POLITECNICO DI MILANO
Scuola di Ingegneria Industriale e dell'Informazione

Corso di Laurea Magistrale in Ingegneria Fisica

Complete mapping of magnon dispersion in antiferromagnetic layered cuprates using RIXS

Tesi Magistrale di

Michele Conni

Matr. Nr. 820655

Relatore: Giacomo Claudio GHIRINGHELLI

Correlatore: Yingying PENG

Anno Accademico 2014/2015

Abstract

In the last decades, the high-temperature superconductivity phenomenon has been widely debated, and even now the physical mechanisms on which it is based are still unknown. However, its correlation with the magnetic properties of the materials in which it shows up has been experimentally probed multiple times; this suggests that a better understanding of the superconductive compounds magnetic interactions is necessary.

To this purpose, the Resonant Inelastic X-ray Scattering (RIXS) technique has proven to be a fundamental method to measure the magnon dispersion relation in superconductive cuprate compounds. In particular, the ERIXS (European RIXS) soft X-ray spectrometer, set inside the ID32 beamline in the European Synchrotron Radiation Facility (ESRF), offers at the present time the best energy resolution possible (less than 55 meV at the Cu L_3 edge). This instrument has started operations in 2015 and the very first experiment has consisted in the measurement of the magnon dispersion relation for three different layered cuprates compounds: $NdBa_2Cu_3O_{6.1}$, $Bi_2Sr_2CuO_{6+x}$ and $CaCuO_2$.

The data analysis is a critical step for understanding the measured samples main features. This procedure however is not univocal, since the theoretical model of high-T_c superconductivity has not been fully developed yet. In this work, the use of the explicit $t-J$ model has been taken into account, and it has been found to be quite insufficient in describing correctly the systems examined. A model based on effective exchange interactions is therefore proposed, which has been implemented in a fitting algorithm thanks to the SpinW Matlab toolbox (from Paul Scherrer Institute). Finally, a physical meaning to the results of the fitting is suggested,

correlated to the contribute provided by the apical oxygens of copper ions to the magnetic behaviour of the inspected compounds.

Sommario

Le onde di spin, alle quali è possibile riferirsi anche con il nome delle loro relative quasi-particelle, i magnoni, sono delle eccitazioni a bassa energia del reticolo di spin in materiali cristallini con simmetria continua. Il loro comportamento è strettamente correlato alle caratteristiche magnetiche del sistema in esame. Come ogni eccitazione reticolare, le onde di spin sono caratterizzate dalla loro relazione di dispersione, la quale dipende dalle interazioni presenti tra gli spin del reticolo. Negli ultimi anni si pensa che esse siano gli agenti principali alla base del comportamento superconduttivo ad alta temperatura.

I superconduttori ad alta temperatura (HTS), scoperti da Georg Bednorz e K. Alex Müller nel 1986, sono materiali che mostrano un comportamento superconduttivo a temperature particolarmente elevate. Nel caso di questa tesi, tali composti corrispondono a cuprati isolanti di Mott drogati con elettroni o lacune. Nello specifico, i superconduttori tradizionali mostrano temperature critiche $T_c < 30\,K$, mentre per i HTS tale grandezza assume valori fino a $138\,K$ (nel caso del $HgBa_2Ca_2Cu_3O_8$). Questo comportamento non è giustificato dalla tradizionale teoria BCS. In particolare, tale modello si basa sul concetto di coppie di Cooper, particelle bosoniche superconduttive formate da una coppia di elettroni legata da una particella di altro genere, nel caso BCS un fonone del reticolo. Teoricamente, tuttavia, tale tipologia di coppie di Cooper presenta una temperatura limite intorno ai $30\,K$. Tuttavia, è ormai ampiamente diffusa l'idea che nel caso dei HTS le coppie di Cooper siano sempre all'origine del comportamento superconduttivo, ma siano tenute insieme non da un fonone, ma da un magnone. Questa ipotesi è supportata dal preponderante comportamento antiferromagnetico presente nei parental compound (cioè i corrispettivi

materiali non drogati) dei HTS. Nel caso dei cuprati, tale comportamento appare nei piani di CuO_2 presenti nel sistema. Tra questi piani sono presenti ulteriori strati formati da ioni di metalli pesanti, lo scopo dei quali è stabilizzare la struttura e fornire le particelle droganti ai CuO_2. Lo studio delle strutture magnetiche dei parental compound è dunque considerato necessario.

Fin dalla loro scoperta, le proprietà magnetiche dei cuprati superconduttori sono state analizzate principalmente con lo scattering anelastico di neutroni (INS). Tuttavia, tale tecnica presenta dei limiti non trascurabili: la grande profondità di penetrazione dei neutroni cotringe ad utilizzare campioni relativamente grandi e la loro energia limita lo studio ad una regione ristretta dell spazio reciproco. Nell'ultimo decennio tali restrizioni sono state aggirate grazie allo scattering anelastico risonante di raggi X (RIXS). Questa tecnica deve la sua notevole evoluzione alla recente introduzione dei sincrotroni di terza generazione, che hanno permesso di aumentare considerevolmente il flusso di fotoni e la risoluzione in energia degli strumenti.

Ad oggi, il RIXS con potere risolutivo più grande è ERIXS (European RIXS), situato nella beamline ID32 di ESRF (European Synchrotron Radiation Facility); tale macchina fornisce una risoluzione efficace di circa 55 meV all'edge L_3 del rame (situato a circa a 930 eV). Lo scopo di questo lavoro è stato quello di implementare una procedura atta all'interpolazione dei dati raccolti con questo strumento durante il primo esperimento in cui è stato utilizzato, avvenuto in Luglio 2015, ed uno successivo, in Novembre 2015. Le misure svolte durante tali periodi hanno avuto lo scopo di caratterizzare tre parental compound di cuprati HTS: $NdBa_2Cu_3O_{6.1}$, $Bi_2Sr_2CuO_{6+x}$ e $CaCuO_2$. Tali misure sono uniche, in quanto prima dell'attivazione di ERIXS le misure RIXS soffrivano di forti limitazioni nel potere risolutivo e nella geometria sperimentale degli strumenti preesistenti. Dagli spettri ottenuti con ERIXS a differenti angoli di scattering è stato possibile ricavare il valore della relazione di dispersione delle onde di spin lungo direzioni ad alta simmetria dello spazio reciproco.

Per eseguire l'interpolazione dei dati, è necessario sviluppare una teoria generale iniziale. Quella più utilizzata è basata sul cosiddetto modello $t-J$, il quale permette

di descrivere un isolante di Mott grazie a due parametri fondamentali: l'energia di hopping t, guadagnata da un elettrone qual'ora si sposti da un atomo ad un suo vicino, e la repulsione coulombiana U. In particolare, nel caso degli isolanti di Mott $U/t \gg 1$. Tale teoria può essere sfruttata per rappresentare le interazioni tra gli elettroni $3d^9$ degli ioni Cu^{2+} nei piani CuO_2; il loro accoppiamento magnetico è dovuto al cosiddetto superscambio, effetto presente tra spin mediato dagli ioni di ossigeno. Difatti, sviluppando l'Hamiltoniana del modello $t-J$, è possibile ottenere una serie di prodotti tra operatori di spin, i quali possono essere riorganizzati in termini di Heisenberg, caratteristici dell'interazione di scambio; tali termini sono contraddistinti dal parametro di scambio J. Il termine di primo ordine di tale sviluppo risulta essere positivo ($J > 0$), cioè l'accoppiamento tra primi vicini in tali materiali è antiferromagnetico.

Il problema di questo modello è che uno sviluppo al primo ordine risulta insufficiente a descrivere in modo soddisfacente i risultati delle misure eseguite. E' possibile ovviare a tale inadeguatezza considerando termini di ordine più alto nello sviluppo dell'Hamiltoniana, definendo in tal modo parametri di scambio efficaci tra atomi via via più lontani. In questa tesi, è stato preso in considerazione un ordine massimo di sei; tuttavia, a causa della grande quantità di parametri, l'interpolazione presenta problemi di convergenza e, siccome l'approccio adottato è efficace, non è possibile definire una relazione analitica tra i parametri di scambio ottenuti in tale processo e le due quantità fondamentali del modello $t-J$, t e U. Questo lavoro ha aiutato a individuare una correlazione tra la struttura cristallina dei cuprati (in particolare la presenza di ossigeni apicali e la loro distanza dagli atomi di rame), la temperatura critica massima e l'estensione degli integrali di hopping.

Summary

The spin-waves, also referred to as magnons quasi-particles, are energetically low-lying excitations of the spin lattice in crystalline materials with continuous symmetry. Their behaviour is strictly correlated to magnetic characteristics of the system. In particular, like any wave-like excitation, they are distinguished by their dispersion relation function, which depends on the magnetic coupling between the atomic spins. In the last decades it has been speculated that spin-waves could be the primary elements of the high-temperature superconductivity phenomenon.

High-temperature superconductors (HTS) are materials, discovered in 1986 by Georg Bednorz and K. Alex Müller, that behave as superconductors at unusually high temperatures. These compounds, in the case of cuprates dealt in this work, are obtained by doping Mott insulator materials with both electrons and holes. Specifically, traditional superconductors have phase transition temperatures $T_c < 30\,K$, whereas HTS show critical temperatures as high as $138\,K$ (for $HgBa_2Ca_2Cu_3O_8$). This high T_c cannot be justified with the conventional superconductivity BCS theory. In particular, the Cooper pairs, i.e. the superconductive particles that are electron pairs bounded by a phonon in the BCS theory, cannot exist at such high temperatures. The most supported hypothesis is that in HTS the two electrons in Cooper pairs are maintained united by a magnon. This conjecture has been suggested by the strong antiferromagnetic behaviour of the HTS parent (i.e. undoped) compounds. In cuprate superconductors the antiferromagnetic properties are determined by weakly coupled copper-oxide (CuO_2) layers present in the system. Their neighbouring layers contain heavy metal ions act to stabilize the structure and dope the copper-oxide layers. It is therefore considered essential to understand better the

physic of the magnetic structure in parent compounds.

Since their discovery, the magnetic properties of superconducting cuprates have been studied chiefly with inelastic neutron scattering (INS). However, this technique has substantial limitations: it requires massive samples (because of the high penetration of neutrons) and it is able to map only a portion of the reciprocal space. To overcome these restrictions, the Resonant Inelastic X-ray Scattering (RIXS) technique has been used. This synchrotron-based spectroscopic technique has become considerably powerful in the past 15 years thanks to the introduction of third generation synchrotron radiation facilities, which allowed a remarkable improvement of photon flux and energy resolution.

The world record of resolving power between RIXS instruments is actually been hold by ERIXS (European RIXS), located at the ID32 beamline of ESRF (European Synchrotron Radiation Facility), providing a combined resolution around 55 meV at the Cu L_3 edge ($\sim$ 930 eV). The aim of this work was to implement a procedure to fit the data gathered during the very first ERIXS experiment, occurred on July 2015, and during a following one, on November 2015. The measurements performed in these two periods have been committed to characterize three cuprate parent compounds: $NdBa_2Cu_3O_{6.1}$, $Bi_2Sr_2CuO_{6+x}$ and $CaCuO_2$. This is the first time that it has been possible to perform this kind of tests on the three compounds. From ERIXS spectra at different scattering angles, it is possible to evaluate the sought magnon dispersion in some points of the reciprocal space.

To fit the outcoming data, it is required to develop a general starting theory. The most generally accepted is the $t-J$ model, which permits to describe a Mott insulator with two fundamental parameters: the electronic hopping energy t from one site of the lattice to another, and the Coulomb repulsion between electrons U. In particular, Mott insulator belong to the case in which $U/t \gg 1$. This theory can be exploited to represent the CuO_2 inplane interactions between the unpaired electron on the Cu^{2+} ions ($3d^9$ electronic state), whose magnetic coupling is due to the superexchange effect, mediated by the oxygen anions. In fact, if the $t-J$ Hamiltonian is expanded in series of spin operators products, it is possible to obtain a sum of Heisenberg

terms, which are characterized by the magnetic exchange parameter J. The first order exchange parameters appears to be $J > 0$, i.e. the system is antiferromagnetic.

The problem with this model is that the nearest-neighbours interaction are found inadequate to fully describe the system. It is possible to obviate this problem by considering higher orders in the Hamiltonian expansion, thus defining more effective exchange parameters that magnetically couple lattice sites of increasing distance. In this work, a maximum order of six has been exploited; however, because of the high number of parameters, this fitting method can give convergence problems and, since it is an effective approach, it is not possible to give a direct relation between the exchange parameters and the two $t - J$ fundamental quantities, t and U.

Contents

List of Figures

Chapter 1

Cuprates

In this chapter we aim to introduce the peculiar characteristics of the studied materials, the cuprates, and to explain why, in this field, Resonant Inelastic X-ray Scattering (RIXS) represents one of the most powerful tools to examine them.

1.1 Crystal structure

Since 1986, year in which Bednorz and Müller discovered the first clues of a superconductive behaviour in cuprates that occurs at temperatures too high to be consistent with the BCS theory [7], a continue endeavor has been made to achieve a deeper comprehension of this phenomenon. Such a deep interest is justified both by the large number of possible applications and by the interesting ensemble of physical behaviours provided by the subject. In fact, the potential technological utilizations allowed by the critical temperature of these materials that exceeds the boiling one of liquid N_2 (at atmospheric pressure) are outstanding. Nevertheless, despite the prosperous literature and the continuous toil on the topic, the high T_c superconducting mechanism is still not clear to this day.

The high-temperature superconductors we are interested in have chemical structure ABO_3; in this notation, A and B are metallic cations and O represents the oxygen. In these materials, atoms can be arranged in different crystalline geometries, that drastically change the role played by the various elements in determining

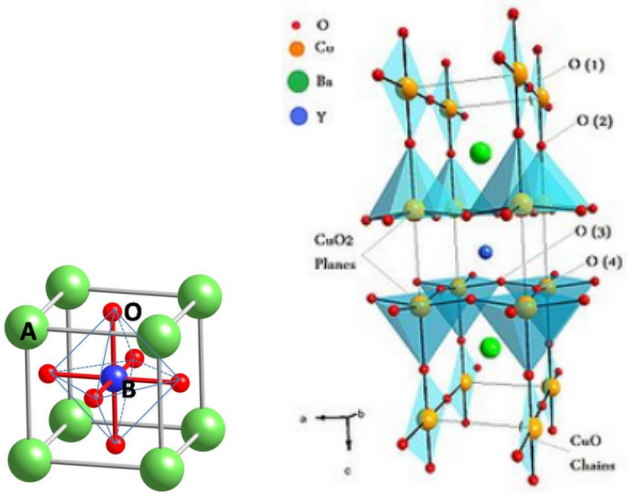

(a) **(b)**

Figure 1.1: *(a) represents a generic AOB_3 crystalline structure. (b) is the scheme of a $YBa_2Cu_3O_{6+x}$ lattice.*

the general substance features. In bulk lattices, A is the larger cation and occupies the corners of a cubic structure, while B is in the center (as seen in figure 1.1a). Oxygen atoms surround B forming an octahedron. This basic structure could be varied in dependence of the relative volume of the ions, thus adopting an orthorhombic cell [8].

However, the most peculiar and interesting role in the structure is played by the Cu (that corresponds to the element B) and O atoms set on bidimensional planes (as in fig. 1.1b), on which the copper is doubly ionized and therefore has a $3d^9$ electronic configuration, i.e. nine of the ten available d orbitals are filled. The presence of out-of-plane oxygen atoms produces a pyramidal crystal structure and affects the copper molecular orbitals by generating a so-called *ligand* (or *crystal*) *field* [25], thus removing their degeneracy and sundering two different energetic branches, t_{2g} and e_g (see fig. 1.2). In particular, the most energetic orbital among the $3d$s is the e_g's $d_{x^2-y^2}$, because of the higher repulsion due to the overlap with the oxygen orbitals, which results in the presence of a unpaired electron and a hole in it. To ease the discussion, the physical picture is often described by reasoning in terms of the single hole [14]; if that is the case, the energy scale must be inverted because $d_{x^2-y^2}$ is the

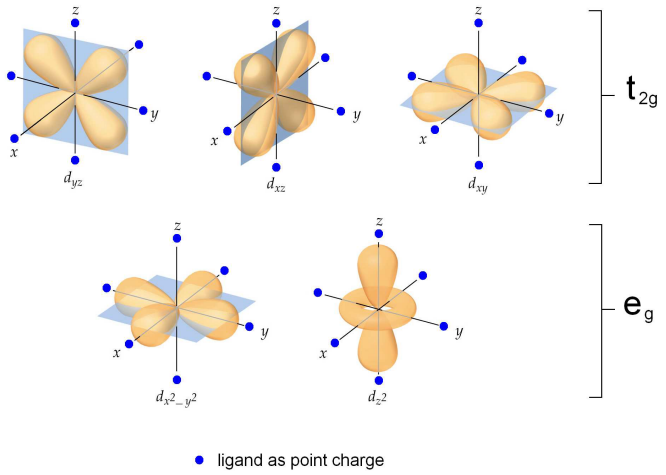

Figure 1.2: *The t_{2g} and e_g molecular orbitals in cuprates.*

lowest energy orbital in which put the hole.

1.2 Significant characteristics

The Cu electrical configuration suggests a metallic behaviour of the material, but it is not so: as a matter of fact, the cuprates are an example of Mott insulators. In this kind of materials, the freedom of the electrons to move in the lattice, signified by the hopping parameter t, drops due to the large Coulomb repulsion between the particles U; that is why this kind of systems are named *strongly electron correlated*.

Another fundamental feature of the cuprates is their magnetic structure: every Cu^{2+} atom has a spin $S = 1/2$, supplied by the unpaired valence electron. Therefore, thanks to a superexchange interaction mediated by the oxygen atoms, at low temperatures an antiferromagnetic long-range spin order arises in the CuO_2 planes. A simple model to describe this order will be discussed in the following chapter, but it is notable to point out that this interaction can be acceptably modeled with the Heisenberg Hamiltonian $\hat{H} = -J \sum_{<mn>} \hat{\mathbf{S}}_m \cdot \hat{\mathbf{S}}_n$ (see (3.20)). In this model the sign of J, that is the exchange constant, determines the nature of the spin interaction: if $J > 0$ it is antiferromagnetic, if $J < 0$ ferromagnetic; in cuprates J it is approximatively $4t^2/U$, and so, as said, antiferromagnetic.

It is worth noting that an antiferromagnetic coupling is also present between the

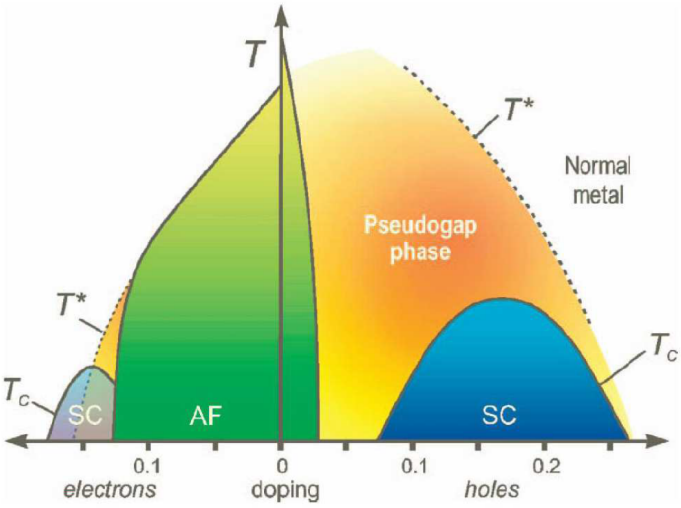

Figure 1.3: *Schematic doping phase diagram of electron and hole-doped high-T_c superconductors; here, SC stands for superconducting and AF for antiferromagnetic phases. Taken from [27].*

atoms that belong to adjacent planes. This interaction is due to the direct exchange, and it is usually rather weak if compared with the inplane one. Furthermore, the Dzyaloshinsky-Moriya (DM) interaction, correlated to the anisotropy of the system, couples ferromagnetically the out-of-plane spin component, but since this effect is quite weak, it appears only if a magnetic field is applied to the material; it can be revealed with the X-ray Magnetic Circular Dichroism (XMCD) technique.

We observed that the common state, usually named parent compound, for a cuprate crystal is insulating. However, when the material gets doped enough, i.e. charges are carried inside the planes by adding oxygen or switching some of the atoms of the parent compound with other elements with a different number of valence electrons, it undergoes a phase transition and becomes superconductive. The doping structure modification is performed on the layers between the CuO_2 planes, that are usually named *charge reservoir* or *blocking* layers. It is therefore interesting to study the phase diagram as function of the temperature T and of the doping [9], as shown in figure 1.3.

There we can see that, as already discussed, the poorly doped material is in an antiferromagnetic phase, and that the superconducting phase is restricted to

low temperatures and a limited doping range, while it does not appear in the parent compound; the superconducting critical temperature T_c shows a maximum, at which the doping is defined as *optimal*, while at high doping percentages the material behaviour becomes metallic. It is also notable that the antiferromagnetic and the superconducting phases do not overlap: therefore doping destroys long-range spin correlations, but it has been observed that the inplane antiferromagnetic alignment is preserved thanks to the short-range interactions.

Another interesting cuprate feature is the *pseudogap phase*, which also appears in the phase diagram (fig. 1.3). This area owes its name to the partial energy gap near to the Fermi energy that looms inside of it, perhaps a superconducting gap forerunner. Inside this region, the material has some odd behaviours (both optical, magnetic and thermodynamic [52]) and shows a critical temperature $T^* > T_c$, but its boundaries have not been well defined yet [35] (this is the reason why in the figure it is delimited by a dashed line). Lots of experiments have been undertaken to improve the understanding of the pseudogap, and they reached the result that T^* lowers with the doping, until it reaches the superconducting phase dome, in which it proves quite difficult to discern its evolution. Also, various pseudogap effects appear to have a different critical temperature trend, and this is why it is difficult to fully define this phase.

Another peculiarity that some families of cuprates (e.g. the "214" family, like $La_{2-x}Sr_xCuO_4$, LSCO in brief) show in the pseudogap phase is a uniaxial modulation of spin and charge orders, commonly named *stripe order* [65]. To fully understand the birth of the stripes, we have to deepen our knowledge about the doping physic: as we already explained, doping holes quench the superexchange interaction, thus dampening the antiferromagnetic long-range order. This happens because their spin is opposite to the one of the Cu^{2+} hole, and thus a doping hole nullifies the local spin on a lattice point. But how do the doping holes distribute themselves on a CuO_2 plane? According to theoretical models [44] [60], they tend to arrange in stripes (see fig. 1.4a): the periodicity of the stripes rises with the doping, until it reaches a maximum, and that point becomes energetically convenient to enhance the filling

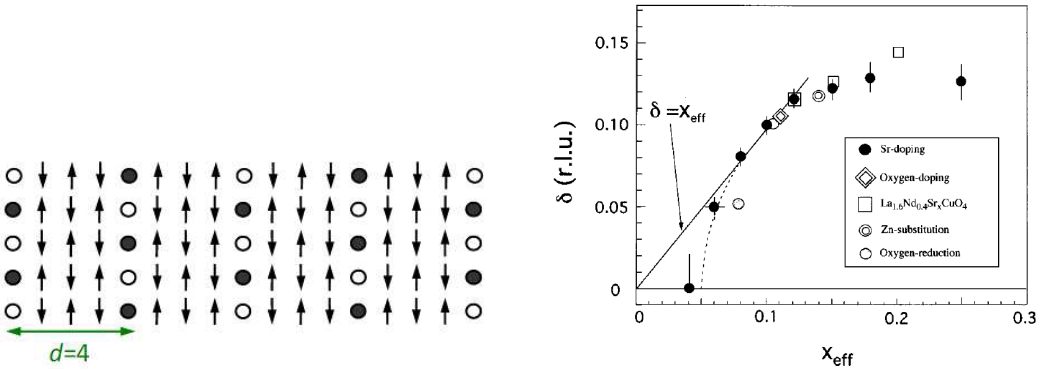

(a) *Schematic doping phase diagram of electron and hole-doped high-T_c superconductors; here, SC stands for superconducting and AF for antiferromagnetic phases. Taken from [27].*

(b) *This is the so-called "Yamada plot". It shows the evolution of the incommensurability parameter δ with hole doping. After a linear increase, δ becomes constant at $p \simeq 1/8$. Taken from [69].*

Figure 1.4: *Doping phase diagram of a generic high-T_c superconductor (left) and Yamada plot (right).*

factor (i.e. the density of holes in each stripe). This results have been experimentally observed with spin ordering sensitive INS experiments: it is in fact possible to observe a spike generated by the stripes at incommensurate distance δ from the parent compound diffraction peak. Then, the δ dependence on doping has been proved to have a saturation point (seen in fig. 1.4b, at which the superconductivity shows a reduced critical temperature T_c. It is thus reasonable to suppose that the two phenomena somehow compete one with the other, thus explaining the T_c drop.

Finally, X-ray scattering revealed that, nearby the doping $p \simeq 1/8$ region in the pseudogap, some cuprates (e.g. the members of the "123" family, like $YBa_2Cu_3O_{6+x}$) show charge density modulations in the CuO_2 planes, that have been acknowledged as *charge density waves* (CDW). In some compounds these waves compete with the superconducting phase and therefore show a T_c drop (referred at as *plateau*) around the mentioned doping ([42], fig. 1.5a); furthermore, at plateau dopings, the RIXS spectra show a maximum intensity for the quasi-elastic peak (fig. 1.5b). The position of the peak in the reciprocal space permits to effectively distinguish CDW from the stripe order; the interaction has also been definitively confirmed as a charge density

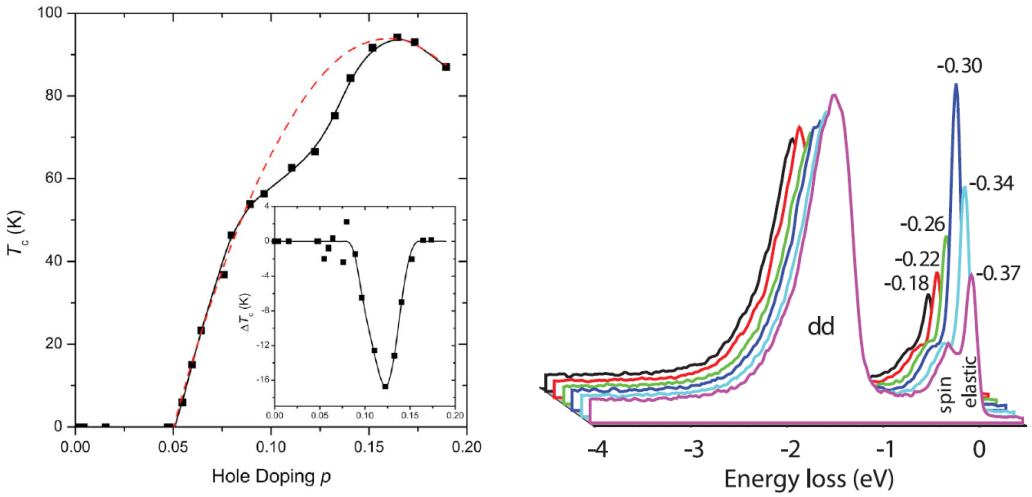

(a) *Dependence of the superconducting phase critical temperature T_c of YBCO on doping. The so-called plateau is clearly visible moving away from the dashed parabolic line, and it has a maximum suppression at $p \simeq 1.8$. From [42].*

(b) *Quasi-elastic peak at transferred momentum $\mathbf{q}_{\parallel} \simeq 0.31$ r.l.u. shown in RIXS spectra; it is evidence of the onset of incommensurate charge density order. From [28].*

Figure 1.5: *Two experimental consequences of the charge density waves in YBCO.*

rather than a spin modulation [28] [13]. Since $T_{CDW} < T^*$, the CDW instability is bounded inside the pseudogap [9].

All the mentioned effects (stripes, pseudogap and CDW) are thought to be somehow related to the superconductive effects. In particular, the most shared theory is the one that points the magnons (i.e. magnetic interaction particles) as strong candidates to cover the role of glue for the Cooper's pairs instead of the phonons (as in the classical superconductivity theory). This supposition rises from the importance of the magnetic interactions in the high-T_c superconductive compounds, as well as from the characteristics we have enlisted in this chapter. Therefore, it is believed that to fully understand an high-T_c superconductive material, first it is necessary to have a deeper knowledge of its parent compound.

In the last decades the study of the magnetic properties of cuprates has been carried on almost solely with the inelastic neutron scattering (INS) technique, that

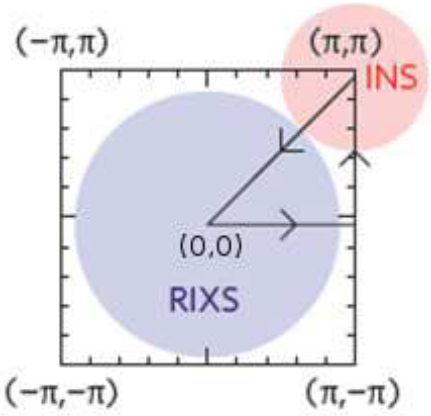

Figure 1.6: *Accessible regions of 2D Brillouin zone for Cu L_3 RIXS and inelastic neutron scattering (INS) applies on cuprates. From [48].*

has proven to be extremely useful and prolific [31] [67]. However, INS has some limitations: as shown in the figure 1.6, its area of study is confined in the surroundings of the Brillouin zone corners, and furthermore the neutron high energy requires the employment of massive samples (hundreds of mm^3 or more). Both of these deficiencies can be satisfactorily overcome by the RIXS set up [40]: fig. 1.6 points out that RIXS can overlay an extensive portion of the Brillouin Zone not covered by the INS and it is effective on the analysis of small samples (down to a few μm^3 in volume). However, because of the limited RIXS energy resolution, the low energy scale (i.e. below 50 meV at present) remains the domain of neutrons. This is why, in recent years, the combination of both RIXS and INS techniques has become mandatory to fully understand the cuprate physic. In particular, the materials discussed in this work are hardly measurable with neutrons because of the fine geometric structure of their lattice.

Chapter 2

RIXS

In the previous chapter we have illustrated the benefits brought by RIXS technique in cuprate study. However, this type of measurement would not be applicable if it wouldn't be for the enormous steps forward made by synchrotron technology in the last decades. In fact, RIXS aim is to probe magnetic and electronic excitations in materials [3], but, for reasons we will explain in this chapter, that requires an extremely intense and monochromatic source [37].

In this chapter we will thus give a general description of RIXS and we will expose the peculiar features of ERIXS, the spectrometer, placed on the ID32 beamline at ESRF, exploited to collect the data showed in this work.

2.1 RIXS working principle

RIXS is an acronym that stands for *Resonant Inelastic X-ray Scattering* and it epitomizes a synchrotron-based scattering measurement technique developed in the last two decades to study the elementary excitations of the matter [29] [2] [15]. Scattering measurements involve the analysis of a sample through the observation of the effects sprang from its interaction with some kind of probing object, which in our case is a synchrotron X-ray beam. In particular, RIXS is a photon *in*-photon *out* spectroscopy techniques: a light beam is sent on the sample, and the detected interaction result is yet again a photon beam. As already acknowledged, the incoming

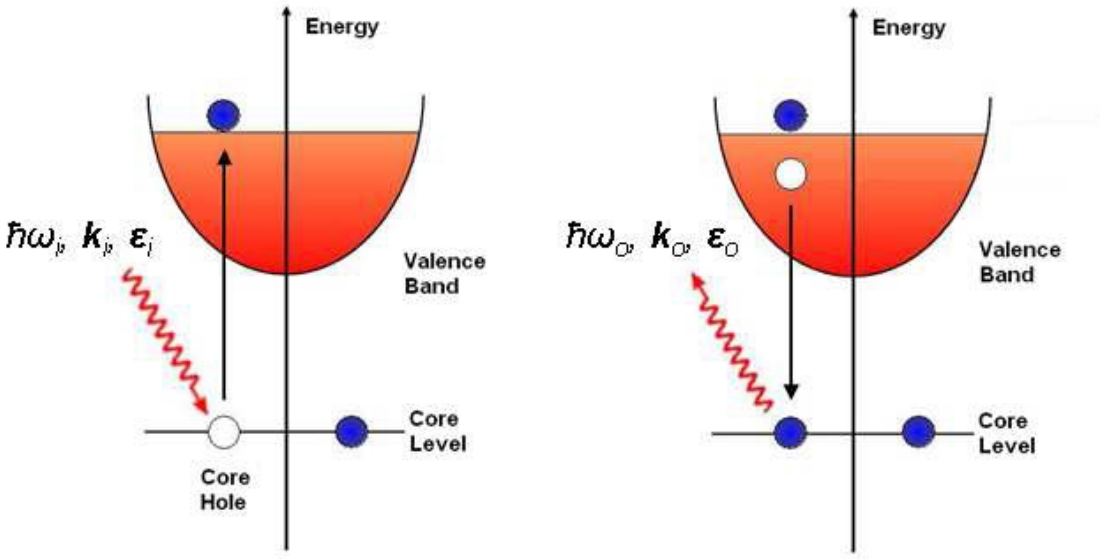

Figure 2.1: *Scheme of the RIXS scattering process: the incoming photon ($E_i = \hbar\omega_i$) gets absorbed by the system, thus promoting a core electron to an empty valence state above the Fermi level and creating a core hole (left panel). After ~ 1 fs, a valence electron fills the core hole and a photon ($E_o = \hbar\omega_o$) is emitted (right panel). Image taken from [48].*

beam energy falls into the X-rays region, since it thus allows to inspect the core atomic energy levels [2]. The beam energy used belongs to the soft X-ray region, i.e. photons with an energy between 100 eV and 2 keV. Since the soft X-rays penetration depth is in the scale of tens of nm, the incoming and outgoing photons can pass through several atomic layers, thus probing the bulk of the inspected material. However, it is also possible to examine the sample surface by working in grazing incidence conditions, i.e. at high angles of incidence $\theta_\perp$ (in fact, as intuitively understandable, the probing depth of the beam decreases with $\sin\theta_\perp$, see fig. 2.9). In general, the detected outgoing photon is different from the incoming one in either energy E, momentum $\mathbf{k}$ or polarization ϵ [47].

The RIXS process is a *second order process* (see fig. 2.1). This means that the exit radiation is product of two consecutive events: first, the incoming photon excites an atomic core electron of the sample to a free valence state, above the Fermi level; however, this state is highly unstable (it has $\sim 1fs$ lifetime), so another electron quickly fills the core hole, which causes the emission of the outcoming photon, that

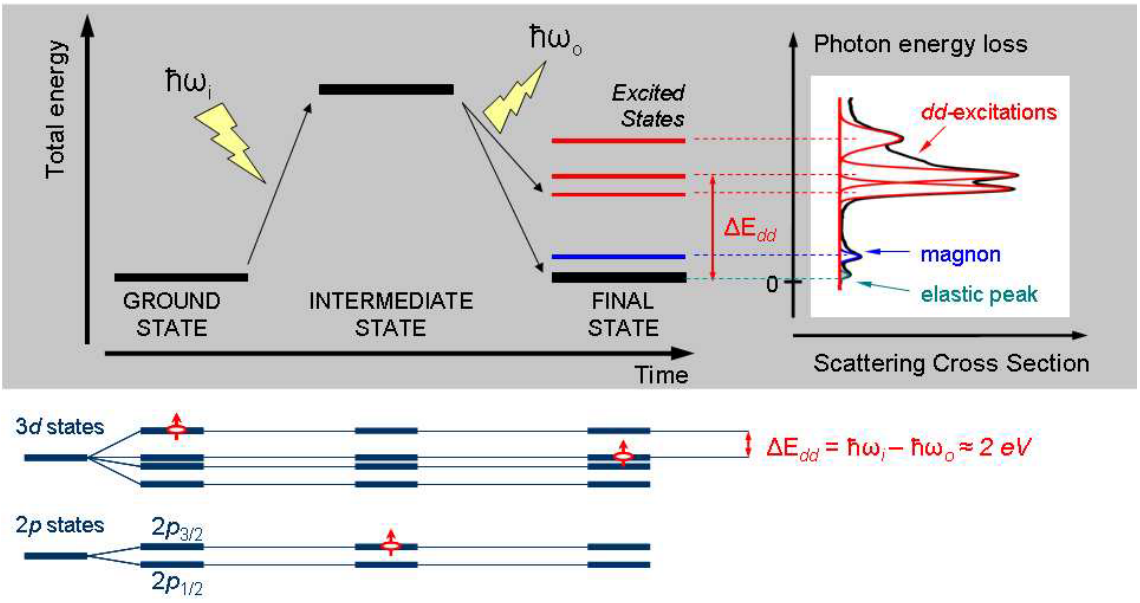

Figure 2.2: *The various stages of a Cu L_3 RIXS double scattering process and the generic output spectrum. On the bottom of the figure is depicted the same process from the Cu $3d^9$ hole (i.e. the red mark) point of view.*

is collected with a suitable revelation device. Since it exploits a two step process, this technique permits to observe a vast variety of effects, because it is not limited by the dipole selection rules, but every observed effect has a very small cross-section; therefore RIXS requires a high intensity incoming beam (i.e. synchrotron radiation). Furthermore, another RIXS feature is that, being based on a photon *in*-photon *out* process, it preserves the overall neutrality of the system, thus avoiding any change in the total charge of the system. Otherwise, the measurement could modify the system energy levels in a way that is difficult to foresee, and the measurement results would be more difficult to understand.

The outcome of a RIXS experiment is a spectrum, i.e. the intensity of the collected beam as a function of the photon energy loss (see figure 2.2). This variable can be easily defined as $\Delta E = E_i - E_o$, where E_i is the incoming photon energy and E_o is the outgoing one; it is clear that $\Delta E > 0$. Every spectrum shows an high intensity peak at $\Delta E = 0$, that is called the *elastic peak*, since it is only determined by the elastic scattering events, i.e. when the revealed photon has the same energy of the probing one, that happens when, after the excitation, the electron returns

to its original core level. Apart from the elastic peak, the spectrum involves an inelastic scattering event, in which $E_o < E_i$ and there is therefore an energy loss in the process. Another fundamental measurable quantity is the photon momentum: the tilting of the sample and the variable position of the collection device allow to regulate the $\mathbf{k}_i$ and $\mathbf{k}_o$ momenta of the input and output photon respectively. It is thus possible to calculate both the energy and the momentum of the examined excitation as:

$$\hbar\omega_i = \hbar\omega_o + E_{ex} \tag{2.1}$$

$$\hbar\mathbf{k}_i = \hbar\mathbf{k}_o + \hbar\mathbf{q}_{ex} \tag{2.2}$$

where, while the properties of the incoming photons are assumed as known, the output photons' ones are measured. Finally, there is a last fundamental measurable property of the output beam, and that is the polarization ϵ_o, that is effectively observable with the actual RIXS setup, even though it is a quite difficult task [11].

Finally, we still haven't made clear why RIXS technique is addressed as resonant. This adjective refers to the wide freedom in energy tuning provided by RIXS. In fact, the absorption spectrum of a generic sample shows peaks in coincidence with any incoming photon energy that is able to excite core electrons to the valence band in an element of the sample. Since the correspondence between the position of these peaks and the related energy excitation and component is well-known, it is possible to tune the RIXS incoming beam energy to focus the measurement on a particular chemical element and study the excitations from its perspective. Moreover, because the absorption energy depends also on the environment in which the atom is included, RIXS is able to partially identify different configurations of the same element in the same sample. This is the feature that permits RIXS to analyze small samples, in spite of its high bulk sensitivity.

In the RIXS in the ID32 beamline at ESRF, usually referred to as ERIXS, we made use of devices that allow the tune of the input photons energy in the range between 400 eV and 1600 eV. These boundaries are such that we can explore interesting energy edges, like the oxygen K edge, the $M_{4,5}$ edges of rare earths

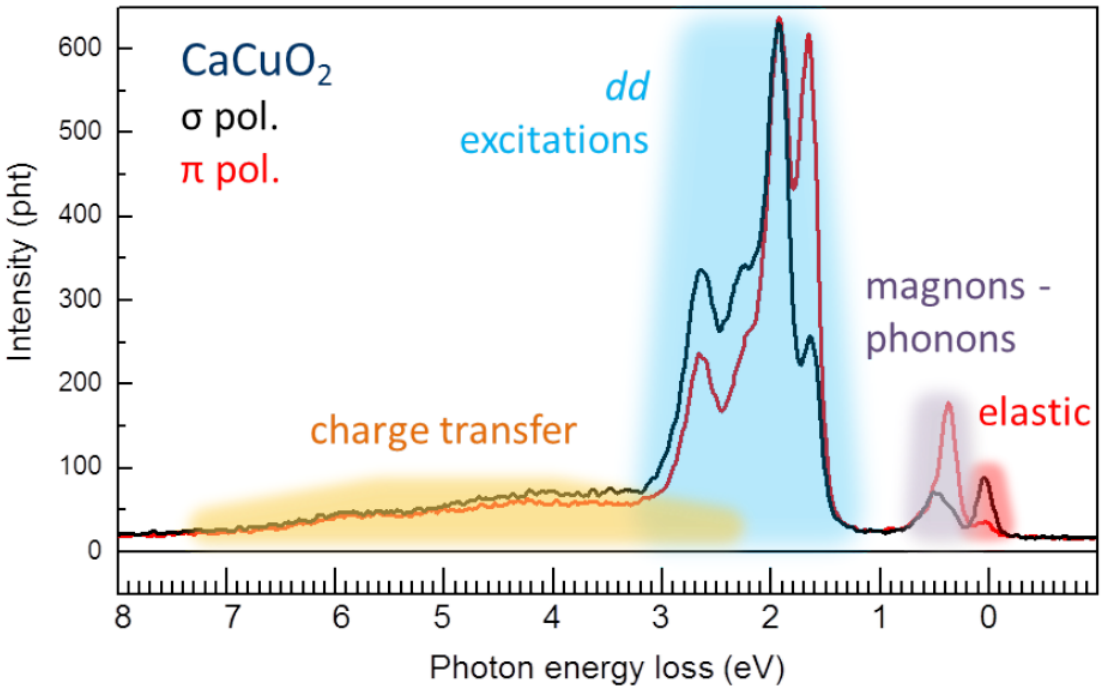

Figure 2.3: *Example of a typical RIXS spectrum of a $CaCuO_2$ sample. The relevant excitations observable with RIXS are highlighted. The red and black curves correspond to the in-plane polarization and its orthogonal respectively.*

and the $L_{2,3}$ edges of transition metals, for example copper (see fig. 2.3). The RIXS resonance permits a quite astounding flexibility in the measurements, because, when the incoming beam is tuned to an absorption edge of a specific element, the contribution to the spectrum due to the other chemical elements in the samples becomes negligible.

Now, let's look at a standard $CaCuO_2$ RIXS spectrum (shown in fig. 2.3) taken at Cu L_3 edge, which corresponds to an electron excitation from $2p_{2/3}$ level to valence shell in the $3d$ orbital. In the figure we can observe various peaks: if we reason in terms of the single $3d^9$ hole, which is excited by the incoming beam to a core level, we can say that the elastic peak is due to the return of the hole to its original state, while the so-called *dd* excitations correspond to the relocation of the hole on a different d state; the *dd* excitations are a clear example of transitions not allowed by electric dipole selection rules that can be inspected with RIXS. But the most important spectral feature for this work is the magnons' peak: a magnon is the

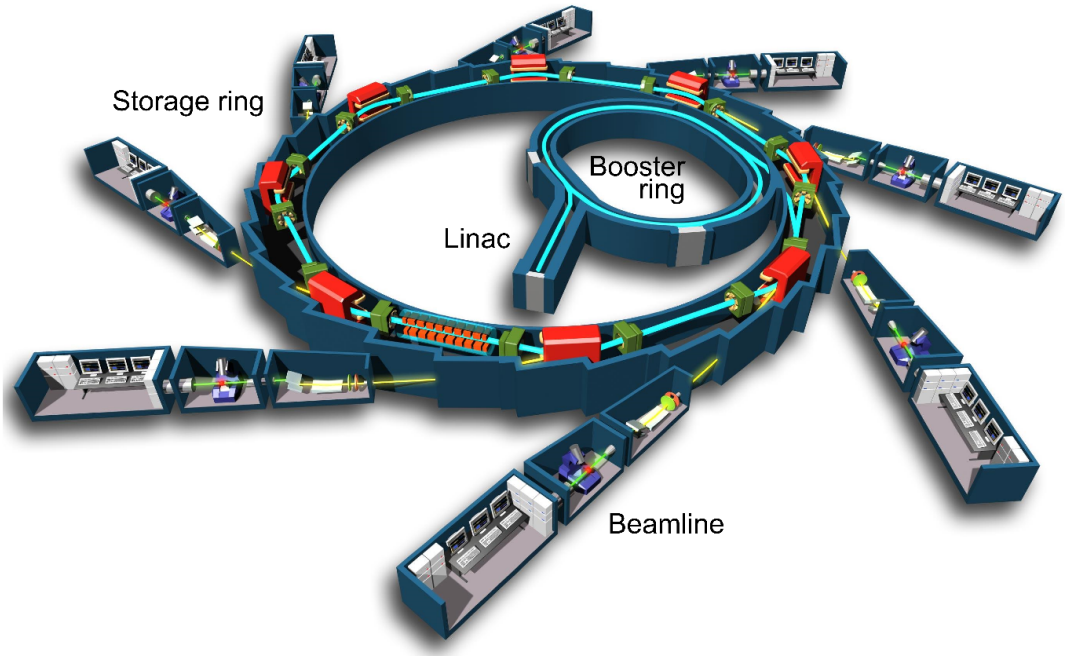

Figure 2.4: *Scheme of an ordinary sinchrotron facility, from [63].*

quasi-particle ($E_m \sim 100$ meV) equivalent to a spin-wave, i.e. a collective excitation of the spin lattice propagating thanks to the high magnetic interaction between the components of the sample. Other observable excitations are the phonons, i.e. collective real lattice excitations, which have approximatively the same energy of magnons, and the charge transfer excitations, that correspond to electron transfers from copper ions to the surrounding atoms. Finally, note that the two black and red plots in fig. 2.3 correspond to the two different orthogonal polarizations (σ perpendicular and π parallel to the scattering plane [58]), and we can see that some peaks intensity changes between the two.

2.2 The ESRF synchrotron

As already made clear, RIXS technique requires high intensity X-ray sources to work properly, and these can be provided by synchrotron facilities, like the *European Synchrotron Radiation Facility* (ESRF), located in Grenoble, France. In fact, a third generation synchrotron like the ESRF provides to his laboratories a radiation with

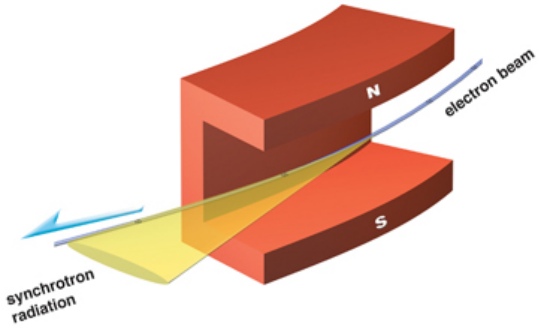

Figure 2.5: *Representation of the bending magnets' action.*

a continuum spectral range between the infrared and the hard X-rays frequencies.

The radiation is generated by a beam of electrons, which have been accelerated up to relativistic velocities, that flows inside the synchrotron ring, whose model is shown in fig. 2.4. In particular, the electrons are generated by the electron guns situated inside the ring, and are firstly accelerated by *linacs* (i.e. linear accelerators). From there, they are injected inside the so-called *booster ring*, the smaller one in figure, where they once again gain speed; since the electron mass increases with its energy, the magnetic field applied in this stage must be $B \propto E_{electron\,beam}$. Eventually, when properly accelerated, the beam in redirected inside the outer ring, named *storage ring*, where they emit radiation to supply the nearby laboratories, usually referred to as *beamlines*.

The beam trajectory is maintained circular with bending magnets (see fig. 2.5), therefore the radiation produced is tangential to the beam itself; actually, the generated photons have a small vertical divergence θ ($\theta \sim 1/\gamma$, where γ is called Lorentz factor [32]). Between two bending magnets, in the storage rings, are placed some quadrupoles and sestupoles, whose purpose is both to focus the beam and to avoid aberrations (which results in a radiation with a slightly different energy from the one reckoned). Third generation synchrotrons exploit another typology of devices: the *insertion device*; they are periodic structures of magnetic dipoles that produce sinusoidal magnetic field to make the beam trace a swinging path. These instruments, they too placed between the bending magnets, force the beam to emit more radiation and moreover they raise the beam brilliance, monochromaticity and directionality.

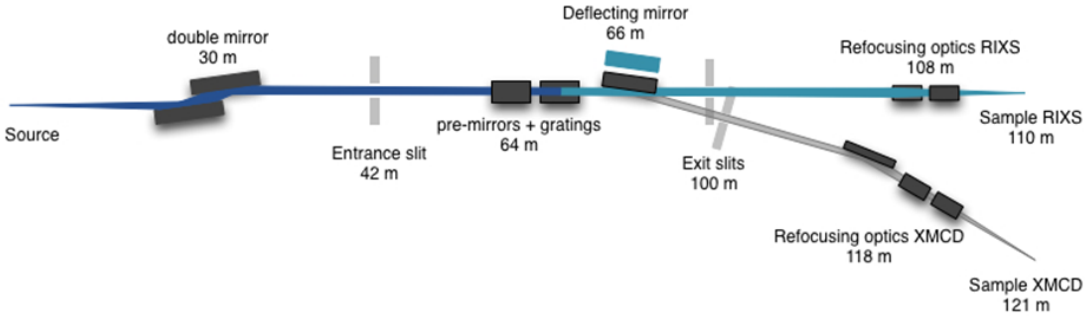

Figure 2.6: *Optical scheme of the ID32 beamline at the ESRF (from [34]).*

Also, depending on the angular deviation imposed to the electron route, the outcoming radiation shows different characteristics, that can be chosen depending on the desired application.

2.3 ERIXS

In this paragraph we want to give a brief look to the practical implementation of a RIXS; in particular, we refer to the design of ERIXS(European RIXS facility), the spectrometer located in the ID32 beamline at ESRF which was used to collect the data used in this work. As we already beckoned, RIXS technique, exploiting a second order process with little cross-section, requires an high intensity input beam to work properly; because of this reason, it is often defined as *photon hungry*. However, this permits RIXS to have an high resolving power, thus allowing to better distinguish all the spectra elements. At the present time, one of the active RIXS that provides better performances is ERIXS, located in the ID32 beamline of ESRF and designed by Prof. G. Ghiringhelli, from the Politecnico di Milano, and his coworkers. The same team previously conceived two other RIXS instruments: AXES, placed in the old ID08 beamline of ESRF and now dismissed, and SAXES, located at the ADDRESS beamline of the Swiss Light Source (SLS) and currently active.

ID32 is actually the only beamline in ESRF to work in soft X-rays, and, as we previously mentioned, contains also an XMCD instrument. Figure 2.6 shows the beamline scheme. In this picture, the beam source is constituted by three APPLE

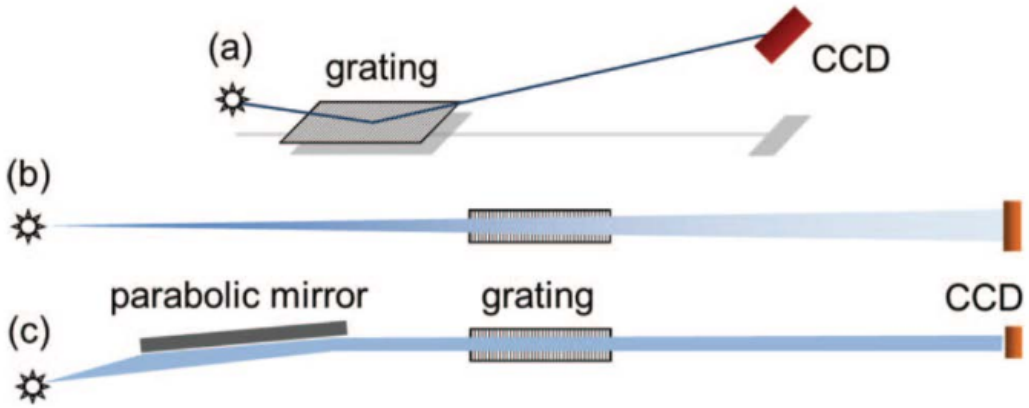

Figure 2.7: *Sketch of the optical layout of a soft-RIXS grating spectrometer.*

II undulators [59] that receive the synchrotron radiation and tune the beam energy; these undulators are also able to provide 100% horizontal, vertical, right and left circular polarized light at will. Then, the double mirror focuses the beam in the entrance slit, from where, with a reflecting mirror, can be redirected on the XMCD or on the RIXS branch. Before the deflecting mirror are disposed two gratings (one for RIXS and one for XMCD) that ensure the beam monochromaticity. These two monochromators are both variable line spacing (VLS) gratings and the one for XMCD also has a sagittally refocusing mirror. After this, the beam comes out from the optics hutch through the exit slit and is focused on the sample; the total distance between source and sample is 110 m. The XMCD principles explanation is outside of this work's purposes, therefore it will not be reviewed here.

ERIXS, like its precursors, works on the principle shown in figure 2.7. The sample itself acts as the spectrometer source, emitting the second order interaction outcoming photons. The final measurement result, i.e. the sample spectrum, is obtained by diffracting the outgoing beam with a concave grating tilted so that it works at grazing incidence. The slight concavity permits to focus the beam on the detector, that would be in our case a CCD (charge-coupled device). The grating is a VLS device, similar to the monochromators before the reflecting mirrors; its grating lines are perpendicular to the direction of the photons. It is the only optical element of the scheme.

Therefore, the photons are vertically dispersed on the CCD surface, thus generating a 2D image. Since the photons' trajectory is more or less deviated in dependence of their energy, the image appears to be composed by isoenergetic parallel lines, which are then summed to obtain the resulting spectrum. To do this, the CCD must be placed on the diffracting grating's focal plane. In ERIXS case, the detector is a commercial thinned back-illuminated CCD, $25.4 \times 25.4\, mm^2$ in size and with $13.5\, \mu m$ square pixels. Its effective spatial resolution is $25 \mu m$ [23], but that can be improved by using it at grazing incidence (fig. 2.8): if tilted of an angle γ (in ERIXS $\gamma = 30°$), the effective resolution becomes $\Delta E_{CCD} = \sin\gamma \cdot 25 \mu m$.

However the overall instrument resolution results from:

$$\Delta E_{TOT} = \sqrt{\Delta E^2_{beamline} + \Delta E^2_{spectrometer}} \tag{2.3}$$

where $\Delta E_{beamline}$ it determined by the monochromator and is ~ 22 meV at the Cu L_3 edge, while $\Delta E_{spectrometer} = \sqrt{\Delta E^2_{source} + \Delta E^2_{slope} + \Delta E^2_{CCD}}$. Here ΔE_{source} is determined by the size of the beam spot on the sample ($FWHM = 4\, \mu m$) and ΔE_{slope} is due to the already discussed slope error ($230 nrad$ rms). These numbers, for a grating with 1400 lines$/mm$ as the one in ID32, lead to a theoretical resolution of ERIXS around 38 meV at the Cu L_3 edge. Combined with 30 meV of the beamline monochromator, (2.3) gives 51 meV. The actual FWHM, measured on the elastic peak scattered from a polycrystalline graphite sample, is 55 meV.

Another developed way to enhance the measurement resolution is the exploitation of the so-called *single-photon counting* (SPC) algorithm [4] [39] [5]. This method was conceived to overcome the fact that a photon, when it comes from the sample to the CCD, is so energetic that it generates an avalanche effect on the CCD electrons that expands over multiple pixels. This represents a big limit to ERIXS resolution. What the SPC algorithm does is to statistically reconstruct the position of the photon impact, and even to a sub-pixel level (i.e. inside a portion of the pixel). In fact, the SPC algorithm brings the CCD effective resolution from 25 to 8 micron.

Finally, it will be useful to better understand the method of collection of ERIXS data (and thus their meaning). Samples are usually contained inside a chamber in ultra-high vacuum (UHV) and they are attached on hexagonal sample plates with

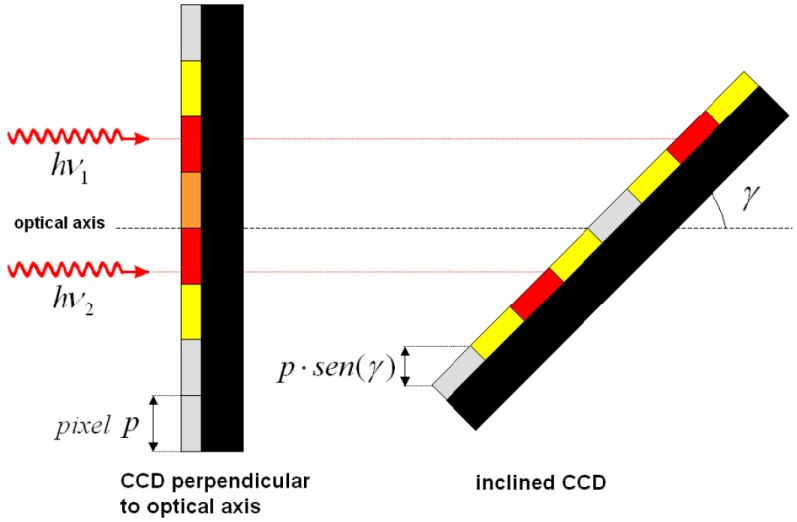

Figure 2.8: *Improvement in the effective spatial resolution for CCD inclined of an angle* γ.

silver paint, double-sided metallic adhesive tape or conductive glue; the holder is then connected to a full 4-circle in vacuum goniometer, used to manipulate the samples in the beam. The goniometer allows samples to be moved in the three spatial directions and rotated directly from the control cabin. The rotation allows to vary the beam angle of incidence on samples, thus altering at will the transferred momentum $\mathbf{q}$, as shown in figure 2.9. Furthermore, if the crystal axes of the sample are known, this permits to choose the momentum projected on the CuO_2 planes $\mathbf{q}_{\parallel}$. Since can be demonstrated that the excitations perpendicular to these planes have a negligible role on the determination of a cuprate dispersion relation, this permits to scan the bidimensional reciprocal lattice of the sample.

Since the CuO_2 planes are parallel to the sample surface, it is possible to define the following angles: the incoming beam hits the sample surface with an angle of incidence θ_i, while the outgoing beam is collected at the angle θ_o. During the measurements, the scattering angle 2θ between $\mathbf{k}$ and $\mathbf{k}'$ is usually maintained fi

xed, while the incident angle is changed by rotating the sample holder. The sample rotation defines the angle δ shown in the figure, that corresponds to the angle between the sample c-axis and the transferred momentum $\mathbf{q}$. Once the samples are

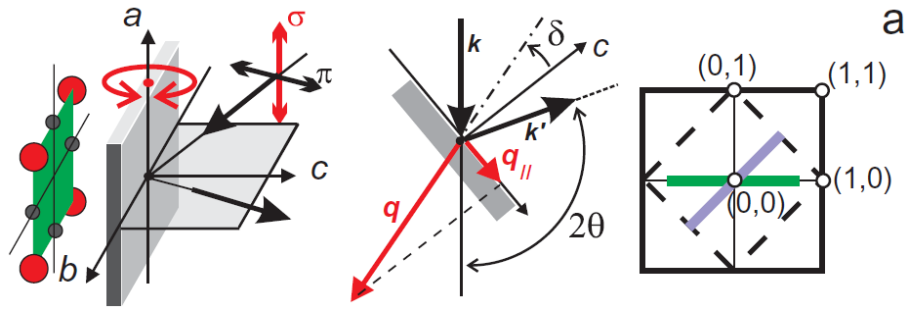

Figure 2.9: *Experimental scheme for RIXS measurements on cuprates and 2D Brillouin zone for cuprates. Taken from [48].*

mounted in the UHV chamber, the direction on which scan the Brillouin zone is thus chosen by orienting the a and b axes with respect to the scattering plane.

2.4 Resolution performances

AXES (Advanced X-ray Emission Spectrometer) and SAXES (Super-AXES) were two dedicated high resolution RIXS spectrometer whose evolution brought to design of ERIXS. AXES, working since 1995 at the beamline ID08 of the ESRF and now dismissed, had a combined resolution at the Cu L_3 edge $\sim$ 235 meV. The currently working SAXES [28], located at the ADDRESS beamline of the Swiss Light Source (SLS), gave a resolution of around 130 meV at the Cu L_3 edge [58]. The enhancement of SAXES resolution by a factor 2 with respect to AXES is primarily due to the fact that the instrument is roughly twice longer. As already calculated, ERIXS managed to obtain another improvement in resolution, allowing to measure Cu L_3 RIXS with a combined resolution of 55 meV. In fig. 2.10 two spectra, one from SAXES and the other from ERIXS, of the same compound are shown to highlight the effects of this improvement.

2.5 Measurements

Before showing the measurement results, let us give a brief introduction to the distinguishing features of the three cuprate compounds analyzed in this work: NBCO,

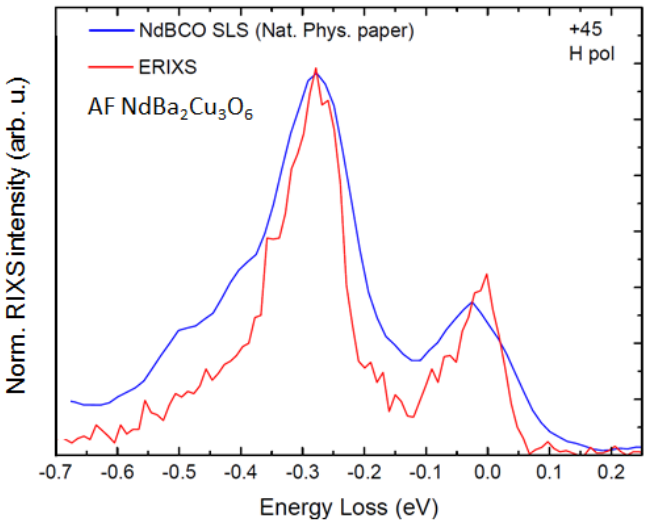

Figure 2.10: *NBCO Cu L_3 RIXS spectra. The red spectrum has been measured with RIXS, while the blue one was measured with SAXES in equivalent conditions. Note the sharp magnon peak and the phonon as a shoulder of the elastic peak. From [22].*

Bi2201 and CCO.

NBCO stands for $NdBa_2Cu_3O_{6.1}$; it has a structure analogous to YBCO, whose unit cell is shown in 2.11a. In that figure the Cu in-plane atoms with different spins are highlighted with red and orange colors, while the ones in light red are copper atoms that do not take part in the magnetic coupling and are said to be organized in chains (in the doped compounds, where extra oxygen atoms would lay in their own plane). The neodymium atoms are exactly in the center of the cell, i.e. in the empty space between the planes, whereas the barium atoms are aligned with them, but between the plane and the underlying chains. On the plane the Cu atoms are distant 3.84 Å, both in a and b directions, the whole cell is 11.7 Åhigh on the c direction and between two adjacent planes there are 3.2 Å(thus the distance between chain and plane is 4.25 Å).

$Bi_2Sr_2CuO_{6+x}$ crystalline structure is shown in fig. 2.11b; from this picture, we can see that a BiSCO unit cell contains two CuO_2 planes, one with the positions of Cu and O inverted in respect with the other. The distance between the planes is 12.2 Å, therefore the unit cell is $c = 24.4$ Åhigh, while the in-plane structure is squared ($a = b = 3.86$ Å). Between these two there are four more planes with Bi^{3+} or

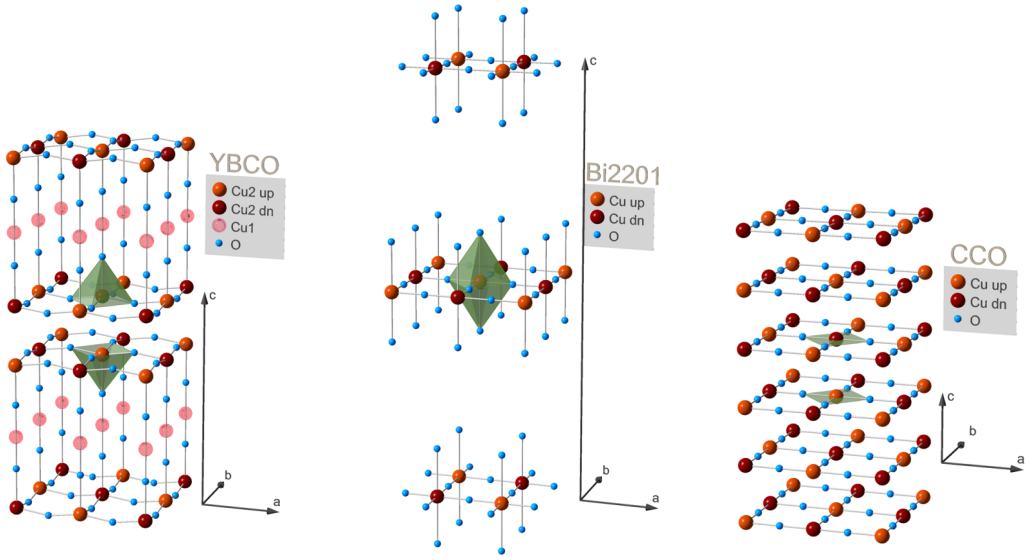

(a) **(b)** **(c)**

Figure 2.11: *$YBa_2Cu_3O_7$, $Bi_2Sr_2CuO_{6+x}$ and $CaCuO_2$ crystal unit cell. Cu1 are the chain copper atoms, Cu2 are the plane ones. In the legend, "dn" means down, referring to the spin.*

Sr^{2+} and O structures, which however don't take part to the magnetic interactions, as Nd in NBCO.

Now let us introduce the $CaCuO_2$ structure, shown in fig. 2.11c. CCO is almost the opposite of Bi2201: it is composed by the alternation of CuO_2 planes and CaO_x ones. As usual, the in-plane configuration is squared and the bond length is $a = b = 3.8$ Å, while the distance between the copper planes is $c = 3.2$ Å.

Figure 2.12a shows the results of the ERIXS measurements used in this work. These have been gathered during two beamlines at ESRF, on July and November 2015, that have been the first applications of ERIXS. The measurements were performed on the path pointed out by the arrows in fig. 2.12b, that is $[0.25\,0.25] \rightarrow [0.5\,0] \rightarrow [0\,0]$. In the figure, the magnetic first Brillouin zone is stressed by the dashed red line. Since the magnetic cell is two times the lattice unit cell, the magnetic first Brillouin zone will be the half of the lattice one. In the same figure the Brillouin zone critical points are stressed. The data to fit have been obtained from the circled points in figure 2.11c; they correspond to the magnon peaks determined

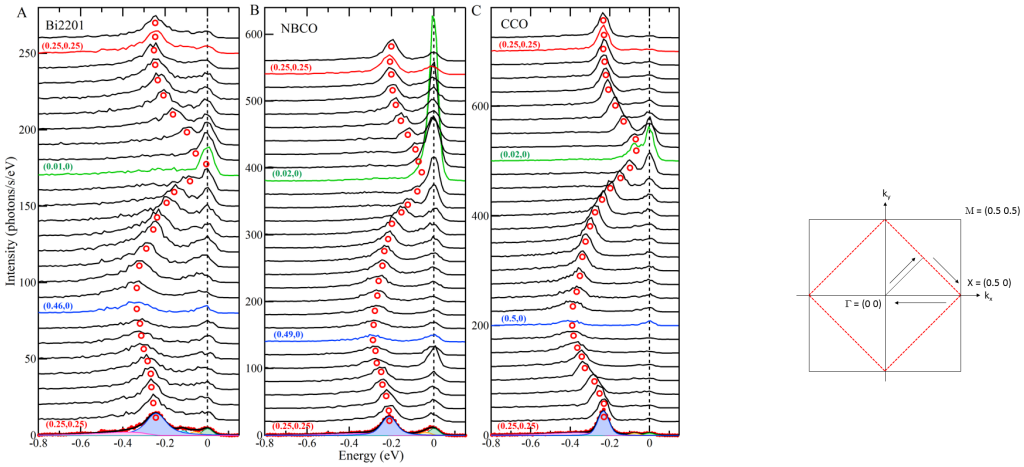

(a) *Three-dimensional dispersions of magnetic excitations in layered cuprates for Bi2201 (A), NBCO (B) and CCO (C). Each spectrum is shifted vertically for clarity. Circles denote the peak positions of spin excitations determined by fitting.*

(b) *First Brillouin zone in the reciprocal space. All points are expressed in r.l.u.*

Figure 2.12: *Measured spectra (left) and magnetic first Brillouin zone map (right).*

by decomposing the various spectra in its fundamental interaction elements, i.e. the elastic, *dd* and charge transfer excitation functions.

Chapter 3

Theory

In this chapter we aim to point out the cornerstones of the theoretical modeling of the spin-wave dispersion relation measured in insulating cuprate materials. Starting from the introduction of the second quantization method, we pass through the Hubbard model, to eventually define the $t - J$ Hamiltonian, one of the methods most currently exploited to model magnetic systems. Then we apply a low energy theory and the spin wave theory to evaluate an effective dispersion relation for the spin-waves in the material. Finally, we briefly describe the linear spin wave theory, based on which is set up the program that we used to fit the dispersion relation, SpinW.

3.1 The Hubbard model

3.1.1 Second quantization

This thesis' work is based on the Hubbard model theory. To fully understand this theory, first we must introduce the so-called *second quantization theory* (see [1]). It is known that, because of their indistinguishability, bosons' and fermions' wave functions must be expressed only with symmetric and antisymmetric terms; an appropriately symmetrized N-particle wavefunction can be expressed in the form:

$$|\lambda_1, \lambda_2, \ldots, \lambda_N\rangle \equiv \frac{1}{N! \prod_{\lambda=0}^{\infty}(n_\lambda!)} \sum_{\mathcal{P}} \zeta^{\frac{1-\mathrm{sgn}\,\mathcal{P}}{2}} |\lambda_{\mathcal{P}1}\rangle \otimes |\lambda_{\mathcal{P}2}\rangle \otimes \cdots \otimes |\lambda_{\mathcal{P}N}\rangle \qquad (3.1)$$

where $\zeta = -1$ for fermions while $\zeta = 1$ for bosons. n_λ represents the total number of particles in state λ (for fermions, Pauli exclusion enforces the constraint $n_\lambda \leq 1$). The sum runs over all $N!$ permutations of the set of quantum numbers $\{\lambda_1, \ldots, \lambda_N\}$, and $\operatorname{sgn}\mathcal{P}$ denotes the sign of the permutation $\mathcal{P}$ ($\operatorname{sgn}\mathcal{P} = 1[-1]$ if the number of transpositions of two elements which brings the permutation $(\mathcal{P}_1, \mathcal{P}_2, \ldots, \mathcal{P}_N)$ back to its original form $(1, 2, \ldots, N)$ is even [odd]). The prefactor $\frac{1}{N!\prod_{\lambda=0}^{\infty}(n_\lambda!)}$ normalizes the many-body wavefunction. In the fermionic case, wave functions corresponding to the states above are known as Slater determinants. We also notice that it is useful to assume that the quantum numbers λ_i defining the state $|\lambda_1, \lambda_2, \ldots, \lambda_N\rangle$ are ordered according to some reasonable convention (e.g. for $\lambda_i = x_i$ a one-dimensional coordinate representation, we might order according to the rule $x_1 \leq x_2 \leq \cdots \leq x_N$).

It is also clear that the notation with generalized coordinates (3.1) is quite cumbersome: its practical computation is almost impossible (e.g. to compute the overlap of two wavefunctions one needs to form not less than $(N!)^2$ different products) and, since this representation is tailor-made for problems with fixed particle number N, it is not suited for applications as statistical mechanics, where, in the general case (grand canonical formulation), the number of particles N ($\propto (10^{23})$, the Avogadro constant) is allowed to fluctuate. To ease this notation we can exploit the *occupation number representation*, whose basis states are specified by $|n_1, n_2, \ldots, n_N\rangle$, where the ith element signals how many particles occupy state number i; moreover, we can switch to a variable number of particles formulation by defining our domain as the Fock state $\mathcal{F}$.

With this foundations we can now define the operators $a_i^\dagger : \mathcal{F} \to \mathcal{F}$ through

$$a_i^\dagger |n_1, \ldots, n_i, \ldots\rangle \equiv (n_i + 1)^{1/2} \zeta^{s_i} |n_1, \ldots, n_i + 1, \ldots\rangle \tag{3.2}$$

where $s_i = \sum_{j=1}^{i-1} n_j$. In the fermionic case, the occupation numbers n_i have to be understood mod 2 ($(1 + 1) = 0 \bmod 2$). Indeed, repeated application of (3.2) leads to the important relation

$$|n_1, n_2, \ldots\rangle = \prod_i \frac{1}{(n_i!)^{1/2}} (a_i^\dagger)^{n_i} |0\rangle \tag{3.3}$$

i.e. the N-fold application of operators $a^\dagger$ to the empty vacuum state $|0\rangle$ generates an N-particle state, which is why the $a^\dagger$ are commonly called *creation operators*.

Proceeding from this definition, it is possible to derive $a^\dagger$'s Hermitian adjoint, $(a^\dagger)^\dagger = a$, that satisfies the relation

$$a_i \left|n_1, \ldots, n_i, \ldots\right\rangle \equiv n_i^{1/2} \zeta^{s_i} \left|n_1, \ldots, n_i - 1, \ldots\right\rangle . \tag{3.4}$$

From this it is easy to see a_i role as the *annihilation operators*. It is also easy to show that the creation and annihilation operators (often called *ladder operators*) satisfy the algebraic closure relation

$$\forall i, j : [a_i, a_j^\dagger]_\zeta = \delta_{ij}, \quad [a_i, a_j]_\zeta = 0, \quad [a_i^\dagger, a_j^\dagger]_\zeta = 0. \tag{3.5}$$

Now, we define the *occupation number operator* as

$$\hat{n}_\lambda = a_\lambda^\dagger a_\lambda \tag{3.6}$$

that simply counts the number of particles in state λ.

Finally, for our purposes it will be useful to derive the following properties:

Change of basis Using the definition of the identity operator and the relations between the initial and the final basis one can immediately derive the transformation law

$$a_{\tilde{\lambda}}^\dagger = \sum_\lambda \langle \lambda | \tilde{\lambda} \rangle \, a_\lambda^\dagger \quad a_{\tilde{\lambda}} = \sum_\lambda \langle \tilde{\lambda} | \lambda \rangle \, a_\lambda \tag{3.7}$$

Representation of one-body operators Since we have seen that any state can be obtained in the Fock space with the ladder operators, it must be possible to represent any one-body operator in an a-representation; in particular, the successive expression follows

$$\hat{\mathcal{O}}_1 = \sum_{\mu\nu} \langle \mu | \, \hat{\mathcal{O}}_1 \, | \nu \rangle \, a_\mu^\dagger a_\nu \tag{3.8}$$

Representation of two-body operators Similarly to the previous point, we can obtain

$$\hat{\mathcal{O}}_2 = \sum_{\mu\mu'\nu\nu'} \langle \mu, \mu' | \, \hat{\mathcal{O}}_2 \, | \nu, \nu' \rangle \, a_\mu^\dagger a_{\mu'}^\dagger a_\nu a_{\nu'} \tag{3.9}$$

Note that we could continue with this approach for every n-body operator, however the $n > 2$ interactions appear very infrequently, thus we can neglect them.

3.1.2 Tight binding model

The next step is to apply this approach to solid-state theory: it is known that a prototypical metal or insulator might be described by the many-particle Hamiltonian, $H = H_e + H_i + H_{ei}$ where

$$\begin{cases} H_e = \sum_i \frac{\mathbf{p}_i^2}{2m} + \sum_{i<j} V_{ee}(\mathbf{r}_i - \mathbf{r}_j) \\ H_i = \sum_I \frac{\mathbf{P}_I^2}{2M} + \sum_{I<J} V_{ii}(\mathbf{R}_I - \mathbf{R}_J) \\ H_{ei} = \sum_{iI} V_{ei}(\mathbf{R}_I - \mathbf{r}_i) \end{cases} \tag{3.10}$$

In this equation H_e, H_i, and H_{ei} describe the dynamics of electrons, ions and the interaction between electrons and ions, respectively, and $\mathbf{r}_i$ ($\mathbf{R}_I$) denote the coordinates of the valence electrons (ion cores). To a first approximation, since the lattice distortions due to both the motion of the ions and the ion–ion interaction couple only indirectly, we may describe the electron system through the simplified Hamiltonian (obtained from (3.8) and (3.9)), $\hat{H} = \hat{H}_0 + \hat{V}_{ee}$, where

$$\begin{cases} \hat{H}_0 = \int a_\sigma^\dagger(\mathbf{r}) \left[\frac{\hat{\mathbf{p}}_i^2}{2m} + V(\mathbf{r}) \right] a_\sigma(\mathbf{r}) d^d r \\ \hat{V}_{ee} = \frac{1}{2} \iint V_{ee}(\mathbf{r} - \mathbf{r}') a_\sigma^\dagger(\mathbf{r}) a_{\sigma'}^\dagger(\mathbf{r}') a_{\sigma'}(\mathbf{r}') a_\sigma(\mathbf{r}) d^d r' d^d r \end{cases} \tag{3.11}$$

$\hat{\mathbf{p}}_i = -i\hbar\partial$ is the quantum momentum operator, while $V(\mathbf{r}) = \sum_I V_{ei}(\mathbf{R}_I - \mathbf{r}_i)$ denotes the lattice potential experienced by the electrons, and the coordinates of the lattice ions $\mathbf{R}_I$ are assumed fixed. For completeness, we have also endowed the electrons with a spin index, $\sigma = \uparrow / \downarrow$. This Hamiltonian defines the problem of the interacting electron gas embedded in a solid state system.

Now, we are interested in crystals, for which Bloch's theorem is applied: eigenstates of a periodic Hamiltonian can be presented in the form of Bloch waves $\psi_{\mathbf{k}n}(\mathbf{r}) = e^{i\mathbf{k}\cdot\mathbf{r}} u_{\mathbf{k}n}(\mathbf{r})$, where the components of the crystal momentum $\mathbf{k}$ take values inside the Brillouin zone, $k_i \in [-\pi/a, \pi/a]$, and we have assumed that the periodicity of the lattice potential is isotropic ($V(\mathbf{r} + a\mathbf{e}_i) = V(\mathbf{r})$). The index n labels the separate energy bands of the solid, and the functions $u_{\mathbf{k}n}(\mathbf{r} + a\mathbf{e}_i) = u_{\mathbf{k}n}(\mathbf{r})$ are periodic on the lattice. Now, depending on the nature of the bonding, there are two complementary classes of materials where the general structure of the Bloch functions

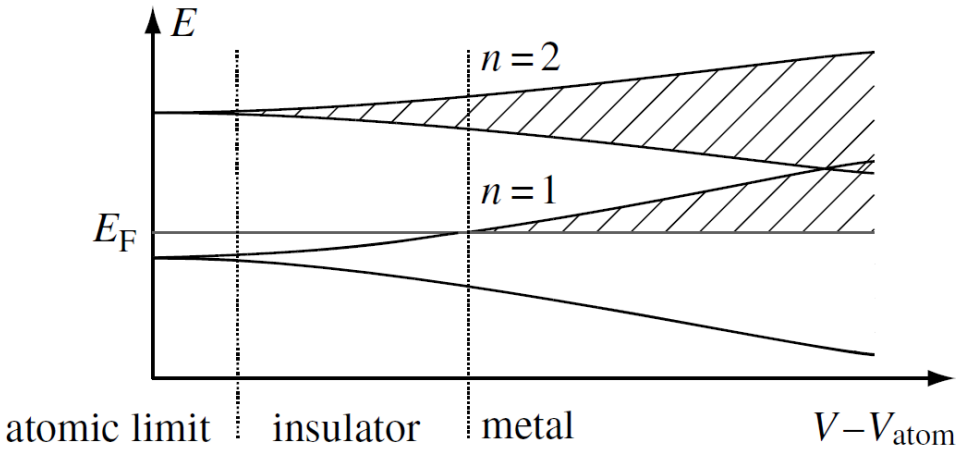

Figure 3.1: *When the Fermi energy E_F lies between two energetically separated bands, the system presents insulating behavior. Conversely, when E_F is located within a band, one may expect metallic behavior. In this work we will focus on metallic systems where the Fermi energy is located within a definite band n_0.*

can be simplified significantly: *nearly free electron systems* (notably the elemental metals drawn from groups I–IV of the periodic table, whose electrons' dynamic is largely oblivious to both the Coulomb potential created by the positively charged ion background and their mutual interaction) and *tight-binding systems*. We are interested in the latter, in which the atoms are independent from one another (i.e. the interatomic distance is greater then the wavefunction width) and the weight of the electron wavefunctions is "tightly bound" to the lattice centers, thus permitting to consider the $\hat{V}_{ee}$ term of the Hamiltonian as a perturbation of $\hat{H}_0$.

In this picture, it is convenient to expand the Hamiltonian in a local basis that reflects the atomic orbital states of the isolated ion. Such a representation is presented by the basis of *Wannier states* defined by

$$|\psi_{\mathbf{R}n}\rangle \equiv \frac{1}{\sqrt{N}} \sum_{\mathbf{k}}^{B.Z.} e^{-i\mathbf{k}\cdot\mathbf{R}} |\psi_{\mathbf{k}n}\rangle \quad |\psi_{\mathbf{k}n}\rangle \equiv \frac{1}{\sqrt{N}} \sum_{\mathbf{k}} e^{i\mathbf{k}\cdot\mathbf{R}} |\psi_{\mathbf{R}n}\rangle \tag{3.12}$$

where $\mathbf{R}$ denote the coordinates of the lattice centers, and $\sum_{\mathbf{k}}^{B.Z.}$ represents a summation over all momenta $\mathbf{k}$ in the first Brillouin zone. The Wannier functions converge on the atomic eigenstates if the distance between atoms is very high (or their interaction is very low), but if the interatomic coupling is non-zero (in that

condition, note, are not eigenfunctions of the Hamiltonian) the functions generate the solid energy bands. This change of basis from Bloch to Wannier states (that, since the Wannier states form an orthonormal basis of the single particle Hilbert space, is unitary) introduces a transformation, which can be obtained from (3.7), in the creation and annihilation operators

$$a^\dagger_{\mathbf{k}\sigma} = \frac{1}{\sqrt{N}} \sum_i e^{i\mathbf{k}\cdot\mathbf{R}_i} a^\dagger_{i\sigma}, \quad a^\dagger_{i\sigma} = \frac{1}{\sqrt{N}} \sum_i^{B.Z.} e^{-i\mathbf{k}\cdot\mathbf{R}_i} a^\dagger_{\mathbf{k}\sigma} \tag{3.13}$$

that results in the new form of the Hamiltonian

$$\hat{H}_0 = \sum_{\mathbf{k}} \epsilon_k a^\dagger_{\mathbf{k}\sigma} a_{\mathbf{k}\sigma} = \frac{1}{N} \sum_{ii'} \sum_{\mathbf{k}} e^{i\mathbf{k}(\mathbf{R}_i - \mathbf{R}_{i'})} \epsilon_k a^\dagger_{i\sigma} a_{i'\sigma} \equiv \sum_{ii'} a^\dagger_{i\sigma} t_{ii'} a_{i'\sigma} \tag{3.14}$$

where $t_{ii'} = N^{-1} \sum_{\mathbf{k}} e^{i\mathbf{k}(\mathbf{R}_i - \mathbf{R}_{i'})} \epsilon_k$; note that in the previous equations we indexed the lattice center coordinates $\mathbf{R} \equiv \mathbf{R}_i$ with $i = 1, \ldots, N$. This new representation of $\hat{H}_0$ describes electrons hopping from one lattice center (i') to another (i); $t_{ii'}$'s value, which represents the strength of the hopping between the two sites, is controlled by the effective overlap of neighboring atoms. In the limit where the energy levels ϵ_k are degenerate, $t_{ii'}$ is a Dirac's delta $\delta_{ii'}$ and no inter-atomic transport is possible; the tight-binding representation becomes useful when $t_{i \neq i'}$ is non-vanishing, but the orbital overlap is so weak that only the nearest neighbour hopping effectively contributes.

We will now have to take into account the interaction term generated by the coulomb potential $\hat{V}_{ee}$; to ease this process, let us focus attention on a single sub-band and drop reference to the band index. First of all, we apply the Wannier transformation and obtain the expansion

$$\sum_{ii'jj'} U_{ii'jj'} a^\dagger_{i\sigma} a^\dagger_{i'\sigma'} a_{j\sigma} a_{j'\sigma'} \tag{3.15}$$

where

$$U_{ii'jj'} = 1/2 \iint \psi^*_{\mathbf{R}_i}(\mathbf{r}) \psi_{\mathbf{R}_j}(\mathbf{r}) V(\mathbf{r} - \mathbf{r}') \psi^*_{\mathbf{R}'_i}(\mathbf{r}') \psi_{\mathbf{R}'_j}(\mathbf{r}') \tag{3.16}$$

It is worth noting that, since we are in the tight binding approximation, this interaction acts only on the atom itself and on the first neighbours. The resulting

tight-binding representation Hamiltonian is

$$\hat{H} = \sum_{ii'} a^{\dagger}_{i\sigma} t_{ii'} a_{i'\sigma} + \sum_{ii'jj'} U_{ii'jj'} a^{\dagger}_{i\sigma} a^{\dagger}_{i'\sigma'} a_{j\sigma} a_{j'\sigma'} \tag{3.17}$$

where the sum of repeated spin indices is implied. Let us understand the meaning of (3.16) by examining its most important contributions:

Direct terms $U_{ii'jj'} \equiv V_{ii'}$, involve integrals over square moduli of Wannier functions and thus couple density fluctuations at neighboring sites ($\sum_{i \neq i'} V_{ii'} \hat{n}_i \hat{n}_{i'}$), i.e. they explicit the interaction between charges localized at neighboring sites; in certain materials, they can induce charge density wave instabilities.

Exchange coupling terms For these terms $i' = j$ and $j' = i$; they tend to generate magnetic coupling with exchange constant $J_{ij} \equiv U_{ijji}$ (clearly, the nature of the order depends on J_{ij}'s sign).

Hubbard interaction If the distance between the atoms is large, the "on-site" Coulomb interaction is the strongest, i.e. putting two fermions on the same site (therefore with opposite spins) costs a very large energy due to the Coulomb repulsion U compared to the energy one gains by letting the fermions delocalize with a bandwidth $W \sim t$; it derives from the terms U_{iiii}.

Note that even a weak interaction can upset the tight-binding model (e.g. induce a magnetic state or an insulating phase). If the last terms prevail, the Hamiltonian takes the simplified form

$$\hat{H} = -t \sum_{<ij>} a^{\dagger}_{i\sigma} a_{j\sigma} + U \sum_{i} \hat{n}_{i\uparrow} \hat{n}_{i\downarrow} \tag{3.18}$$

where $< ij >$ is a shorthand used to denote neighbouring lattice sites and where we used the definition $U_{iiii} \equiv U/2$, $\sum_{i\sigma\sigma'} U_{iiii} a^{\dagger}_{i\sigma} a^{\dagger}_{i\sigma'} a_{i\sigma} a_{i\sigma'} = \sum_i U \hat{n}_{i\uparrow} \hat{n}_{i\downarrow}$. This is the *Hubbard model* Hamiltonian we sought.

3.1.3 Hubbard model

Let us go through the most important (theoretical and phenomenological) details of this model. The phase behaviour of the Hubbard Hamiltonian (3.18) is characterized

ultimately by three dimensionless parameters: the ratio of the Coulomb interaction scale to the bandwidth U/t, the average number of electrons per site n (called particle density or filling fraction), and the (dimensionless) temperature, T/t. In the limit $n \ll 1$ and $T/t \ll 1$ (low electron density and low temperature), we expect a behaviour similar to the nearly free electrons (metallic) case, scilicet a little $U/t \ll 1$. When $n = 1$ (half-filled model), if we have weak interaction ($U/t \ll 1$), hopping is probable and double occupancy of the same atomic coordinate costs little energy; on the other hand, if $U/t \gg 1$, the system is strongly correlated and the electrons' migration is dampened: this is the case of *Mott insulators*. But what is the physical explanation of the nature of the Mott–Hubbard transition from the metallic to the insulating phase? In the Mott's original formulation the system was conceived as an insulator characterized by two "Hubbard bands" with a bandwidth $\sim t$ separated by a charge gap U [49] [50]. States of the upper band engage site double occupancy while those states that make up the lower band do not. The transition between the metallic and the insulating phase was predicted to occur when the interaction was sufficiently strong that a charge gap develops between the bands.

Experimentally, it is often found that the low-temperature phase of the Mott insulator is accompanied by the anti-ferromagnetic ordering of the local moments; this is originated by the *superexchange* mechanism and can be proved theoretically with some calculation: considering for simplicity only two half-filled neighbouring sites, one can see that the overall system can be in six different states (recalling the Pauli principle, we have two polarized states, $|\uparrow,\uparrow\rangle$ $|\downarrow,\downarrow\rangle$, and four states with null total spin, $|s_1\rangle = |\uparrow,\downarrow\rangle$, $|s_2\rangle = |\downarrow,\uparrow\rangle$, $|d_1\rangle = |\uparrow\downarrow,\cdot\rangle$ $|d_2\rangle = |\cdot,\uparrow\downarrow\rangle$, where $|s\rangle$ and $|d\rangle$ stand for single and double occupancy, respectively). In the strong coupling limit $U/t \gg 1$, the ground state will be composed predominantly of states with no double occupancy ($|s\rangle$); to determine the ground state structure in this case, we will treat the hopping part of the Hamiltonian $\hat{H}_t$ as a perturbation of the Hubbard interaction part $\hat{H}_U$. In this way, we can write the effective Hamiltonian as

$$\hat{P}_s \hat{H}' \hat{P}_s = J\left(\hat{\mathbf{S}}_1 \cdot \hat{\mathbf{S}}_2 - \frac{1}{4}\right) \tag{3.19}$$

where $\hat{P}_s = \prod_i (1 - n_{i\uparrow} n_{i\downarrow})$ is the Gutzwiller projector, i.e. the operator that projects

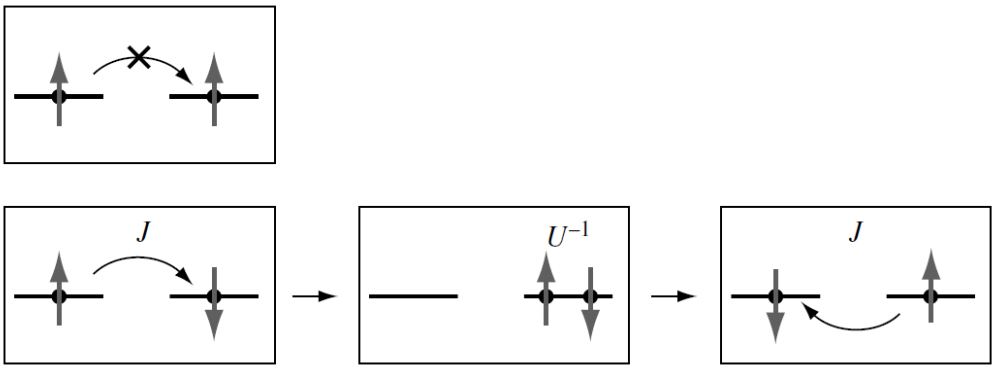

Figure 3.2: *Simple physical interpretation of the reason why electrons subject to a strong local repulsive Coulomb interaction have a tendency to adopt an antiferromagnetic spin configuration between neighboring sites. On the top, hybridization of spin polarized states is forbidden by Pauli exclusion. Bottom:superexchange mechanism by which two antiparallel spins can lower their energy by a virtual process in which the upper Hubbard band is occupied. Anti-parallel spins can take advantage of the hybridization (however small) and reduce their kinetic energy by hopping to a neighboring site. Taken from [1].*

onto the singly occupied subspace, and $J = 4t^2/U$ (see fig. 3.2); this means that, when the system is in a single occupied state $|s_i\rangle$, its energy is minimized by a state where $S_1 = -S_2 = 1/2$, i.e. there is an anti-ferromagnetic superexchange interaction that couples the spin (first formulated by Anderson in [6]).

This approach can be easily extended to the overall lattice system through the *Heisenberg Hamiltonian*

$$\hat{H} = -J \sum_{<mn>} \hat{\mathbf{S}}_m \cdot \hat{\mathbf{S}}_n \tag{3.20}$$

where $J \sim t^2/U$. Thus, while the charge degrees of freedom are quenched by the insulating magnetic phase, spin fluctuations can propagate in the lattice. When doped away from the half-filling the $\hat{H}_t$ term must be reconsidered; the removal of electrons from the half-filled system introduces vacancies into the "lower Hubbard band" that may propagate through the lattice. For a low concentration of holes, the strong coupling Hubbard system may be described by the effective *t–J Hamiltonian*

$$\hat{H}_{t-J} = -t \sum_{<mn>} \hat{P}_s a^\dagger_{m\sigma} a_{n\sigma} \hat{P}_s + J \sum_{<mn>} \hat{\mathbf{S}}_m \cdot \hat{\mathbf{S}}_n \tag{3.21}$$

Here transport depends sensitively on the competition between the exchange energy of the spins and the kinetic energy of the holes.

The rich behaviour of the Mott–Hubbard system is nowhere more exemplified than in the ceramic cuprate system: their single band is exactly half-filled (one electron per Cu site) and, therefore, according to the standard band picture, these materials should be metallic. However, strong electron interaction drives the cuprate system into an insulating antiferromagnetic Mott–Hubbard phase. When doped away from half-filling, the Hubbard gap and the antiferromagnetic order collapse, but the system develops the high-temperature unconventional superconducting phase we are interested into, whose mechanism is believed to be rooted in the exchange of antiferromagnetic spin fluctuations.

Finally, we have to note that, when we are in a system in which the number of excitations is not fixed (i.e. in the Hamiltonian some operators appear as polynomials containing unequal numbers of creation and annihilation operators, for example aa or $aa^\dagger a^\dagger$ and not only $a^\dagger a$ and $aa^\dagger$), like when dealing with photons and phonons, we have to use the *Bogoliubov transformation*: we redefine the annihilation and creation particle operators as quasi-particle operators whose number is conserved in the system. To obtain them, we apply an unitary transformation to a and $a^\dagger$, while remembering that even the new operators have to satisfy the commutation relations.

3.2 The Hubbard model in cuprates

As already introduced, the cuprate material class shows an unexpected high temperature superconductivity, and the proximity between the superconducting and the insulating antiferromagnetic phases inspired the idea that the electron pairing mechanism might be of magnetic origin, in contrast with conventional superconductivity where it is the electron-phonon interaction which results in electron pairing. We thus want to develop a theoretical model able to describe this magnetic behaviour that would help us to understand its correlation with the superconductivity phenomenon [18]. First of all, the atoms' position is assumed as fixed to the lattice

points, thus neglecting phonon physics; moreover, it is supposed that only the valence electrons participate in the low-energy physics, while the other electrons are left in their atomic orbital state. To address theoretically the physics of the cuprate materials, the Hubbard model was proposed to encompass the most relevant aspects of the CuO_2 square lattice plane physics. Exploiting the previous section, (3.18) is a good starting point:

$$\hat{H} = -t \sum_{<ij>,\sigma} (a^{\dagger}_{i\sigma} a_{j\sigma} + h.c.) + U \sum_{i} \hat{n}_{i\uparrow} \hat{n}_{i\downarrow} \tag{3.22}$$

where the dependence on the spin σ has been added (h.c. stands for hermitian conjugate); it is useful to remind that, neglecting the temperature dependence and considering the half-filling case ($n = 1$), the only parameter of this model is the ratio U/t, which value in cuprates is ~ 10.

As already discussed, in the strong limit $U/t \gg 1$ it is possible to introduce the Coulomb repulsion perturbatively. We already know that the zeroth order of the Hamiltonian is obtained by substitution of Wannier and Bloch states in the hopping part and it is (3.14) (with $\epsilon_k = -1/2 \sum_\tau t_\tau e^{i\tau \cdot \mathbf{k}}$, $\tau = \mathbf{R}_i - \mathbf{R}_j$). By turning on the interaction, the number of double occupancies (DOs) should become a good quantum number (at low temperature), since it defines sectors of the Hilbert space separated by the large Coulomb repulsion energy U; therefore, the lowest energy subspace is obtained when there is the minimum of DOs as permitted by the filling. In this subspace, the Coulomb interaction $V = U \sum_i \hat{n}_{i\uparrow} \hat{n}_{i\downarrow}$ is diagonal, while the kinetic term $K = -t \sum_{<ij>,\sigma} (a^{\dagger}_{i\sigma} a_{j\sigma} + h.c.)$ can be treated as a perturbation. If we denote $|\alpha\rangle$ and $|\beta\rangle$ two states belonging to the lowest energy sector of the Hubbard model, the expansion can be written as:

$$\langle \alpha | \hat{H} | \beta \rangle = 0 + \langle \alpha | K | \beta \rangle + \sum_{\gamma} \frac{\langle \alpha | K | \gamma \rangle \langle \gamma | K | \beta \rangle}{E_0 - E_\gamma} + \dots \tag{3.23}$$

Since we are in the half-filling case, the first order correction does not contribute because $K|\beta\rangle$ has a DO, while $|\alpha\rangle$ has none: they belong to two different subspaces, i.e. they are orthogonal. The second order term is equivalent to (3.19) :

$$\hat{H}^{(2)} = J \sum_{<ij>} \left(\hat{\mathbf{S}}_i \cdot \hat{\mathbf{S}}_j - \frac{1}{4} \right) \tag{3.24}$$

with as usual $J = 4t^2/U$, i.e. the interaction is antiferromagnetic.

Advancing as in the previous section, it is possible to turn to doped case where holes are added and then to perform the same kind of effective perturbation theory development. In this case, the first order perturbation $\langle\alpha| K |\beta\rangle$ will now contribute by exchanging an electron and a hole, while the second order perturbation will generate more complex hops, the so called three-sites term. Altogether, the effective Hamiltonian of the Hubbard model in the strong coupling limit with finite doping is a t-J-like model [41]:

$$\hat{H}^{(2)} = -\sum_{<ij>,\sigma} \hat{P}_s(t_{ij}a^\dagger_{i\sigma}a_{j\sigma} + h.c.)\hat{P}_s + J\sum_{<ij>}(\hat{\mathbf{S}}_i \cdot \hat{\mathbf{S}}_j - \frac{1}{4}n_i n_j) + \tag{3.25}$$

$$-\frac{J}{4}\sum_{j,\tau\neq\tau',\sigma} \hat{P}_s(a^\dagger_{j\sigma'}a_{j\sigma'}a^\dagger_{j+\tau\sigma}a_{j+\tau'\sigma} + a^\dagger_{j+\tau\sigma'}a_{j\sigma'}a^\dagger_{j\sigma}a_{j+\tau'\sigma})\hat{P}_s \tag{3.26}$$

where $\hat{P}_s$ is the Gutzwiller projector.

3.2.1 Effective low energy theory

The results of the perturbation theory are theoretically consistent, but they are not suited to applications; we thus have to try to develop an effective low energy that could be used in an practical situation ([45], [21]). The general Hamiltonian (3.22) can be rewritten as:

$$\hat{H} = -\sum_{\mathbf{r}\sigma\tau} t_\tau \hat{T}_{\mathbf{r}\sigma\tau} + U\hat{V} \tag{3.27}$$

$$\hat{T}_{\mathbf{r}\sigma\tau} = a^\dagger_{\mathbf{r}+\tau\sigma}a_{\mathbf{r}\sigma} \tag{3.28}$$

$$\hat{V} = a^\dagger_{\mathbf{r}\uparrow}a_{\mathbf{r}\uparrow}a^\dagger_{\mathbf{r}\downarrow}a_{\mathbf{r}\downarrow} \tag{3.29}$$

Practical choices for the hoppings can for instance include first, second and third nearest neighbours on a square lattice, but we will deal with it in the next chapter. As always, we are in the strong coupling limit (i.e. putting two fermions on the same site costs a lot of energy due to the Coulomb repulsion), therefore the number of DO is given by the operator $\hat{V}$, thus defining subspaces with very different energy ($\Delta(E) = U$); in our limit the number of DOs could be considered fixed, so $\hat{V}$

commutes with the Hamiltonian, and we have to find an approximate change of basis $\hat{U}$ that fulfills the condition:

$$[\hat{U}\hat{H}\hat{U}^{\dagger}, \hat{V}] = 0 \tag{3.30}$$

The change of Hamiltonian effects a change in the basis states too; our initial basis states $|\alpha\rangle$ are the real space configurations of the spin $|\uparrow\rangle$, $|\downarrow\rangle$, the empty state $|-\rangle$ and the doubly occupied one $|\uparrow\downarrow\rangle$. To assure that the final basis is orthonormal, we require that the operator is unitary, that is equivalent to impose that $\hat{U} = e^{i\hat{S}}$, where $\hat{S}$ is an hermitian matrix. The new Hamiltonian becomes:

$$\hat{H}' = e^{i\hat{S}}\hat{H}e^{-i\hat{S}} = \hat{H} + [i\hat{S}, \hat{H}] + \frac{1}{2}[i\hat{S}, [i\hat{S}, \hat{H}]] + \dots \tag{3.31}$$

where the second equality arises from a standard combinatorics result.

Since it is almost impossible to find the explicit analytical form of the $\hat{S}$ operator that satisfies the equation (3.30), we use an approximation: we suppose that $\hat{S}$ is proportional to a generic small parameter λ, we derive its series expansion and we verify the requested condition for the first n terms. To do that, first we exploit the number operators $\hat{n}_{\mathbf{r}\sigma}$ (3.6) and $\hat{h}_{\mathbf{r}\sigma} = 1 - \hat{n}_{\mathbf{r}\sigma}$ (that is 0 when $\hat{n}_{\mathbf{r}\sigma} = 1$, i.e. when the state is occupied, and vice versa) to transform the kinetic operator $\hat{T}$ so that the terms that create, destroy a DO and the ones that simply move a spin are explicit:

$$\hat{T}_{\mathbf{r}\sigma\tau} = \hat{T}^{1}_{\mathbf{r}\sigma\tau} + \hat{T}^{-1}_{\mathbf{r}\sigma\tau} + \hat{T}^{0}_{\mathbf{r}\sigma\tau} \tag{3.32}$$

$$\hat{T}^{1}_{\mathbf{r}\sigma\tau} = \hat{n}_{\mathbf{r}\tau\sigma'} a^{\dagger}_{\mathbf{r}+\tau\sigma} a_{\mathbf{r}\sigma} \hat{h}_{\mathbf{r}\sigma'} \tag{3.33}$$

$$\hat{T}^{-1}_{\mathbf{r}\sigma\tau} = \hat{h}_{\mathbf{r}\tau\sigma'} a^{\dagger}_{\mathbf{r}+\tau\sigma} a_{\mathbf{r}\sigma} \hat{n}_{\mathbf{r}\sigma'} \tag{3.34}$$

$$\hat{T}^{0}_{\mathbf{r}\sigma\tau} = \hat{n}_{\mathbf{r}\tau\sigma'} a^{\dagger}_{\mathbf{r}+\tau\sigma} a_{\mathbf{r}\sigma} \hat{n}_{\mathbf{r}\sigma'} + \hat{h}_{\mathbf{r}\tau\sigma'} a^{\dagger}_{\mathbf{r}+\tau\sigma} a_{\mathbf{r}\sigma} \hat{h}_{\mathbf{r}\sigma'} \tag{3.35}$$

it is easy to see that $\hat{T}^{1}_{\mathbf{r}\sigma\tau}$ creates a double occupancy,$\hat{T}^{-1}_{\mathbf{r}\sigma\tau}$ destroys one and $\hat{T}^{0}_{\mathbf{r}\sigma\tau}$ either move a double occupancy or a hole.

Once defined these operators, by using a first order correction $\hat{S}^{(1)} = 1/U(\hat{T}^{1} - \hat{T}^{-1})$, we can compute a second order Hamiltonian:

$$\hat{H}^{(2)} = \hat{V} + \hat{T}^{0} + \frac{1}{U}([\hat{T}^{1}, \hat{T}^{-1}] + [\hat{T}^{1}, \hat{T}^{0}] + [\hat{T}^{0}, \hat{T}^{-1}]) + o(\frac{t^3}{U^2}) \tag{3.36}$$

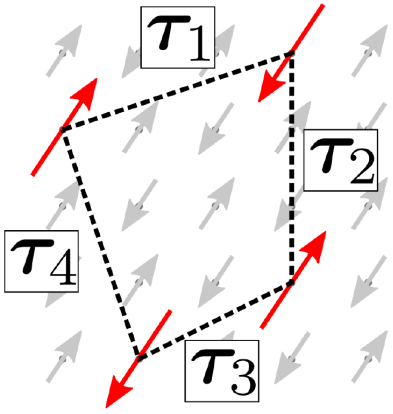

Figure 3.3: *Example of path treaded by a valence electron (or hole) on four different lattice sites. τ_1, τ_2, τ_3 and τ_4 are the hopping vectors. Taken from [18].*

and, considering only the subspace with the minimum number of double occupancies allowed by the filling and the half-filled case, we simplify this equation into:

$$\hat{H}^{(2)} = -\frac{1}{U}(\hat{T}^{-1}\hat{T}^{1} + \hat{T}^{0}\hat{T}^{1}) \tag{3.37}$$

This operation can be done also for the fourth order and the result is:

$$\hat{H}^{(4)} = -\frac{1}{U}\hat{T}^{-1}\hat{T}^{1} + \frac{1}{U^2}\hat{T}^{-1}\hat{T}^{0}\hat{T}^{1} + \tag{3.38}$$

$$+ \frac{1}{U^3}(\hat{T}^{-1}\hat{T}^{1}\hat{T}^{-1}\hat{T}^{1} - \hat{T}^{-1}\hat{T}^{0}\hat{T}^{0}, \hat{T}^{1} - \hat{T}^{1}\hat{T}^{-1}\hat{T}^{1}\hat{T}^{1}/2) \tag{3.39}$$

We obtained a t^4/U^3 order approximation of the effective Hamiltonian; since none of the $\hat{T}^m$ terms' combinations of these Hamiltonians creates DO, they do not change the system state. Therefore the Hilbert space associated with (3.38) has only the $\sigma \in \{\uparrow, \downarrow\}$ spin-$\frac{1}{2}$ degrees of freedom per site, and thus the single sites Hamiltonians (and the whole Hamiltonian) can be expressed through the $SU(2)$ 2D special unitary group base (i.e. the Pauli matrices).

This can be done by substituting the $\hat{T}^m$ operators with the sum of their possible effects on every lattice combination of sites. For example, let's understand how the following hopping process acts (shown in 3.3):

$$\hat{T}^{-1}\hat{T}^{0}\hat{T}^{0}\hat{T}^{1} = \sum_{i_1 i_2 i_3 i_4} \sum_{\tau_1 \tau_2 \tau_3 \tau_4} \sum_{\sigma_1 \sigma_2 \sigma_3 \sigma_4} \hat{T}^{-1}_{i_4 \tau_4 \sigma_4} \hat{T}^{0}_{i_3 \tau_3 \sigma_3} \hat{T}^{0}_{i_2 \tau_2 \sigma_2} \hat{T}^{1}_{i_1 \tau_1 \sigma_1} \tag{3.40}$$

where i denotes the lattice site, τ the hopping vector, σ the initial spin of the electron on the site and the numbers $1, 2, 3, 4$ the steps of the process. Despite the apparent

complexity from the many indices, only a very few subset of those actually give a finite contribution. I.e., if we consider a cluster with wavefunction:

$$|\alpha\rangle = \begin{vmatrix} 1 & 2 \\ 3 & 4 \end{vmatrix} = \begin{vmatrix} \uparrow & \downarrow \\ \downarrow & \uparrow \end{vmatrix} \tag{3.41}$$

the process is:

$$\hat{T}^{-1}\hat{T}^{0}\hat{T}^{0}\hat{T}^{1}\begin{vmatrix} \uparrow & \downarrow \\ \downarrow & \uparrow \end{vmatrix} = \hat{T}^{-1}\hat{T}^{0}\hat{T}^{0}\begin{vmatrix} \uparrow\downarrow & \downarrow \\ - & \uparrow \end{vmatrix} \tag{3.42}$$

$$= \hat{T}^{-1}\hat{T}^{0}\begin{vmatrix} \uparrow\downarrow & \downarrow \\ \uparrow & - \end{vmatrix} \tag{3.43}$$

$$= \hat{T}^{-1}\begin{vmatrix} \downarrow & \uparrow\downarrow \\ \uparrow & - \end{vmatrix} \tag{3.44}$$

$$= \begin{vmatrix} \downarrow & \uparrow \\ \uparrow & \downarrow \end{vmatrix} \tag{3.45}$$

The last hop, which must annihilate both a double occupancy and a hole, require that these two are not separated far enough that no hopping is available for $\hat{T}^{-1}$ to be able to operate. Therefore, the translation vectors τ_i must form a closed path for our combination (3.40) to give a contribution, and thus the complicated sum above contains far less terms than apparent. The situation is identical also for the other operators' combinations: they might only contribute on closed paths.

The *overall effective Hamiltonian* can be computed with an appropriate computer calculation, which neglects the inconsequential terms; in this way we obtain:

$$\hat{H}^{(4)} = \sum_{ab}\Big(\frac{4t_{ab}^2}{U} - \frac{16t_{ab}^4}{U^3}\Big)\Big(\mathbf{S}_a\cdot\mathbf{S}_b - \frac{1}{4}\Big) + \sum_{abc}\frac{4t_{ab}^2t_{bc}^2}{U^3}\Big(\mathbf{S}_a\cdot\mathbf{S}_c - \frac{1}{4}\Big) + \tag{3.46}$$

$$-\sum_{abcd}\frac{4t_{ab}t_{bc}t_{cd}t_{da}}{U^3}\Big\{\sum_{i=b,c,d}\mathbf{S}_i\cdot\mathbf{S}_a - 20[(\mathbf{S}_a\cdot\mathbf{S}_b)(\mathbf{S}_c\cdot\mathbf{S}_d) + \tag{3.47}$$

$$+(\mathbf{S}_a\cdot\mathbf{S}_d)(\mathbf{S}_b\cdot\mathbf{S}_c) - (\mathbf{S}_a\cdot\mathbf{S}_c)(\mathbf{S}_b\cdot\mathbf{S}_d)]\Big\} + E^{(4)} \tag{3.48}$$

where a, b, c and d are the sites' indices and $E^{(4)}$ is a constant; note that, as we have derived in the previous example, the sums are only over closed paths, while the abc sum is indeed composed by 4-order paths with $d = b$ ($a \to b \to c \to b \to a$).

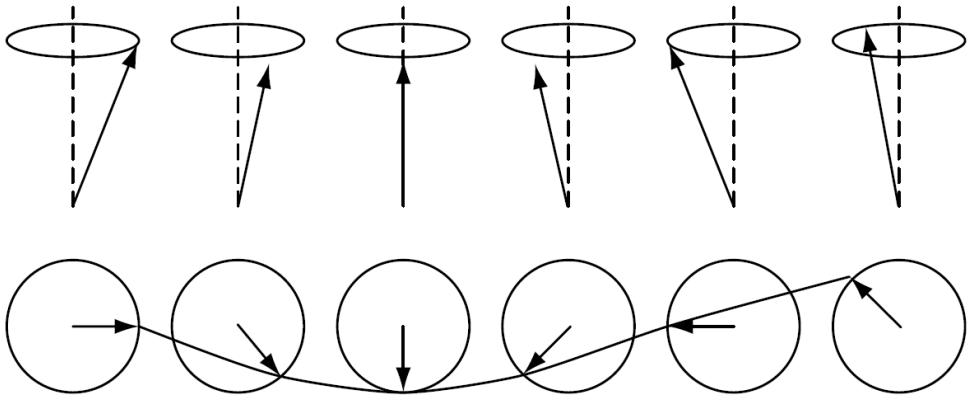

Figure 3.4: *Spin configuration of an elementary spin-wave excitation from the spin polarized ground state. Note that a simultaneous change of the orientation of all spins does not change the ground state energy (high degeneration), i.e. the system possesses a global rotation symmetry. From [1].*

3.3 Spin-wave theory

At this point, it is necessary to introduce another important physical instrument to describe the behaviour of magnetic materials: the *spin-waves* (fig. 3.4). A simple starting point to this topic is a spin system described by an Heisenberg Hamiltonian (3.20). While at high temperature the study of this system is approachable with a moment-expansion method, spin-wave theory is a good approximation at low temperatures. In this picture, the ground state is the one with all the spins aligned in a precise direction, while the first excited state is the one with only one spin in the other direction. However, due to the transverse nature of the exchange interaction between the elements of the lattice, this spin flip is delocalized all over the system, and is therefore describable as a spin-wave. The plainest spin-wave theory was conceived by Bloch, and we will now follow its derivation [70] [10] [61].

Let's consider the waves as non interacting, since at very low temperatures the interaction's amplitude is very small. First of all, the spin operator's evolution in time can be derived from the commutation relation (i.e. spin operator equation of motion):

$$\frac{d\hat{\mathbf{S}}_j}{dt} = \frac{i}{\hbar}[\hat{H}, \hat{\mathbf{S}}_j] = -\frac{1}{\hbar}(\hat{\mathbf{H}}_i \times \hat{\mathbf{S}}_j) \tag{3.49}$$

where j is the lattice point number and $\hat{H}$ represents the Heisenberg Hamiltonian including the Zeeman energy $-g\mu_B\hat{\mathbf{H}} \cdot \hat{\mathbf{S}}_i$. Then, we substitute the Heisenberg Hamiltonian expression in (3.49), and, assuming that field and spin, in the ground state, are directed along the same direction z, we derive two linear equations to evaluate the spin variation in the two other directions, x and y (with $\hat{S}_z \simeq \hat{S}$, since they are small variations). Next, we switch to an $\hat{S}_\pm$ description:

$$\hat{S}_\pm = \hat{S}_x \pm i\hat{S}_y \tag{3.50}$$

Assuming a Bravais lattice, we apply the Fourier transform:

$$\hat{S}_{\mathbf{k}\pm} = \frac{1}{\sqrt{N}} \sum_j e^{-i\mathbf{k}\cdot\mathbf{R}_j} \hat{S}_{j\pm} \tag{3.51}$$

to obtain the equation for a spin-wave with wave vector $\mathbf{k}$ ($\mathbf{R}_j$ is the position of the jth lattice point). From this is easy to obtain the energy of the system and the x and y spin progresses, that show how these excitations correspond to a rotation of the spin vector in the xy plane. It is also possible to derive the medium number of spins flipped as a temperature function, thus observing a $\tilde{T}^{3/2}$ trend, that corresponds, as it should, to the spontaneous magnetization of ferromagnets decrease with the increasing temperature.

3.3.1 Spin wave theory in cuprates

Let's apply this approach to our cuprate picture: we still need to resolve (3.46), and the sin-wave theory has provided us with an instrument to evaluate the Heisenberg-like terms $\hat{\mathbf{S}}_m \cdot \hat{\mathbf{S}}_n$ [18]. It is thus possible to use the spin-wave theory to approximately diagonalize the Hamiltonian. We can act as in the Bloch theory, but some changes are mandatory: in effect, we are here dealing with an antiferromagnetic system, and not ferromagnetic, for which we developed the treatise. First of all, it is essential to find the system ground state, that we will assume as the antiferromagnetic Néel order. As the magnetic lattice has doubled unit cell compared to the nuclear cell (because it has to describe the spin distribution on the lattice, which is antiferromagnetic, and therefore two nearest neighbours have opposite spin), we

adopt the staggered spin notation:

$$\begin{cases} \hat{S}_j^x = e^{i\mathbf{k}\cdot\mathbf{R}_j}\tilde{S}_j^x \\ \hat{S}_j^y = \tilde{S}_j^y \\ \hat{S}_j^z = e^{i\mathbf{k}\cdot\mathbf{R}_j}\tilde{S}_j^z \end{cases} \tag{3.52}$$

where the terms with $\sim$ are the original spins and $\mathbf{k} \in [-\pi/a, \pi/a]$ (a is the square lattice parameter).

It is then necessary to take into account the interaction between spin-waves, that we did neglected in the Bloch treatise. To do that, we have to apply the *Holstein-Primakoff method* []: it consists in introducing a creation and an annihilation operator based on the number operator $\hat{n} = S - \hat{S}_j^z = \hat{a}_j^\dagger \hat{a}_j$, through which represent our spin operators. This corresponds, like for photons and phonons, to introduce a particle equivalent to the spin-waves: the *magnons*. We then introduce the $\hat{S}_\pm$ notation as in (3.50) and rewrite all the spin coordinates in terms of the ladder operators (this is the Holstein-Primakoff transformation), hence obtaining:

$$\begin{cases} \hat{S}_j^z = S - \hat{a}_j^\dagger \hat{a}_j \\ \hat{S}_j^+ = \sqrt{2S - \hat{a}_j^\dagger \hat{a}_j}\,\hat{a}_j \\ \hat{S}_j^- = \hat{a}_j^\dagger \sqrt{2S - \hat{a}_j^\dagger \hat{a}_j} \end{cases} \tag{3.53}$$

The classical ground state being ferromagnetic in the staggered frame of reference, we do not need to introduce two species of bosons to distinguish the lattices with opposite spin direction.

It is now possible to proceed by developing the formulation of the general effective Hamiltonian (3.46) in terms of the ladder operators. From our transformation we can calculate the various products of spin operators, both quadratic ($\hat{\mathbf{S}}_j \cdot \hat{\mathbf{S}}_{j+\tau}$) and quartic ($\hat{\mathbf{S}}_j \cdot \hat{\mathbf{S}}_{j+\tau_1})(\hat{\mathbf{S}}_{j+\tau_2} \cdot \hat{\mathbf{S}}_{j+\tau_3}$), as power series expansions in $1/S$ [38]: de facto, we are expanding in Taylor series the squared root in (3.53). Stopping the expansion at the second order, the quadratic terms become:

$$\hat{\mathbf{S}}_j \cdot \hat{\mathbf{S}}_{j+\tau} = S^2 \left[(\hat{\mathbf{S}}_j \cdot \hat{\mathbf{S}}_{j+\tau})^{(0)} + \frac{1}{S}(\hat{\mathbf{S}}_j \cdot \hat{\mathbf{S}}_{j+\tau})^{(1)} + \right. \tag{3.54}$$

$$\left. \frac{1}{S^2}(\hat{\mathbf{S}}_j \cdot \hat{\mathbf{S}}_{j+\tau})^{(2)} + o\Big(\frac{1}{S^3}\Big) \right] \tag{3.55}$$

For quartic terms, if we exclude the quadratic contributions in the bosonic spin operators, we can use the same solution:

$$(\hat{\mathbf{S}}_j \cdot \hat{\mathbf{S}}_{j+\tau_1})(\hat{\mathbf{S}}_{j+\tau_2} \cdot \hat{\mathbf{S}}_{j+\tau_3}) = S^4 \Bigg((\hat{\mathbf{S}}_j \cdot \hat{\mathbf{S}}_{j+\tau_1})^{(0)} (\hat{\mathbf{S}}_{j+\tau_2} \cdot \hat{\mathbf{S}}_{j+\tau_3})^{(0)} + \tag{3.56}$$

$$\frac{1}{S} (\hat{\mathbf{S}}_j \cdot \hat{\mathbf{S}}_{j+\tau_1})^{(1)} (\hat{\mathbf{S}}_{j+\tau_2} \cdot \hat{\mathbf{S}}_{j+\tau_3})^{(0)} + \tag{3.57}$$

$$\frac{1}{S} (\hat{\mathbf{S}}_j \cdot \hat{\mathbf{S}}_{j+\tau_1})^{(0)} (\hat{\mathbf{S}}_{j+\tau_2} \cdot \hat{\mathbf{S}}_{j+\tau_3})^{(1)} + o\Big(\frac{1}{S^2}\Big) \Bigg) \tag{3.58}$$

In both equations the various terms are complicated combinations of the $\hat{a}^\dagger$ and the $\hat{a}$ operators, derivable directly by the scalar product calculation with Holstein-Primakoff spin coordinates.

As in the Hubbard model, we can diagonalize this linear combination of ladder operators terms by exploiting the Bogoliubov transformation; to do that, first we have to Fourier transform our ladder coordinates, therefore obtaining a coordinate set referred to the space vector $\mathbf{k}$:

$$\hat{a}_j = \frac{1}{\sqrt{N}} \sum_{\mathbf{k}} e^{-i\mathbf{k}\cdot\mathbf{R}_j} \hat{a}_{\mathbf{k}} \tag{3.59}$$

and similarly for $\hat{a}_j^\dagger$. Then, as already seen, we define some quasi-particle operators whose number is conserved and we impose the ladder operator commutation relations, thus obatining the result:

$$\omega_{\mathbf{k}} = \sqrt{A_{\mathbf{k}}^2 - B_{\mathbf{k}}^2} \tag{3.60}$$

where $A_{\mathbf{k}}$ and $B_{\mathbf{k}}$ are complicated terms that depend on the lattice configuration.

Finally, it is possible to correct this result with a magnon-magnon $1/S$ interaction (intralayer, since the interlayer interaction is very weak) using a Hartree-Fock (i.e. iterative and mean field) procedure; this gives (for the square lattice monolayer) a constant renormalization factor $Z_c = 1.15$, that has to be applied to the dispersion relation (3.60) to derive the effective result. Physically, the renormalization is due to the charge fluctuations of the Hubbard model, which we integrate perturbatively in our effective theory.

3.3.2 Linear spin-wave theory

In this last paragraph, we want to introduce the theory [64] on which is based the simulation program exploited for the magnetic behaviour of a crystal lattice simulation, SpinW, about which we will discuss extensively in the next chapter. This is the *linear spin-wave theory* [62], and it follows the footsteps of the theory already showed, but in a more general way. The SpinW program aims to solve the general magnetic Hamiltonian of interacting localized magnetic moments on a periodic lattice:

$$H = \sum_{\substack{mi \\ nj}} \mathbf{S}_{mi}^{T} J_{mi,nj} \mathbf{S}_{nj} + \sum_{mi} \mathbf{S}_{mi}^{T} A_{mi} \mathbf{S}_{mi} + \mu_B \mathbf{H}^{T} \sum_{mi} g_i \mathbf{S}_{mi} \tag{3.61}$$

where the 3×3 matrix formalism is utilized, i.e. all the elements are conceived as algebraic three-dimensional elements (e.g. the spins are 3×1 column vectors and the operators A and J are 3×3 matrices). The indices m and n are indexing the crystallographic unit cell (running from 1 to L), while i and j label the magnetic atoms inside the unit cell (running from 1 to N), $\mathbf{H}$ is the external magnetic fi

eld column vector, μ_B is the Bohr magneton and $J_{mi,nj}$ is the exchange matrix coupling the two sites mi and nj. This Hamiltonian can describe the magnetic properties of many Mott insulators; its first, second and third terms describe respectively an exchange interaction, a general anisotropy (e.g Dzyaloshinskii-Moriya effect) and an external magnetic field.

To resolve this Hamiltonian (for incommensurate lattices, generally), as before, we need to know its classical magnetic ground state; we thus assume that the solution is *a priori* known (see [55]). Then we introduce a rotating frame [36], i.e. a preceding coordinate transformation: every spin is rotated in respect with its neighbours by an angle that depends on the magnetic ordering wave vector and on the position of the cell in which the spin is situated. If we can obtain a ferromagnet with this transformation (possibility that strongly depends on the symmetry of the system), as we did with the antiferromagnetic case in the previous section, the SpinW method

can be applied. To diagonalize the Hamiltonian, we apply two rotation operators:

$$\begin{cases} \mathbf{S}_{nj} = R_n \mathbf{S}'_{nj} \\ \mathbf{S}'_{nj} = R'_j \mathbf{S}''_{nj} \end{cases} \tag{3.62}$$

R_n, if applied on the set $\mathbf{S}'_{nj}$ (that has all equal unit cells and it is thus independent on n), permits to generate the original spins, while R'_j does the same operation inside the unit cell and on the ferromagnetic set $\mathbf{S}''_{nj}$ to obtain $\mathbf{S}'_{nj}$. It is also useful to note that SpinW exploits the symmetry of the system to simplify some aspects of the problem, since the symmetry imposes some requirements on the parameters.

Now it is possible to apply the linear spin wave theory, which is used to describe small fluctuations of the spin from is classical value, i.e. at low temperature and with large S (high order corrections are necessary for $S = 1/2$ systems, that is the half-filling case). Once again, we apply the Holstein-Primakoff method and we maintain only the linear term in the bosons creation and annihilation operators:

$$S''^{+}_{nj} = \sqrt{2S_j}\, a_{nj} \tag{3.63}$$

$$S''^{-}_{nj} = \sqrt{2S_j}\, a^\dagger_{nj} \tag{3.64}$$

$$S''^{z}_{nj} = S_j - a^\dagger_{nj} a_{nj} \tag{3.65}$$

Then, if we apply the rotation operators R_n and R'_j, we can obtain (without the magnetic field) a quite complex yet general Hamiltonian expression, that, we notice, depends on the very same rotations, i.e. on the crystalline configuration of the system. From here, one can expand the Hamiltonian and neglect all the terms with more than two operators: the zero order terms gives the ground state energy, the first order's expectation value vanishes and the second order gives the spin-wave dispersion relation. Then, like in the previous section, we can Fourier transform in the Brillouin zone in the spatial wave vector $\mathbf{k}$ and deduce the problem in the general formulation:

$$H = \sum_{\mathbf{k} \in B.Z.} \mathbf{x}^\dagger(\mathbf{k}) h(\mathbf{k}) \mathbf{x}(\mathbf{k}) \tag{3.66}$$

where $\mathbf{x}$ is the column vector of the bosonic operators:

$$\mathbf{x}(\mathbf{k}) = [a_1(\mathbf{k}), \ldots, a_N(\mathbf{k}), a^\dagger_1(\mathbf{k}), \ldots, a^\dagger_N(\mathbf{k})]^T \tag{3.67}$$

and the Hermitian matrix $h(\mathbf{k})$ consists in the following submatrices:

$$h(\mathbf{k}) = \begin{bmatrix} A(\mathbf{k}) - C & B(\mathbf{k}) \\ B^{\dagger}(\mathbf{k}) & \bar{A}(\mathbf{k}) - C \end{bmatrix} \tag{3.68}$$

$A(\mathbf{k})$, $B(\mathbf{k})$ and C depend on the rotations, $S_{i,j}$ and J_{ij}; it can be shown that $A(\mathbf{k})$ is Hermitian and C is real. The same can be done, with analogous passages, to the Zeeman Hamiltonian. We now have to diagonalize the $h(\mathbf{k})$ operator; to do that, the program exploits a numerical approach to the Bogoliubov transformation proposed by Colpa [17], and from this it provides the sought dispersion relation.

Chapter 4

Fitting of magnon dispersion in antiferromagnetic compounds with different models

The aim of this work was to find a proper fitting algorithm for the spin-wave dispersion obtained by our group with ERIXS during July and November 2015 beamtimes at ESRF. To achieve this goal, we made use of the SpinW Matlab library developed by Dr. Sándor Tóth of Paul Scherrer Institute (PSI) to plot and numerically simulate magnetic structures and excitations of given spin Hamiltonian using classical Monte Carlo simulation and linear spin wave theory [64].

4.1 Dispersion features

In [68] Tranquada et al. have reported the complete calculation of dispersion relation for the $YBa_2Cu_3O_7$ (YBCO) compound. YBCO crystal structure, reported in 2.11a, is composed by couples of adjacent planes, called *bilayers*. In this model, which is quite simple, the magnetic interactions of the spin lattice (along with the Hamiltonian) are expressed in terms of the inplane first-neighbours exchange parameter J and of its two out-of-plane analogous ($J_{\perp 1}$ between planes in the same bilayer and $J_{\perp 2}$ between planes in two nearest bilayers). The method exploited to resolve the

problem is the one already seen in the previous chapter (Holstein-Primakoff, Fourier transform and Bogoliubov transformation); in the system Hamiltonian there is an additional anisotropy term resulting from spin-orbit coupling, which however experimentally has proven to be very small.

Resolving the eigenvalue problem, the modes of the system appear to be:

$$\left[\frac{\omega_{\mathbf{q}j}}{\omega_\parallel}\right]^2 = (1 + \frac{1}{4}\alpha_\perp \mp \frac{1}{2}\alpha_D\gamma_\parallel)^2 + \tag{4.1}$$

$$- (\gamma_\parallel \pm \frac{1}{4}\alpha_\perp|\gamma_\perp| - \frac{1}{2}\alpha_D\gamma_\parallel)^2 \tag{4.2}$$

where the eigenmode labels $j = 1$, 2, 3 and 4 correspond to the various sign combinations ($-+$, $++$, $--$ and $+-$ respectively), $\omega_\parallel = 2J_\parallel/\hbar$, $\alpha_{\perp i} = J_{\perp i}/J_\parallel$ and $\alpha_\perp = \alpha_{\perp 1} + \alpha_{\perp 2}$. The other terms are more complicated:

$$\begin{cases} \gamma_\parallel = \frac{1}{2}[\cos q_x a + \cos q_y a] \\ \gamma_\perp = |\gamma_\perp| e^{i\phi_\perp} \end{cases} \tag{4.3}$$

with:

$$\begin{cases} |\gamma_\perp| = \frac{\sqrt{J_{\perp 1}^2 + J_{\perp 2}^2 + 2J_{\perp 1}J_{\perp 2}\cos q_z c}}{J_{\perp 1} + J_{\perp 2}} \\ \phi_\perp = \arctan \frac{J_{\perp 1}\sin q_z z c - J_{\perp 2}\sin q_z (1-z)c}{J_{\perp 1}\cos q_z z c - J_{\perp 2}\cos q_z (1-z)c} \end{cases} \tag{4.4}$$

Here, a is the in-plane lattice constant, c is the out-of-plane one. It is useful to note that $|\gamma_\perp|$ is equal to $\frac{J_{\perp 1} - J_{\perp 2}}{J_{\perp 1} + J_{\perp 2}}$ in $q_z = \pi$, while it is equal to 1 in $q_z = 0$; therefore $0 < |\gamma_\perp| \leq 1$. Finally, $\alpha_D = D/J_\parallel$, and D is the anisotropy parameter: as it is clear by considering (4.1), the anisotropy eliminates a degeneration order, thus generating 4 different modes. However, since it can be proved both theoretically and experimentally that $\alpha_D \lesssim 10^{-2}$, we will continue to neglect it.

Therefore, imposing $\alpha_D = 0$:

$$\left[\frac{\omega_{\mathbf{q}j}}{\omega_\parallel}\right]^2 = (1 + \frac{1}{4}\alpha_\perp)^2 - (\gamma_\parallel \pm \frac{1}{4}\alpha_\perp|\gamma_\perp|)^2 \tag{4.5}$$

Near the center of the Brillouin zone $q_x = q_y = 0$, so that $\gamma_\parallel = 1$ and:

$$\omega_{\mathbf{q}z}^2 = \frac{\omega_\parallel^2}{16}\alpha_\perp[\alpha_\perp(1-|\gamma_\perp|^2)+8(1\mp|\gamma_\perp|)] \tag{4.6}$$

Since $\alpha_\perp \ll 1$ we can neglect the first term, thus finding:

$$\omega_{\mathbf{q}z} = \frac{\omega_\parallel}{\sqrt{2}}\sqrt{\alpha_\perp}\sqrt{1\mp|\gamma_\perp|} \tag{4.7}$$

Then, we already saw that in our case $J_{\perp 2} \ll J_{\perp 1}$; therefore, defining $J_{\perp 2}/J_{\perp 1} = \epsilon \ll 1$:

$$\begin{aligned} |\gamma_\perp| &= \frac{\sqrt{1+2\epsilon\cos q_z c+\epsilon^2}}{1+\epsilon} \simeq \\ &\simeq (1+\epsilon\cos q_z c)(1-\epsilon) \simeq \\ &\simeq 1-[1-\cos q_z c]\epsilon = \\ &= (1-\epsilon)+\epsilon\cos q_z c \end{aligned} \tag{4.8}$$

From the previous equation it is possible to deduce that the elimination of the anisotropy leaves a grade of degeneracy, i.e. there are two resulting modes, which can be addressed as acoustic (the one that goes to zero if $q_z = 0$) and optical.

We thus obtained a simple but complete model to describe threedimensional cuprate structures with the two parameters $J_\parallel$ and $J_\perp$. In general, it can be applied to all the compounds, and we used it to extract the dispersion relation for NBCO, Bi2201 and CCO. The exchange parameters exploited in this simulation trail have been obtained by the literature. These functions are shown in fig. 4.1.

The results, despite being rather rough, help to sketch an initial picture of the informations brought by the dispersion relation. In BiSCO, for example, because of the low $J_\perp$, the modes are almost coincident, so that there is no energy gap in Γ. On the other hand, in NBCO the gap is present, but since $J_{\perp 2} \simeq 0$, the dispersion on the L direction is almost constant, while in CCO the two modes meet and cross with a sinusoidal trend (an analytical derivation of this can be found in appendix A.

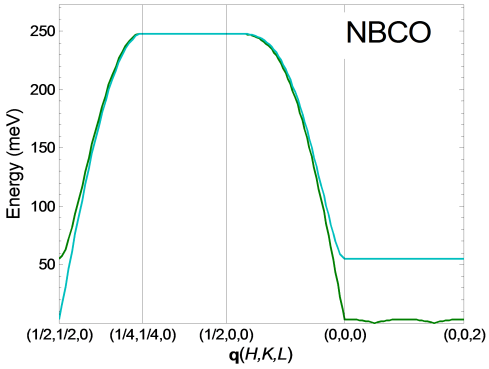

(a) *NBCO.*

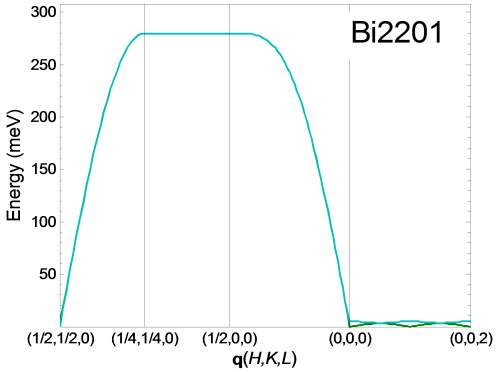

(b) *BiSCO.*

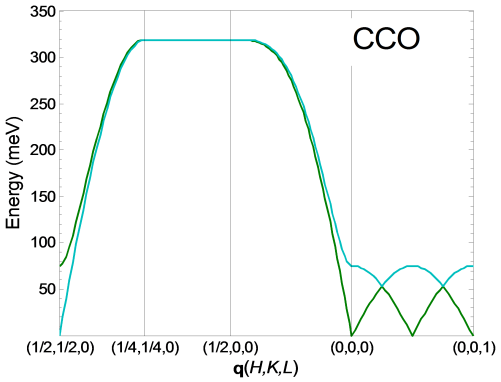

(c) *CCO.*

Figure 4.1: *NBCO, BiSCO and CCO 3D spin-wave dispersion simulations.*

4.2 t-J problem

The construction derived in the previous section, based on the Heisenberg Hamiltonian (3.20), is too elementary to describe the complex spin-wave dispersion relation observed in high-T_c cuprates, and it is thus necessary to extend it. Since it has been ascertained that the interplane magnetic coupling is negligible with respect to the intraplane interactions [68], it is reasonable to suppose that this is mainly due to the superexchange interaction between high-order lattice neighbours. We could thus consider the following Heisenberg Hamiltonian including higher-order couplings:

$$\hat{H} = J \sum_{<ij>} \mathbf{S}_i \cdot \mathbf{S}_j + J' \sum_{<ii'>} \mathbf{S}_i \cdot \mathbf{S}_{i'} + J'' \sum_{<ii''>} \mathbf{S}_i \cdot \mathbf{S}_{i''} + \tag{4.9}$$

$$+ J_c \sum_{<ijkl>} \{(\mathbf{S}_i \cdot \mathbf{S}_j)(\mathbf{S}_k \cdot \mathbf{S}_l) + (\mathbf{S}_i \cdot \mathbf{S}_l)(\mathbf{S}_k \cdot \mathbf{S}_j) - (\mathbf{S}_i \cdot \mathbf{S}_k)(\mathbf{S}_j \cdot \mathbf{S}_l)\} \tag{4.10}$$

where where J, J', and J'' are the first-, second-, and third-nearest-neighbour magnetic exchanges, i.e. the interaction between an atom and its first linear, its second linear and its first diagonal neighbours. J_c is the ring exchange interaction coupling four spins (labeled clockwise) at the corners of a square plaquette, generated by the hopping of the valence electron (or hole) on a squared path [43] [33] [57] [12]; it corresponds to the simplest term of the quartic expansion (3.56). Note that all these interactions are generated only by the next-neighbour superexchange, i.e. the hopping processes that cause them, as illustrated in fig. 4.2, are combinations of first-neighbours hopping: for example, J' it is not due to the direct coupling between two diagonal atoms, but to two subsequent simple hopping processes.

In this picture, as again already seen in chapter 3, the normalized dispersion relation is $\omega_{\mathbf{k}} = 2Z_c(\mathbf{k})\sqrt{A_{\mathbf{k}}^2 - B_{\mathbf{k}}^2}$ (3.60); $Z_c(\mathbf{k})$ is the already discussed renormalization factor, which permits to include the effect of quantum fluctuations. In the present case, it is possible to express the terms inside the squared root as:

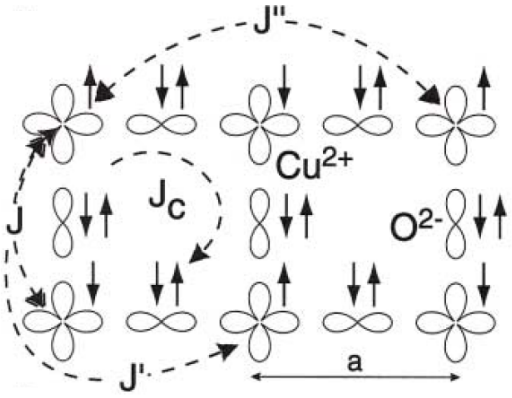

Figure 4.2: *Scheme of the superexchange effective interactions on a generic cuprate CuO_2 plane.*

$$\begin{cases} A_{\mathbf{k}} = J - J_c/2 - (J' - J_c/4)(1 - \nu_h\nu_k) - J''[1 - (\nu_{2h} + \nu_{2k})/2] \\ B_{\mathbf{k}} = (J - J_c/2)(\nu_h + \nu_k)/2 \\ \nu_x = \cos 2\pi x \end{cases} \tag{4.11}$$

Since within the linear spin-wave theory all three higher-order spin couplings J', J'' and J_c have similar effects on the dispersion relation and intensity dependence, they cannot be determined independently from a dispersion relation without additional constraints.

The simplest possible assumption is to require that $J'' = 0$ and $J_c = 0$. However, this approach proves to be rather unsatisfactory. For example, Coldea et al. used it to fit some INS data of La_2CuO_4 (LCO) compound [16], thus obtaining a positive J (i.e. antiferromagnetic) and a negative J' (i.e. ferromagnetic). These results are not compatible with theoretical prediction nor with other experimental results (e.g. $Sr_2CuO_2Cl_2$ (SCOC), material with similar exchange paths between Cu^{2+} ions to LCO); in fact, they both provide a positive (i.e. ferromagnetic) J'.

Clearly, it is necessary to extend this model by introducing J'' and J_c by taking into account the quartic Hamiltonian expansion. As seen in the previous chapter, the t-J Hamiltonian appears to be a good model with which describing the cuprate CuO_2 planes magnetic physics. It is thus possible to obtain the explicit relations

between the terms in (4.9) and the Heisenberg Hamiltonian quartic expansion terms in (3.56) as:

$$\begin{cases} J = 4\frac{t^2}{U} - 24\frac{t^4}{U^3} \\ J_c = 80\frac{t^4}{U^3} \\ J' = J'' = 4\frac{t^4}{U^3} \end{cases} \tag{4.12}$$

From now on, we will address this formulation as *simple t-J model*. As will be later shown, this model permits to obtain quite satisfactory fitting results. However, it still has some flaws: since the equations (4.12) depend all on the t and U parameters, all the exchange constants are correlated, so this is still a two-variables model; furthermore, the usual U/t values provided by this model are quite different from the expected ones (e.g. in [16] $U/t = 7$, while the value expected from the theory is ~ 12). One possible solution is to add a second- and a third-neighbours hopping parameters t' and t'' into the Hubbard Hamiltonian, while maintaining its quartic expansion, as proposed by Delannoy et al. in [21]; we will discuss this more deeply later in this chapter.

4.3 Simulation

Before any fitting trial, it is worth to take a closer look to a spin-wave dispersion relation simulation on a designed path in the reciprocal lattice. In this section we will observe how the SpinW program permits to fit this function for one of the compounds measured: $NdBa_2Cu_3O_{6.1}$ (NBCO). A concise description of the exploited instruments made available by SpinW toolbox is reported in the appendix B.

4.3.1 NBCO

In the NBCO, the magnetic structure is antiferromagnetic in each plane. Also, there is also an antiferromagnetic interaction in the c-axis direction, but only between two planes on the same bilayer. Since the heavy elements Nd and Ba and the CuO on the chains don't interact magnetically [66], we will not include them in the simulated

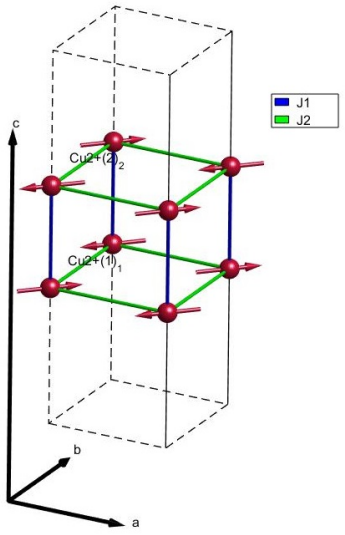

Figure 4.3: *Magnetic cell of the $NaYBa_2Cu_3O_7$ obtained with the SpinW plot tool.*

unit cell. The same happens with the in-plane oxygen atoms: it is true that they permit the superexchange between nearest coppers, but they themselves don't have any spin, thus they can be neglected. It is therefore possible to generate the magnetic structure with the Cu in-plane atoms only.

We start the SpinW simulation script, as reported in appendix B, by generating the NBCO crystal structure (the lattice constants are $a = 3.84$ Å, $b = 3.84$ Å and $c = 11.7$ Å) and then by declaring the spin interactions (since we are considering the undoped parent material, each Cu atom will have a spin $S = 1/2$). In the present simulation, the number of magnetic interactions considered is two, the interplane $J_\perp$ and the in-plane $J_\parallel$; for these parameters, it is easy to find acceptable values from the literature (in our simulation $J_\perp = 8$ meV and $J_\parallel = 140$ meV). The results can be viewed by using the `plot` SpinW script, which produces the figure 4.3.

The path in the Brillouin zone followed in the simulation is $\mathbf{k} = [0.5\,0.5\,0] \rightarrow [0\,0\,0] \rightarrow [0.5\,0\,0] \rightarrow [0.25\,0.25\,0]$. Before plotting the simulated dispersion relation, we also made use of the SpinW tool `omegasum`, which eliminates all of the bands that have very low intensity or that are physically excludable. In fact, the number of solutions found by the simulation algorithm is in theory twice the number of spin

elements in the magnetic lattice supercell, which in the NBCO case that is 8, thus the solutions should be 16. However, most of the modes calculated are physically unacceptable, while others have a negligible intensity; the whole set of modes is reported in fig. 4.4b. The final simulation result is shown in fig. 4.4a; note that the SpinW toolbox allows, as seen in the picture, to add also the energy spread of the dispersion.

This seems to reflect quite right the experimental results (see [26]). However, the figure misses a second mode (an *optical* mode from RIXS viewpoint, since it has a non-zero local minimum in $\mathbf{k} = [0\,0\,0]$, but it is in $\mathbf{k} = [0.5\,0.5\,0]$) that has been observed during the experiments. This is due to the fact that the `omegasum` function actually disregards this mode because its simulated intensity is too weak.

It is afterwards interesting to understand what happens if the complete *simple t-J model* is considered; based on Delannoy's article [21], (4.12) can be expanded to obtain the effective exchange interactions:

$$\begin{cases} J_1^{eff} = J - \frac{J_c}{2} \\ J_2^{eff} = J' - \frac{J_c}{4} \\ J_3^{eff} = J'' \end{cases} \tag{4.13}$$

This is quite reasonable: the first- and second-nearest neighbour interactions are actually involved in the circular hopping process J_c, and thus their effective exchange constants depend on that. Note that, since from the relations (4.12) one could obtain that $J_c = 4J' = 4J''$, it is possible to express all the (4.13) as a function of J and J':

$$\begin{cases} J_1^{eff} = J - 10J' \\ J_2^{eff} = -4J' \\ J_3^{eff} = J' \end{cases} \tag{4.14}$$

It is thus clear that in this model $J_2^{eff} < 0$; furthermore, since the first order magnetic interaction must be antiferromagnetic (i.e. $J_1^{eff} > 0$), $J > 10J'$ is imposed. In particular, to maintain the same interaction magnitude, we approximated J_1^{eff} to

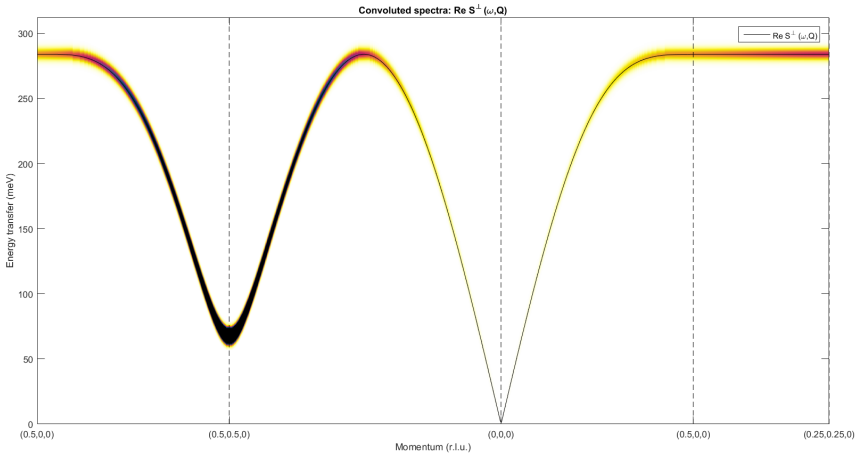

(a) *NBCO spin-wave dispersion simulated with SpinW.*

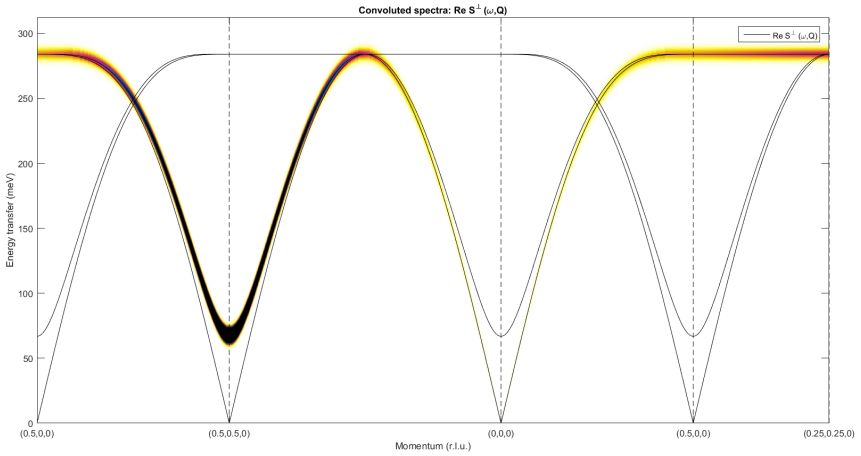

(b) *The same dispersion function, but without the use of the omegasum tool command.*

Figure 4.4: *Simulations of the NBCO dispersion relation on the path defined in the text.*

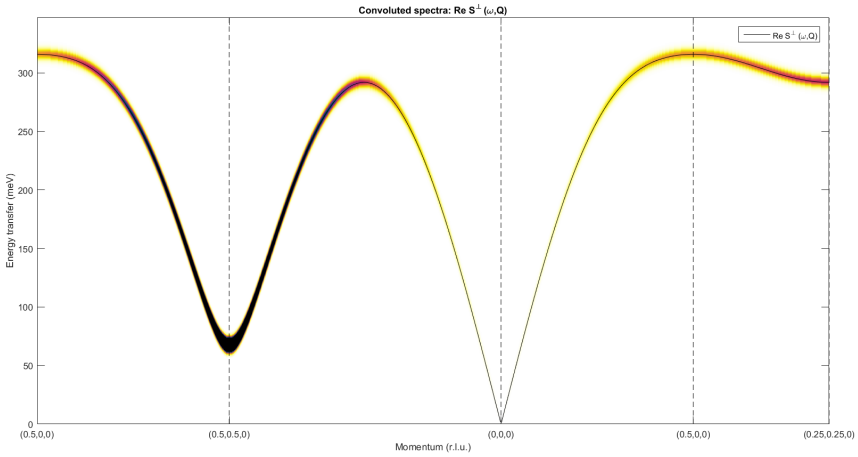

Figure 4.5: *NBCO simulation of the magnon dispersion relation on the same path as fig. 4.4.*

the previous $J_{\parallel}$. Using this parameter, along with $J_{\perp}$, for the fitting gives the results $J' = 2$ meV and $J_{\perp} = 8$ meV (we imposed $J = 160$ meV, which is an acceptable value).

In this simulation, it is also necessary to change the magnetic coupling maximum distance to include the considered interactions; it is easy to see that this distance must be bigger than two times the in-plane interatomic distance (that is 7.68 Å), but smaller than the nearest interaction distance above it (8.32 Å), therefore we chose 8 Å. We took in consideration only the vertical exchange between plane $J_{\perp}$, while the other terms were forced to 0; this is because, as already hinted, in the interplane space there are no oxygen atoms to support superexchange, thus the interaction is a direct exchange, whose strength is weak on the interplane distance.

By applying SpinW as described before, the result is easily obtained, and it is shown in fig. 4.5. In this figure is visible the similarity to the simpler model; however, in this case the system has also a dispersion between $\mathbf{k} = [0.5\,0\,0]$ and $\mathbf{k} = [0.25\,0.25\,0]$. In addition, all the peaks are slightly higher, due to the strongest interaction. These differences are clearly due to the introduction of the second- and third-order effective superexchanges; in particular, since in the proposed model both J_2^{eff} and J_3^{eff} depend only on the J' parameter, the energy gap between $\mathbf{k} = [0.5\,0\,0]$

and $\mathbf{k} = [0.25\,0.25\,0]$ depends only on it.

Another interesting test could be to run a simulation along the reciprocal c axis, i.e. the direction perpendicular to CuO_2 planes; the results are shown in fig. 4.6, and they indicate that there is no dispersion on this direction. That is because in NBCO, even if the planes are coupled in pairs, the distance between planes in different cells is 8.5 Å, therefore the interplane magnetic interaction is much weaker than in the adjacent planes and it is possible neglect it.

Finally, we tried to better understand what caused the absence of the optical mode. This was revealed to be due to the fact that the observed acoustic mode has a very high intensity peak in $\mathbf{k} = [0.5\,0.5\,0]$; since the spectra simulated contained this point, the optical mode gets neglected. Actually, the acoustic mode diverges only for $k_z = 0$ r.l.u. , as it has been imposed in the simulations. It thus appears another interesting test to study the spin-wave intensity behaviour dependence on the L direction (i.e. on the c axis).

4.3.2 Intensity study

First of all, it is possible to try the simulation with a k_z coordinate different from 0 r.l.u.; for example, in fig. 4.7 it is shown the result for $k_z = 1.5$ r.l.u. (that is an experimentally acceptable value) and same J, J' and $J_\perp$ values as in the previous simulations. Apart from the numerical errors, unfortunately present ubiquitously in the SpinW package (probably due to a difficult management of the different modes and the `omegasum` erasing), it is possible to recognize the acoustic mode previously seen (i.e. the one that goes to 0 in $\mathbf{k} = [0\,0\,1.5]$), as well as the new optical mode, which has zero energy in $\mathbf{k} = [0.5\,0.5\,1.5]$. Note that the spin-wave intensity calculated by SpinW is different from the one obtained with RIXS because it is calculated for the INS technique; however, since the INS structure factor, from which depends the cross-section of the measurement, is almost constant, and the RIXS one is more complex, but nonetheless the corrections are rather small, the intensity obtained has been assumed acceptable.

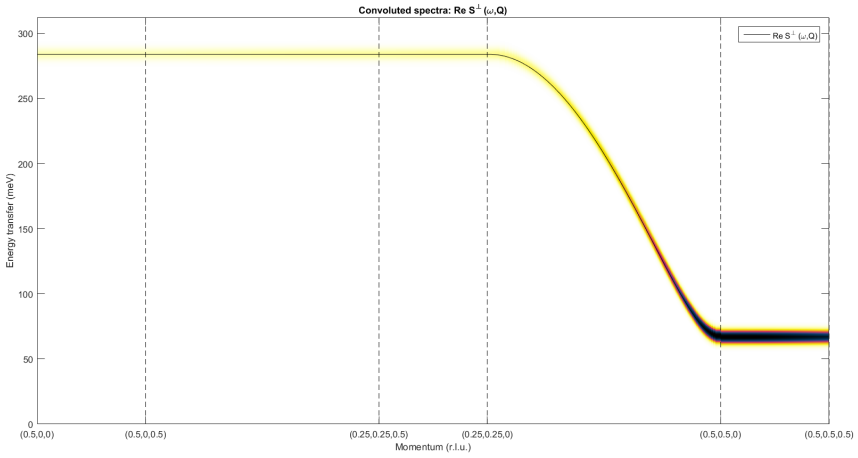

(a) *NBCO spin-wave dispersion simulation with path fragments on the c axis.*

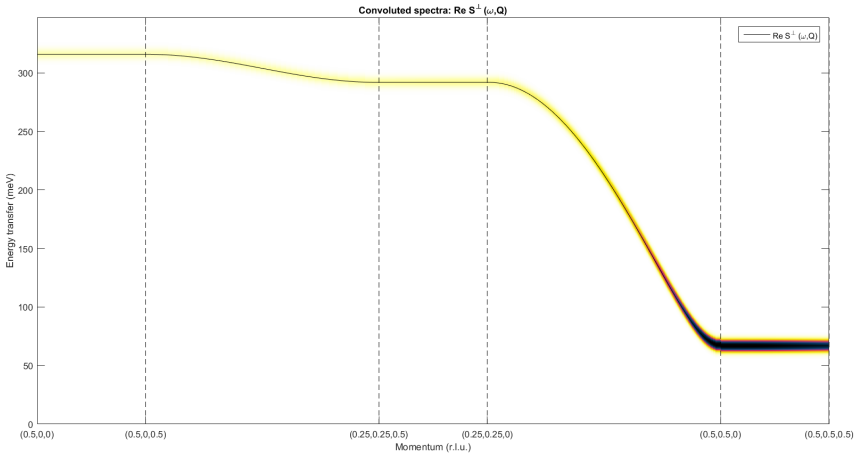

(b) *The same dispersion relation, but with complete simple t-J model.*

Figure 4.6: *Simulations of the NBCO dispersion relation on c axis paths.*

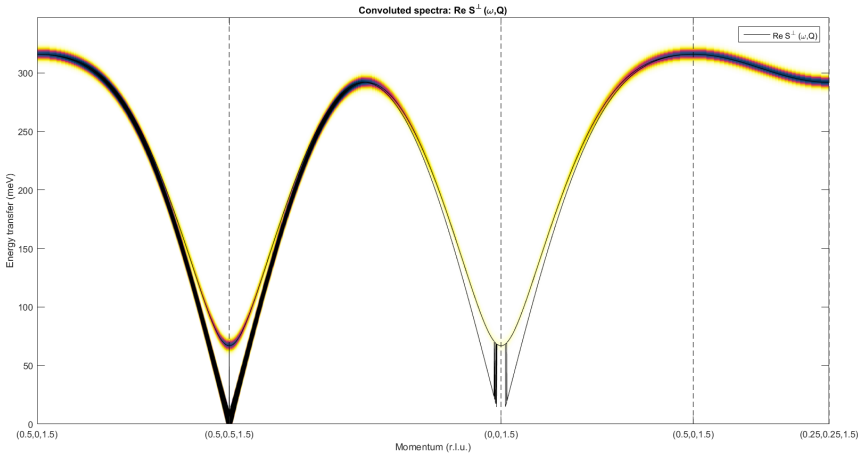

Figure 4.7: *NBCO simulation of the magnon dispersion relation on the same path as fig. 4.4, but with $k_z = 1.5$ r.l.u.*

To clarify the intensity trend of the two modes on the path, SpinW provides an intensity plot; applied on the same path, we obtained fig. 4.8b. In this figure, it is possible to see that in $\mathbf{k} = [0.5\,0.5\,1.5]$ one branch has a finite amplitude, while the other one diverges; from fig. 4.7 it is clear that the diverging mode is the one to whom we refer as optical. However, in the $k_z = 0$ r.l.u. intensity study, shown in fig. 4.8a, in effect there is only a single mode. This means that intensity dependence could be quite complicated in this toolbox.

To directly understand the L direction intensity behaviour of the modes, one can simulate its dependence on the c coordinate at fixed k_x, k_y positions. Some example of this attempts can be seen in figg. 4.9: the first one examines the $[0\,0\,0] \rightarrow [0\,0\,10]$ interval, while the other the $[0.5\,0.5\,0] \rightarrow [0.5\,0.5\,10]$ one.

This way, I know that the strongest mode in fig. 4.9a will be the optical one (the acoustic has a zero) and vice versa for fig. 4.9a. Note how there is a difference of almost two orders of magnitude between the scales of the two plots. However, in the upper picture the modes have minima in $k_z = n \cdot 1.85$ r.l.u. In the second figure (fig. 4.9b) both modes have a peak at $k_z \simeq 1.6$ r.l.u., but both of them decrease, becoming stable after a few periods; their zeros are in $k_z = n \cdot 3.7$ r.l.u. Therefore, it should be possible to insulate the missing optical mode by imposing $k_z = 1.85$

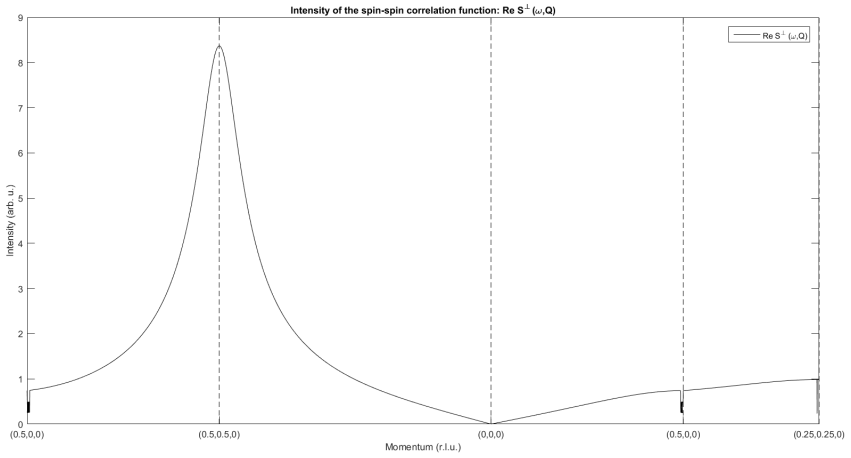

(a) *NBCO simulation of the modes intensity with $k_z = 0$ r.l.u.*

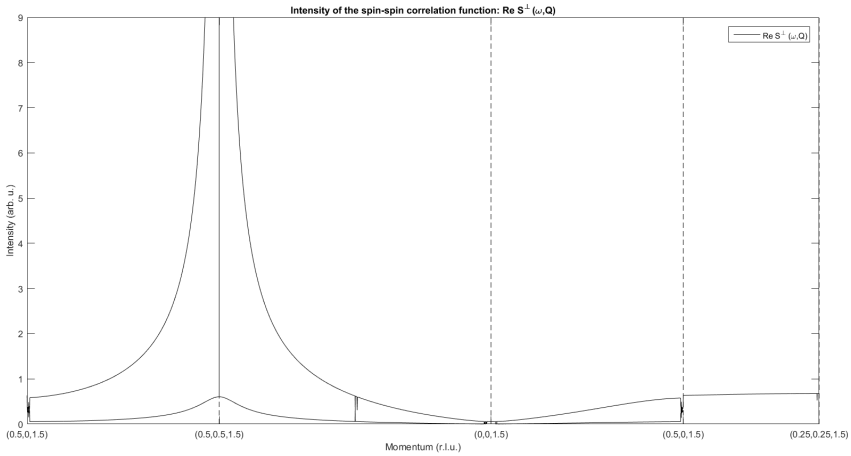

(b) *NBCO simulation of the modes intensity with $k_z = 1.5$ r.l.u.*

Figure 4.8: *Simulations of the NBCO magnetic intensity on the path defined in the text.*

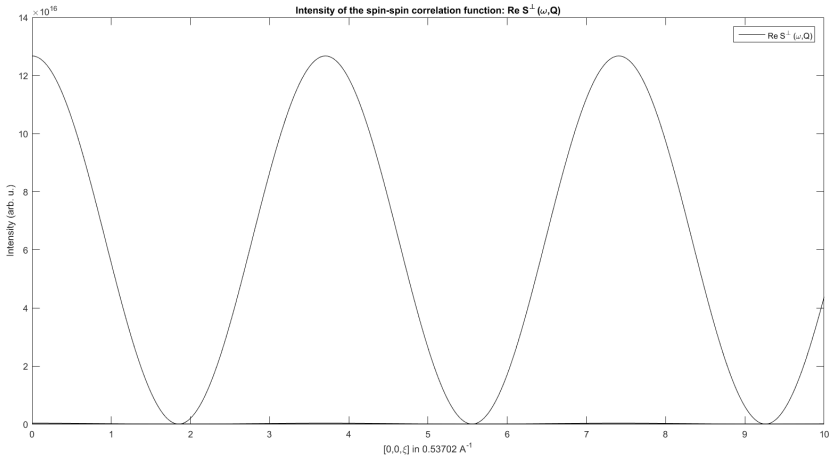

(a) *NBCO intensity simulation from* $\mathbf{k} = [0\,0\,0]$ *to* $\mathbf{k} = [0\,0\,10]$.

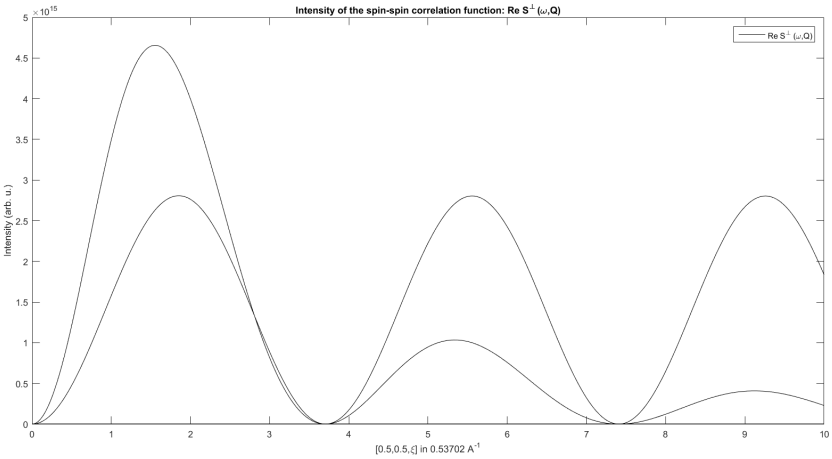

(b) *NBCO intensity simulation from* $\mathbf{k} = [0.5\,0.5\,0]$ *to* $\mathbf{k} = [0.5\,0.5\,10]$.

Figure 4.9: *NBCO spin-waves intensity dependence on the L direction.*

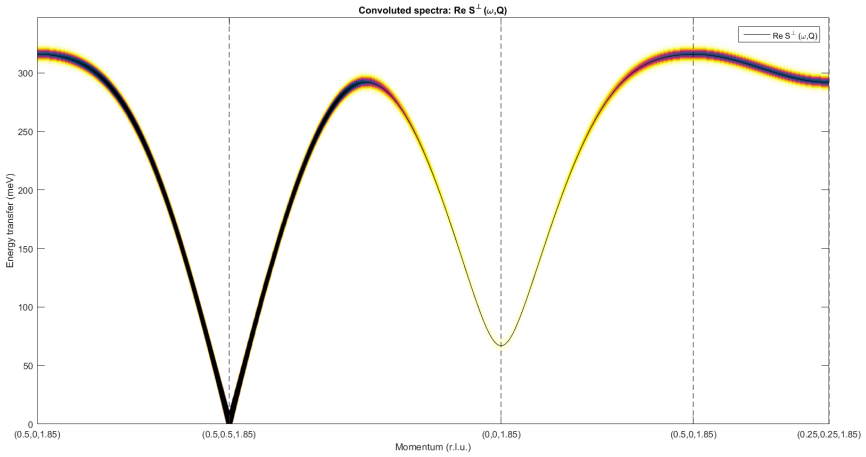

Figure 4.10: *NBCO optical mode dispersion function, obtained by imposing* $k_z = 1.85$ *r.l.u.*

r.l.u.; we thus obtain fig. 4.10.

4.4 Fitting

In this section, we will get to the heart of this work: the construction of the spin-wave dispersion fitting program based the SpinW toolbox. A possible initial fitting could be developed from the analytical solutions to the Heisenberg eigenvalues problem that have been proposed in various articles of the literature. In particular, in this work we used this approach on the model proposed by Coldea in [16], which neglects the out-of-plane dispersion dependence ($J_\perp = 0$) and makes use of the simple $t - J$ model. However, the results are not satisfactory, since the fitting error has a quite large value; it would be possible to improve this approach by using the results in [21], but its analytical development stands outside the scope of this thesis.

It is in this picture that SpinW becomes useful: it can be exploited as Matlab function on which found the fitting process. However, SpinW requires to limit the number of magnetic interactions between the atoms, which corresponds to the number of parameters of the fitting. In analogy with the explicit Coldea model, the two effective parameters of the simple $t - J$ model J and J' can be used. Yet this brings a still large error and does not permit to reproduce particular areas of

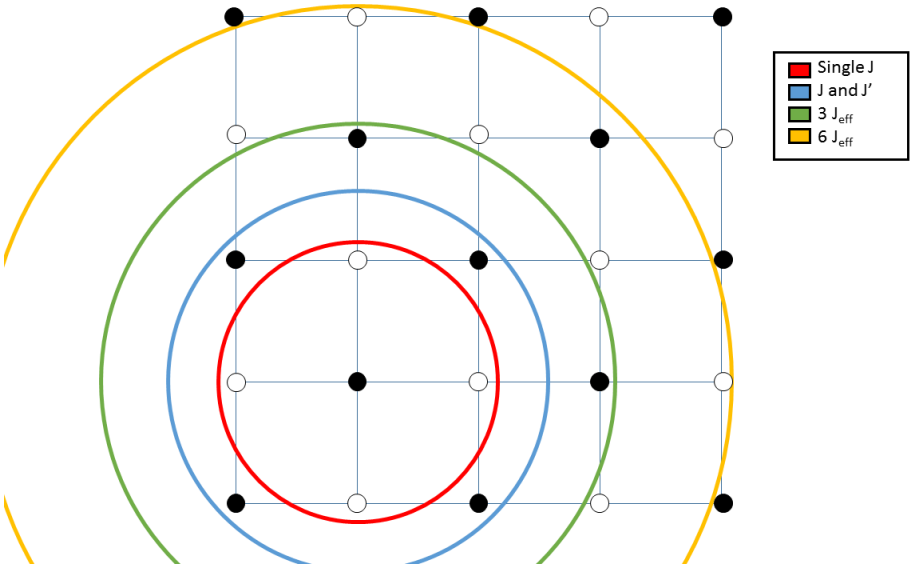

Figure 4.11: *Lattice area of the magnetic interactions taken into account by all the different fitting processes described in this work.*

the reciprocal space and certain complex trends of the dispersion. It is anyway quite straightforward to expand this approach to higher-order effective exchanges. In particular, in this work we take into consideration a third-order model, which however turns out to give similar results to the simple $t - J$ ones, and a six-order one. Higher orders give serious problems of convergence (faced in the appendix D). The different models just exposed are summarized in fig. 4.11. In the current section, all the solutions obtained with these different approaches are gathered and exposed.

4.4.1 Simple $t - J$, $3J$ and $6J$ fitting

To perform the fitting, we exploited Matlab function `lsqcurvefit`. This algorithm is a nonlinear least-squares iterative solver that finds coefficients x that solve the following problem:

$$\min_x \|F(x, xdata) - ydata\|^2 = \min_x \sum_i (F(x, xdata_i) - ydata_i)^2 \tag{4.15}$$

where $xdata$ and $ydata$ are matrices or vectors ($xdata$ contains the input data and $ydata$ is observed output) and $F(x, xdata)$ is a matrix-valued or vector-valued

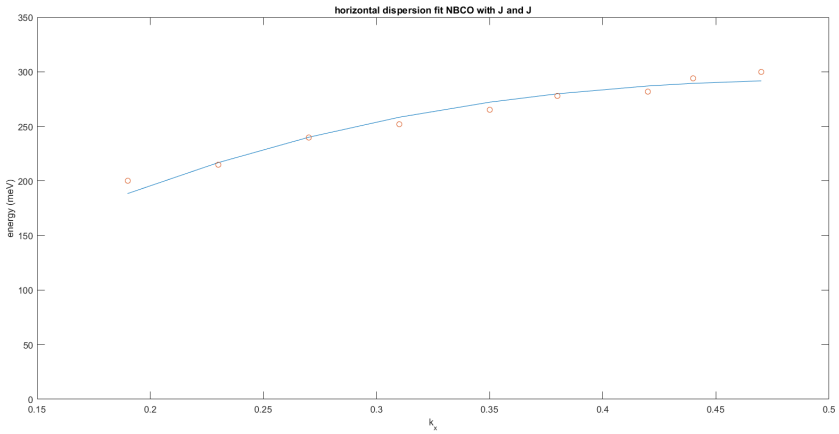

Figure 4.12: *NBCO fitting from* Γ *to* X*; the circles represent the collected data, the line is the fitting result.*

function of the same size as $ydata$. In particular, $F(x, xdata)$ must be defined by the user and simply correspond to a numerical ansatz to the problem. Furthermore, `lsqcurvefit` requires an x_{guess} initial guess for the parameters to find. It is useful to note that `lsqcurvefit` provides an useful optional exit output called `resnorm`, that is the norm of the residual; `resnorm` represents a criterion on which is possible to judge the effectiveness of the fitting. As a matter of fact, `resnorm` is defined as $\sum_i (F(x, xdata_i) - ydata_i)^2$, that depends on the dimension of the $ydata$ vector; it appears to be more useful to introduce a more generic parameter, therefore we defined the variable `error` as $\sqrt{resnorm}/N$, where N is the number of the data gathered.

First of all, we chose a simpler approach and we applied it only to NBCO; we didn't made use of SpinW, but we tried to fit the data with the simple $t - J$ model adopted by Coldea in [16] and already discussed in section 4.2. To do that, we programmed a Matlab function that would calculate $\omega_{\mathbf{k}} = 2Z_c(\mathbf{k})\sqrt{A_{\mathbf{k}}^2 - B_{\mathbf{k}}^2}$ (where, we remind, $A_{\mathbf{k}}$ and $B_{\mathbf{k}}$ are functions of the r.l.u. coordinate in the bidimensional Brillouin zone and are parametric on the in-plane exchange constants J, J', J'' and J_c, see equation (4.11)). We then exploited (4.12) to reduce the dependence on only two parameters, J and J', while we neglected the dependence on $J_\perp$. In this scenario, x is a vector containing J and J', $xdata$ are the $k_{x,y}$ coordinates in the reciprocal

lattice and *ydata* are the RIXS measurements results, whereas $F(x, xdata_i)$ is $\omega_{\mathbf{k}}$. Finally, it is possible to reverse (4.12) to obtain t and U as functions of J and J':

$$\begin{cases} U = \frac{(J+6J')^2}{4J'} \\ t = \frac{(J+6J')^{3/2}}{4\sqrt{J'}} \end{cases} \tag{4.16}$$

We started by doing a fitting try-out only on the data in the k_x axis (i.e. $[\Gamma \to X]$ direction) and the result is shown in fig. 4.12. We used $J = 140$ meV and $J' = 8$ meV as starting values and we obtained:

parameters	*result* (meV)
J	129.7
J'	2.9
error	2

that is quite acceptable.

Then, we tried to fit all the data collected at the ESRF in July 2015, that were distributed on the k_x axis, on the magnetic Brillouin zone boundary and on the positive diagonal. Initially we thought it was possible to make a surface fitting in all the $k_{x,y}$; however, this has been proven to be not convenient, since the number of data was to little to obtain a proper solution. So, we did a linear fitting in a single variable, defining the function on the path followed by our data in the reciprocal lattice; we used a piecewise defined function, appropriately changing the parameters and the form of $\omega_{\mathbf{k}}$. We named the effective variable s; it actually represents the distance treaded on the path between a chosen starting point and the coordinate of the datum. The path used for this fitting is $[0.5\,0] \to [0\,0] \to [0.25\,0.25] \to [0.5\,0]$; the resulting parameters are shown in the next table.

parameters	*result* (meV)
J	131
J'	3.6
t	248
U	1600
U/t	6.5
J_1^{eff}	95
J_2^{eff}	-14.5
J_3^{eff}	3.6
error	4.9

Here the effective exchange parameters have been calculated with the relations previously furnished.

This is completely reasonable: J_1^{eff} has the same sign of J_3^{eff} and they are both antiferromagnetic, however $J_3^{eff} \ll J_1^{eff}$, so that the second order interaction tends to be ferromagnetic; J_2^{eff}, on the other hand, is negative, i.e. ferromagnetic, as in fact is the magnetic order of the diagonal interactions. The result is shown in fig. 4.13.

A second trial without SpinW could be derived by exploiting the already mentioned high-order hopping model, derived in the article [21] by Delannoy et al. However, $A_{\mathbf{k}}$ and $B_{\mathbf{k}}$ expressions derived in the article seem to be wrong (as noted by Guarise et al. in [30]), and their extraction is not approachable; this is also shown by the result of the fittings.

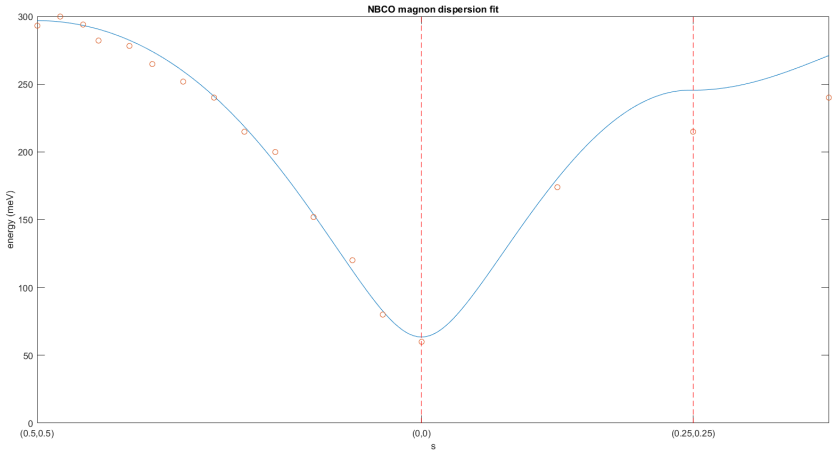

Figure 4.13: *NBCO fitting with explicit $\omega_{\mathbf{k}}$ expression of all the data gathered with ERIXS in July 2015. The path is reported in the text.*

We obtained:

parameters	*result* (meV)
J	135
J	4.3
t'	0.3
t''	32
error	3.1

whereas the theory requires that t' and t'' were < 1 and with opposite sign. Therefore, we discarded this option to extend our model.

Finally, it is possible to merge the fitting program with SpinW, i.e. to use a SpinW simulation script with free J and J' parameters as `lsqcurvefit` ansatz function. This also allows to add $J_\perp$ as a fitting parameter.

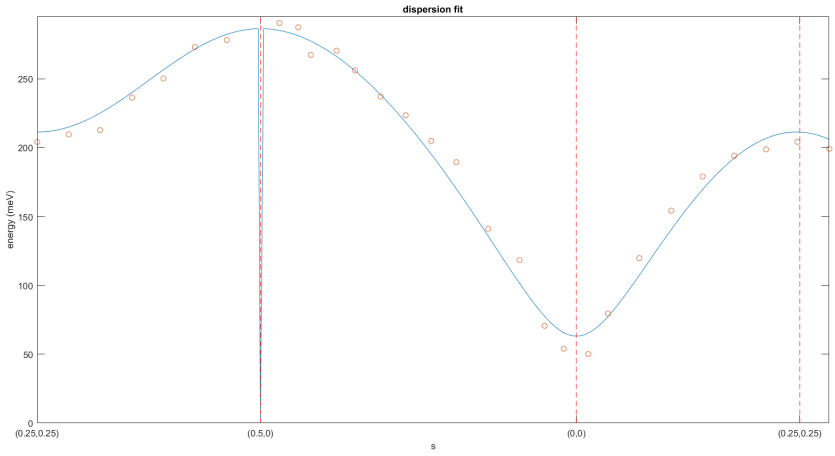

Figure 4.14: *NBCO fitting with t-J SpinW of all the data gathered with ERIXS. Simple t-J model was exploited.*

The result is shown in fig. 4.14 and the respective parameters are:

parameters	*result* (meV)
J	129.6
J'	5.3
$J_\perp$	9.3
t	230.5
U	1220
U/t	5.3
J_1^{eff}	76.6
J_2^{eff}	-21.2
J_3^{eff}	5.3
error	1.6

This fitting is not too good: 4.14 shows a good coherence with the data near the X point, but at Γ the energy gap is too high and the trend between the point is appears as smoothed.

The same method can be applied to both BiSCO and CCO data. Let us first

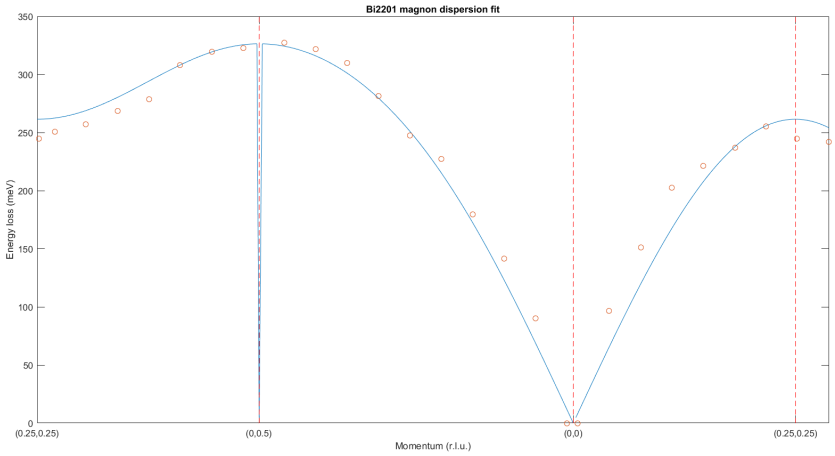

Figure 4.15: *Bi2201 fitting with SpinW and t-J model of the complete dataset gathered with ERIXS.*

take a look to the results for Bi2201; but before that, it is worth noticing that it has a fitting parameter less than the other two materials because its $J_\perp = 0$. The fitting result is reported in fig. 4.15 and the fitting parameters are:

parameters	*result* (meV)
J	147.5
J'	4.6
t	270.2
U	1670
U/t	6.2
J_1^{eff}	101.6
J_2^{eff}	-18.3
J_3^{eff}	4.6
error	2.9

It can be seen that also in BiSCO there are problems in Γ vicinity; the $t-J$ model shows also difficulties to reproduce the *plateau* around $[0.25\,0.25]$.

It is now possible to talk about CCO. We only have to add the note that, while

NBCO and Bi2201 dispersions are independent from the c axis reciprocal lattice coordinate k_z, the 3D magnetic structure of CCO requires to specify it; in the present case, $k_z = 0.44$ r.l.u., i.e. the one used during the measurements. As clearly visible in figure 4.16 (that depicts the $t - J$ fitting outcome for CCO), the problems in this compound are the same as for the two previous compounds: the reconstruction near Γ has a wrong trend and the *plateau* around [0.25 0.25] is rounded by the algorithm. In this case the parameters are:

parameters	*result* (meV)
J	182.2
J'	10.3
$J_\perp$	11.5
t	297.1
U	1440
U/t	4.9
J_1^{eff}	79.5
J_2^{eff}	−41.1
J_3^{eff}	10.3
error	3.3

By analyzing the data, it is possible to find that the dispersion along the [0.25 0.25] → [0.5 0] line, to which we address as ΔE_{MBZB} ($MBZB$ stands for "magnetic Brillouin zone boundary"), in CCO is almost double than in NBCO and BiSCO, and that this value is strictly correlated to the J_c parameter. On the other hand, the maximum E_{max} of magnon energy at X Brillouin point appears to be mainly set by the nearest neighbours exchange J.

Besides the wrong fitting trend, the results underline another problem already touched upon: the ratio U/t is too much smaller than that obtained from ARPES measurements [20] and the large-U hypothesis at the basis of the Hubbard model can't be fulfilled; this can be related to the presence of J_c, which is much higher

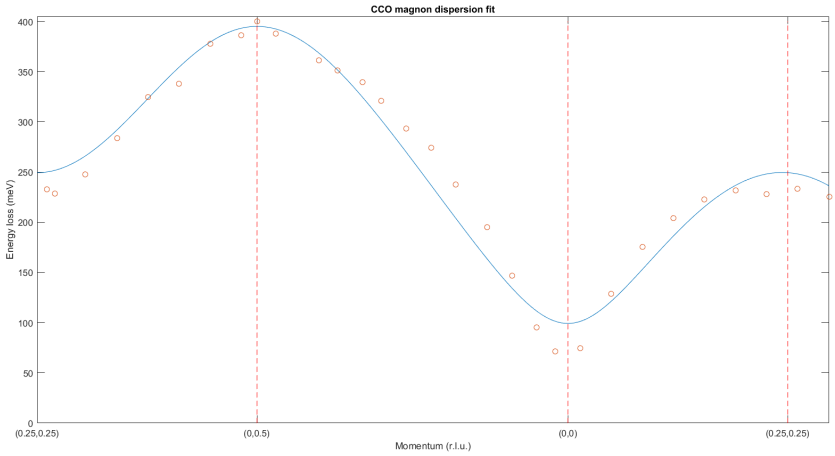

Figure 4.16: *CCO fitting with t-J SpinW algorithm.*

than J' and J'' (we recall that, in the simple $t-J$ model, $J' = J'' = J_c/20$), and that maintains U very low.

A possible extension of the $t-J$ model could be to disregard completely the analytical correlations (4.13) and (4.14) between the effective exchange parameters and the ones deduced theoretically (J, J', etc.). In this way, the fitting becomes on four parameters, the three J^{eff}s and $J_\perp$ (three for Bi2201, since it has no $J_\perp$ dependence), and the convergence could be less univocal, but this adds a freedom degree to the operation. Furthermore, this means that, since the relation between J^{eff}s and t and U is in this case unknown, it is no more possible to calculate the U/t ratio; however, this can provide a deeper understanding in the meaning of the various effective coefficients and, moreover, a better fitting result. We address to this model as *3J model*.

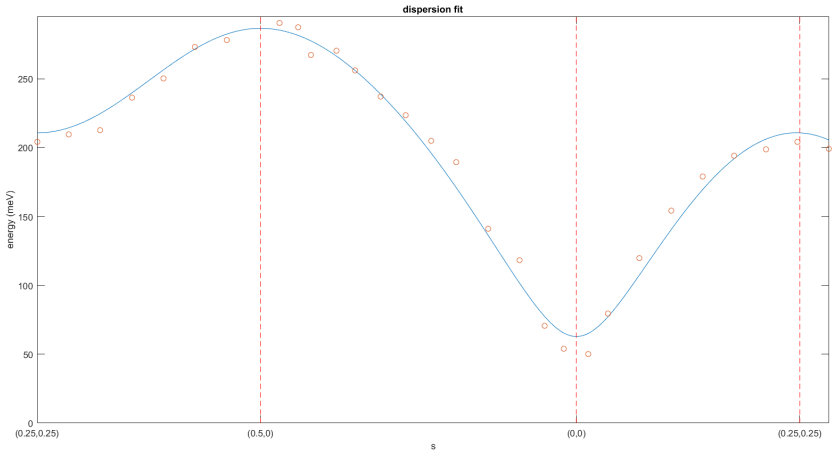

(a) *NBCO.*

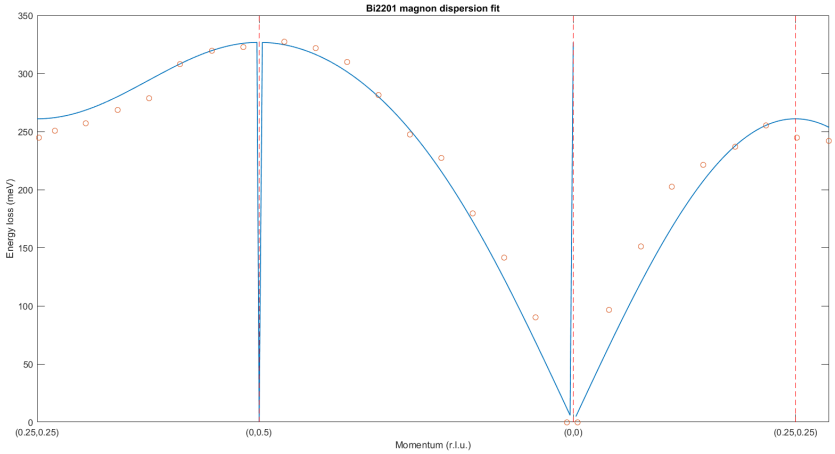

(b) *BiSCO.*

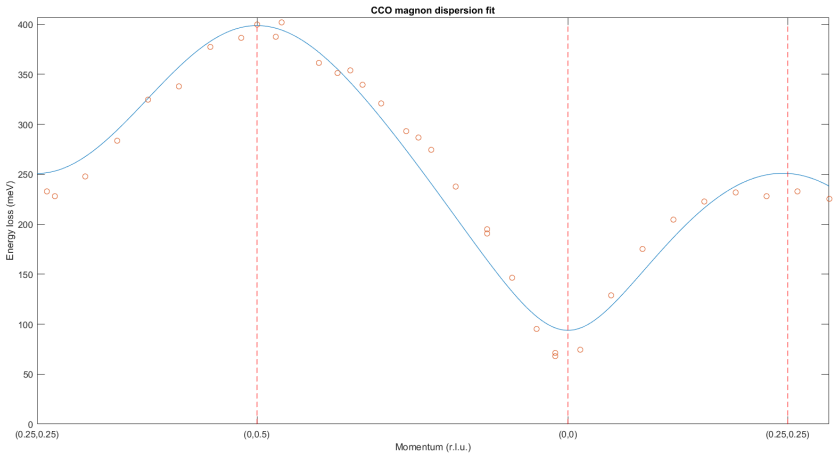

(c) *CCO.*

Figure 4.17: *NBCO, BiSCO and CCO fittings with SpinW, using the three $J^{eff}s$ as parameters, of all the data gathered.*

Therefore, we tried to apply this technique to NBCO, and the result is shown in figure 4.17a; the respective parameters are:

parameters	*result* (meV)
J_1^{eff}	90.3
J_2^{eff}	-14.6
J_3^{eff}	8.7
$J_\perp$	7.8
error	1.6

On the other hand, in BiSCO:

parameters	*result* (meV)
J_1^{eff}	111.4
J_2^{eff}	-13.5
J_3^{eff}	7.2
error	3.1

Finally, in CCO:

parameters	*result* (meV)
J_1^{eff}	112.1
J_2^{eff}	-26.6
J_3^{eff}	18
$J_\perp$	7.3
error	3.1

It is clear that, even if the bonds between the J^{eff}s have been relaxed, the error doesn't change very much, so there must be something else to influence the

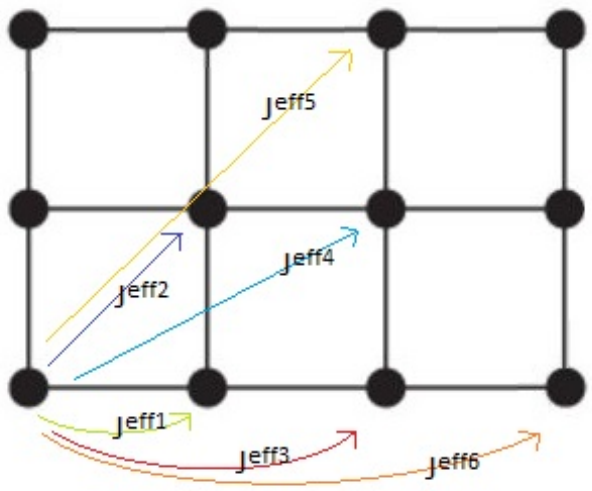

Figure 4.18: *Simple representation of the fourth, fifth and sixth order effective superexchanges.*

magnon dispersion to obtain the measured trend. To understand the meaning of these outcomes and to find some improvement to the present model, it seems to be mandatory to gain a deeper knowledge of the action of every J^{eff}s. This study has been performed and reported in the appendix C. Its results show that it is possible to improve the fitting performances by adding some effective exchanges, but the fourth- and the fifth-order parameters do not have enough influence on the dispersion: it is necessary to adopt at least a *6J model* (all the J^{eff}s are shown in fig. 4.18).

In the light of this hypothesis, we tried to fit the data with six J^{eff}s. The resulting plots are displayed in fig. 4.19 and all of them look quite good: the lines follow the measured trends pretty well, and in BiSCO and CCO the model proves to be able to reproduce also the *plateau* in [0.25 0.25]. Furthermore, as seen in the next table, the low value of the `errors` demonstrate the improvement obtained: 0.78 for NBCO, 1.32 for BiSCO and 0.86 for CCO.

However, the exchange parameters are completely different from both the ones previously obtained and the values we supposed they would assume:

parameters	*compound*		
	$NBCO$ (meV)	$Bi2201$ (meV)	CCO (meV)
J_1^{eff}	206.7	231.1	192
J_2^{eff}	56.4	58.8	25.8
J_3^{eff}	46.3	47	47.7
J_4^{eff}	11.8	9.6	11.7
J_5^{eff}	1.1	0.6	-2.3
J_6^{eff}	4.4	7.5	2.2
$J_\perp^{eff}$	1.7	/	1.8
error	0.78	1.32	0.86

These results are in complete opposition with the theory exposed until now, since their values are very high and all the J_2^{eff}s are widely positive. Therefore, the values obtained seem to be quite unphysical; however, there is no literature in this scope, and moreover, as we seen, the usual approach to cuprate system, that is the $t-J$ model, doesn't furnish acceptable results. It is possible to obtain values more similar to the ones expected if some restraints are put on the J^{eff}s values (for example J_2^{eff}) with an insignificant increase of the `error` (less than 1%). However, these solutions seem artificial, and most of the times they collapse on the boundaries chosen. This is due to the fact that a 6 or 7 parameters fitting has big convergence problems: there seem to be a gigantic number of convergence points, and the one towards which the procedure tends depends on the set of starting parameters inserted. To better understand this problem, we did run some convergence trials, whose results have been summarized in appendix D. It is although necessary to find an opportune condition to limit the number of numerical solutions to the problem.

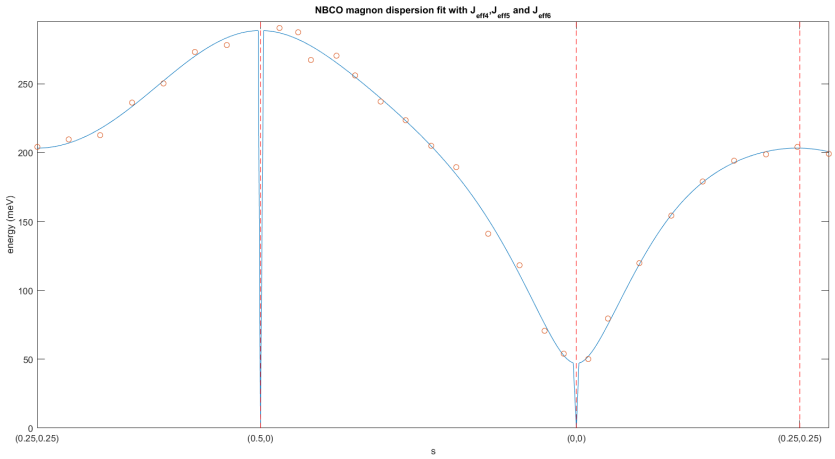

(a) *NBCO.*

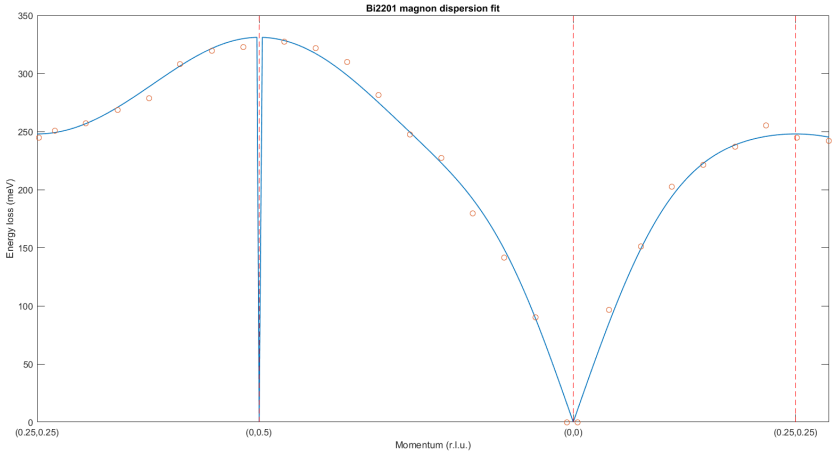

(b) *BiSCO.*

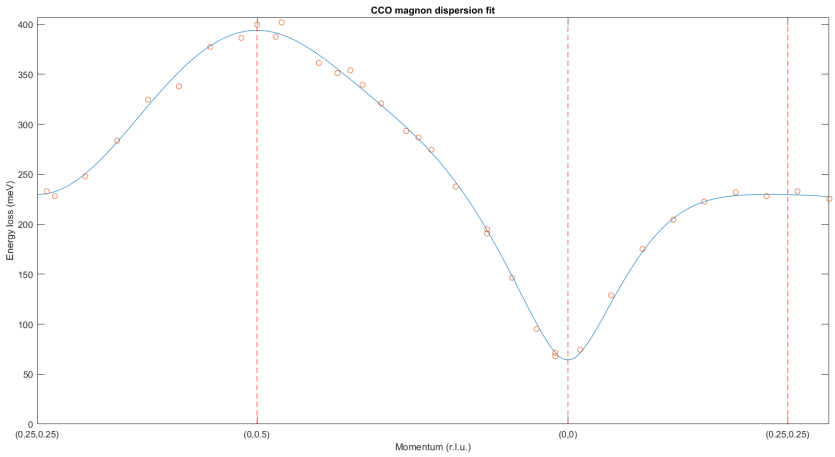

(c) *CCO.*

Figure 4.19: *NBCO, BiSCO and CCO fittings with SpinW, using the six $J^{eff}s$ as parameters, of all the data gathered.*

It is worth noticing that the methods ($t-J$, $3J$ and $6J$) have been tested also on other cuprate compounds, whose data have been obtained from the literature. In particular, the test materials were $Bi_2Sr_2YCu_2O_8$ (BSYCO), $Sr_2CuO_2Cl_2$ (SCOC) and La_2CuO_4 (LCO), whose experimental informations have been gathered in [19], in [56] and in [16] respectively. The first one, BSYCO, has a bilayered structure, very similar to the NBCO and YBCO ones, while the other two, SCOC and LCO, are monolayered and they can be compared to Bi2201; all three these compounds have been already studied deeply. Therefore, we exploited them to make sure that our model was correct; in particular, we applied the $t-J$ model method on BSYCO and SCOC and we checked that the resulting J and J' corresponded with the literature ones, thing that actually happened. However, since LCO features are well known, we continued to apply to it the various methods conceived to have a further prove of the dependence of the dispersion relation on the various J^{eff}s (both with the $3J$ and the $6J$ models), and, because of its similarity with BiSCO, to assure that the numbers obtained with its fittings were coherent. The two compounds results are actually similar; in particular, as all the other cuprates under study, LCO too shows a whole positive set of J^{eff}s.

4.5 Fitting results

Since putting boundaries to the fitting data has proven to be not satisfactory, another acceptable condition to reduce the convergence freedom of the results must be applied. As discussed, the $t-J$ model outcoming parameters were consistent with the theoretical suppositions despite the simple approach of the method. Therefore, we decided to perform a fit with the $6J$ model, but imposing J_1^{eff} values as the ones obtained with $t-J$. To maintain a reference with the literature results, the outcome of the application of this process to LCO are also reported afterwards. The results are gathered in the next table:

parameters	*compound*			
	$NBCO$ (meV)	$Bi2201$ (meV)	CCO (meV)	LCO (meV)
J_1^{eff}	76.64	101.65	79.48	119.95
J_2^{eff}	−14.30	−12.42	−29.34	−3.06
J_3^{eff}	11.04	11.41	20.27	8.41
J_4^{eff}	7.51	2.42	15.11	5.81
J_5^{eff}	0.59	−0.23	−3.94	0.68
J_6^{eff}	0.82	8.54	−3.72	−0.26
$J_\perp^{eff}$	4.37	/	3.68	/
error	0.79	1.34	0.90	0.81

It is clear that these results seem satisfactory; also, we checked with a few trials that the convergence would not be a problem, and it has been confirmed. Furthermore, remembering that the `errors` in $6J$ tests were 0.78 for NBCO, 1.32 for BiSCO and 0.86 for CCO, it is clear that the results of the exploited approach are essentially equivalent to the rough $6J$ model. In particular, the fitting pictures are shown in figg. 4.20, 4.21, 4.22 and 4.23.

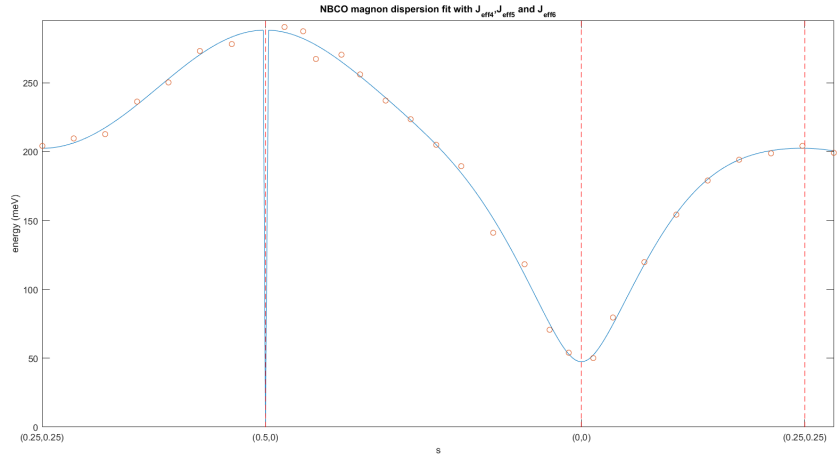

(a)

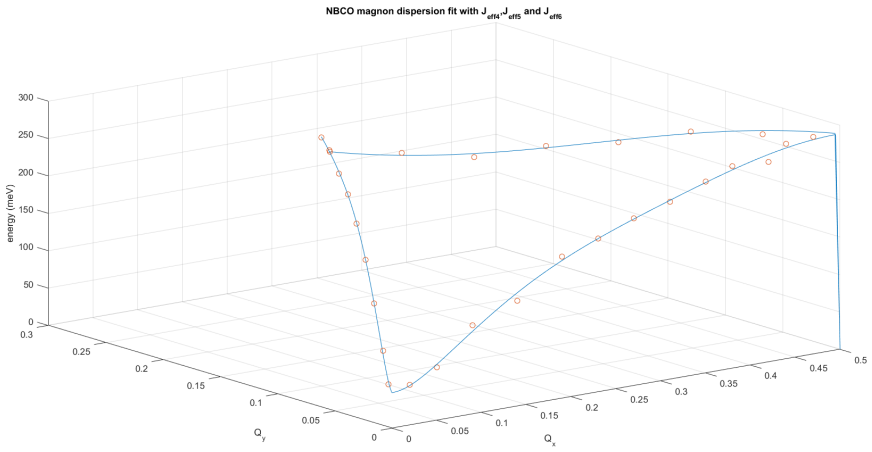

(b)

Figure 4.20: *NBCO final fitting. The figure above shows the usual dispersion on the s path, the one below shows the same result reported on its bidimensional path on the reciprocal lattice.*

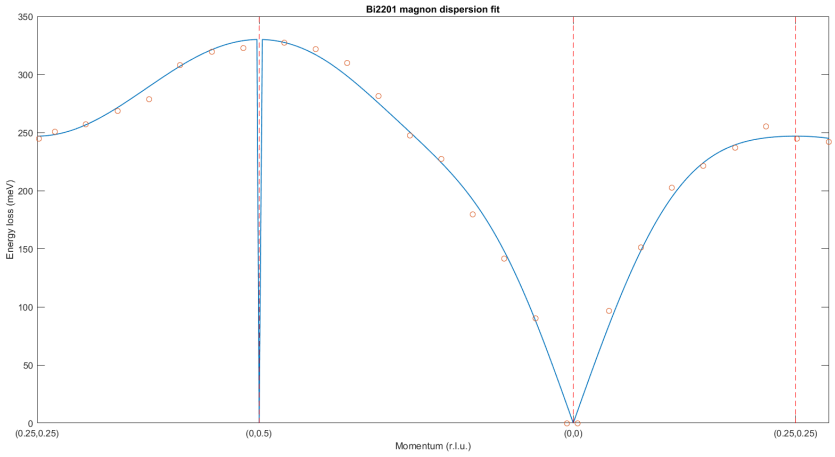

(a)

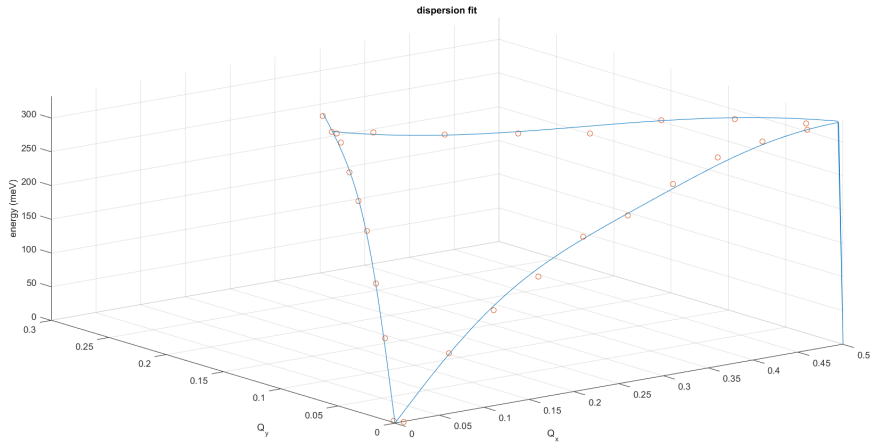

(b)

Figure 4.21: *BiSCO final fitting. The figure above shows the usual dispersion on the s path, the one below shows the same result reported on its bidimensional path on the reciprocal lattice.*

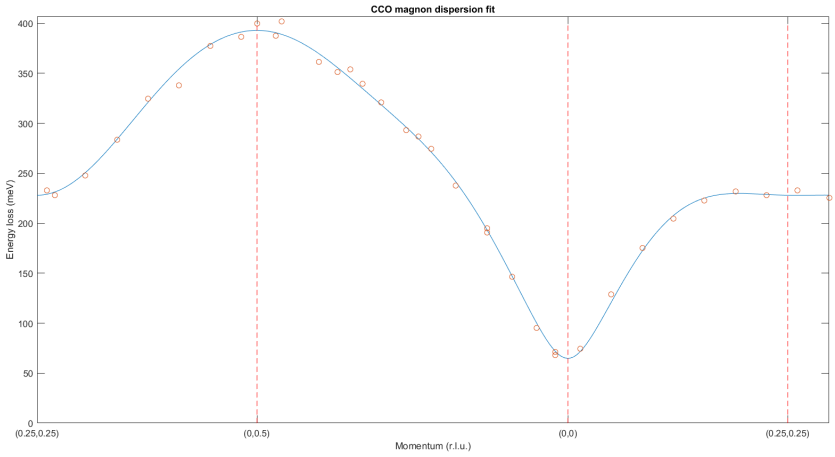

(a)

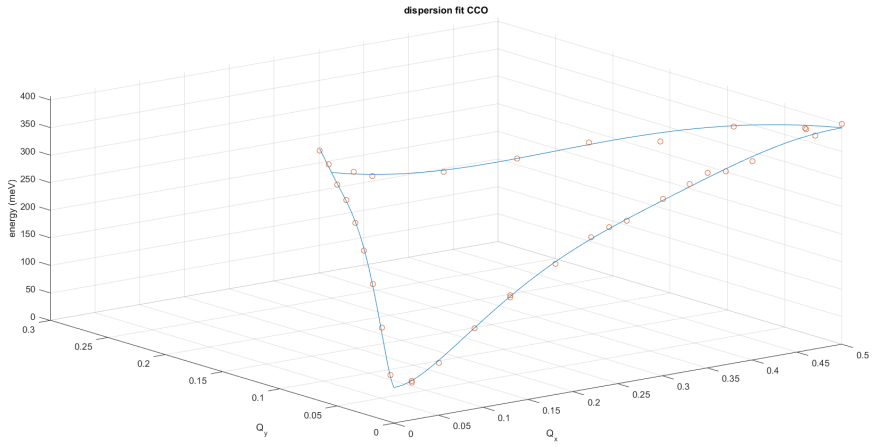

(b)

Figure 4.22: *CCO final fitting. The figure above shows the usual dispersion on the s path, the one below shows the same result reported on its bidimensional path on the reciprocal lattice.*

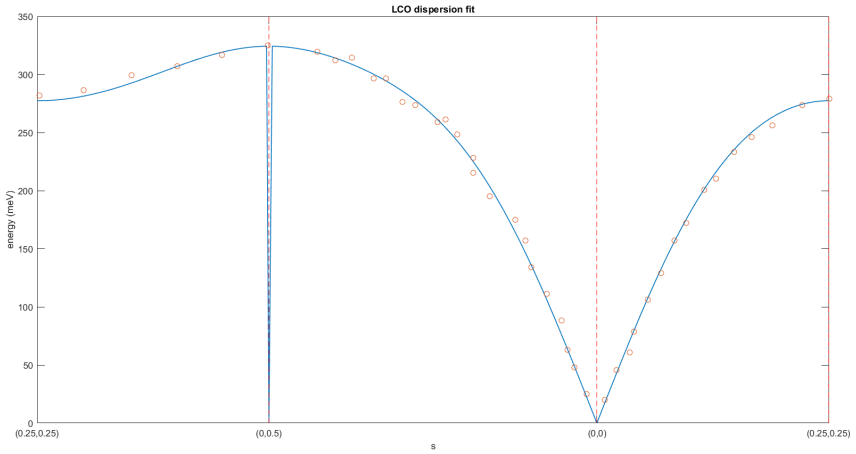

(a)

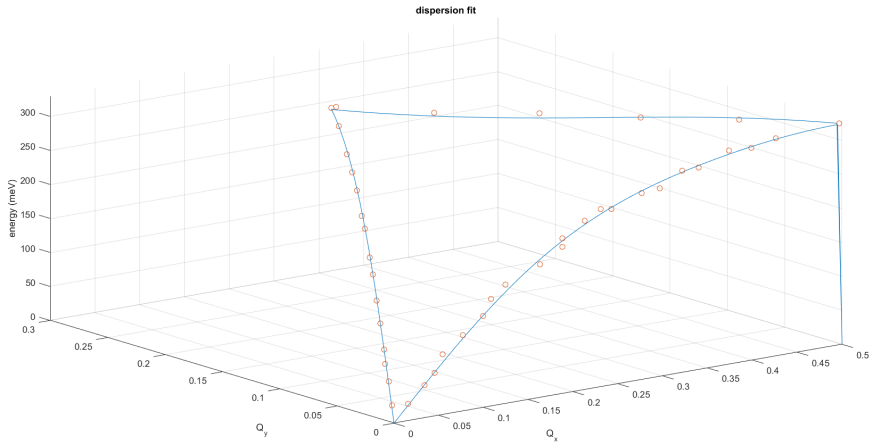

(b)

Figure 4.23: *LCO final fitting. The figure above shows the usual dispersion on the s path, the one below shows the same result reported on its bidimensional path on the reciprocal lattice.*

Let us try to interpret these numbers: as supposed, J_1^{eff} is positive and has the greatest absolute value in all the compounds, J_2^{eff} is negative and J_3^{eff} is small and positive; the higher-order parameters are difficult to understand, although J_4^{eff} is positive and J_5^{eff} has a very low modulus. Interestingly, in BiSCO J_1^{eff} and J_6^{eff} values are quite big; this can be linked to the strongly bidimensional structure of this material, feature that tends to enhance the intralayer interaction, whose strongest terms are the linear ones. On the other hand, in CCO J_3^{eff} is extremely high, and this could be related to the fact that in this case J_6^{eff} is negative, thing that has to be counterbalanced somehow; however, being J_1^{eff} fixed, the only linear term that could act on this matter is J_3^{eff}. In LCO, the fitting remains mainly dominated by J_1^{eff} and J_3^{eff}, with a particularly strong contribute from J_4^{eff}. All these results are shown in figg. 4.24a and 4.24b. Note that the higher BiSCO `error` it is mainly due to the presence of an extremely high point near [0.25 0.25].

Finally, a deeper study showed that the sum $J_1^{eff}+|J_2^{eff}|+2J_4^{eff}+J_6^{eff}$ is linearly related to the magnon energy E_{max} at X, as is J in the Hubbard model (fig. 4.24c), while $|J_2^{eff}| + J_3^{eff}$ is proportional to ΔE_{MBZB} (fig. 4.24d), in analogy to J_c.

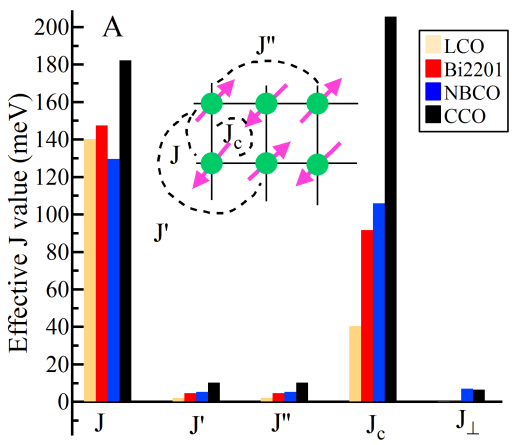

(a) *Histogram of the simple $t-J$ model results.*

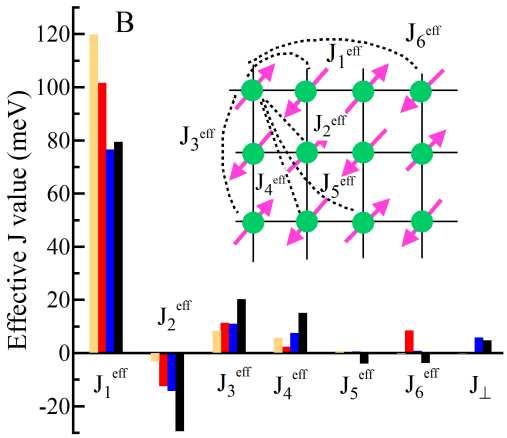

(b) *Histogram of the 6J model results.*

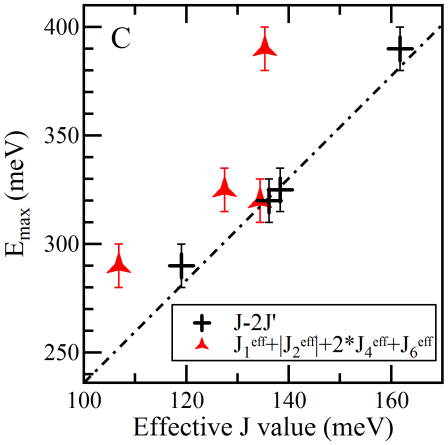

(c) *Dependence of E_{max} on $J^{eff}s$.*

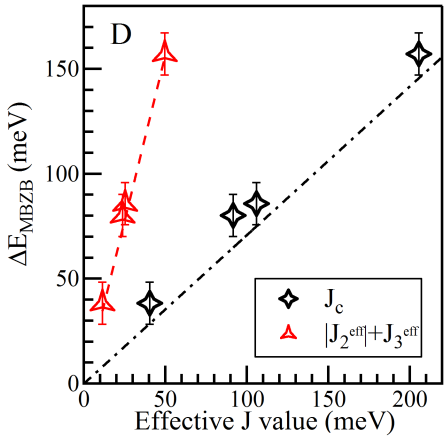

(d) *Dependence of E_{MBZB} on $J^{eff}s$.*

Figure 4.24: *LCO final fitting. The figure above shows the usual dispersion on the s path, the one below shows the same result reported on its bidimensional path on the reciprocal lattice.*

Conclusions

In this work we proposed various possible fitting methods to analyze spin-wave magnetic dispersion relation in parental compounds of superconducting layered cuprates, and we eventually pointed out, in our opinion, the best among the others, feasible with the instruments within grasp. However, only the $3d_{x^2-y^2}$ copper and the $2p_{x,y}$ orbitals have been taken into account. On the contrary, it has been suggested (by Pavarini et al. [54]) that other molecular orbitals could partake into the complex magnetic interaction picture here exposed. In particular, a possible central role could be played by the so-called *apical oxygens*, i.e. the out-of-plane oxygens bounded to the in-plane copper ions. In each of three compounds under study the number of apical oxygens per copper site it is different: Bi2201 has two of them, disposed symmetrically in respect with the CuO_2 plane, which determine an elongated octahedron structure (fig. 2.11b); on the other hand, NBCO, being organized in bilayers, shows only a single apical O per in-plane Cu (fig. 2.11a), while in CCO they are completely absent, feature that permits the material to generate the already discussed tree-dimensional lattice structure, composed by an incommensurate series of CuO_2 planes (fig. 2.11c).

According to this theory, the presence of the apicals polarizes the out-of-plane states (i.e. the Cu $3d_{z^2}$ orbital), thus quenching the magnetic ordering in the planes. On the contrary, the absence of apical oxygen supports, aided by the long range $4s$ copper orbital, the delocalization of the valence electrons on the lattice, therefore expanding the interaction area of the hopping integrals.

In this scope, the results obtained in the last chapter permit to show how the number of apical oxygen per Cu atom can strongly affect the behaviour of a com-

pound. In fact, it can be noted that a couple of apical oxygens close to the layer copper (as in LCO, where $z_{Cu-O} = 2.4$ Å) determines relatively small values of the difference of energy ΔE_{MBZB} between the two points X and [0.25 0.25], both located on the magnetic Brillouin zone boundary; furthermore, it has already been described how this difference is related to J_c and to $|J_2^{eff}| + J_3^{eff}$, which also appear to be weak. On the other hand, in BiSCO and NBCO, where there are two apicals at larger distance ($z_{Cu-O} = 2.58$ Å) and one apical nearby ($z_{Cu-O} = 2.38$ Å) respectively, both ΔE_{MBZB}, J_c and to $|J_2^{eff}| + J_3^{eff}$ are larger. Finally, in CCO, where there are no apical oxygens, all of these parameters are significantly big. It is nonetheless clear that apicals can't furnish an universal instrument to decipher all the cuprates peculiar characteristics: in fact some other parameters, like the maximum energy of the dispersion E_{max} and the next-neighbour exchange J, do not seem to be related to the number and distance of apical oxygens. However, the link between E_{max} and the aspects of the superconductive phase, in particular the critical temperature T_c, has not been demonstrated: actually, different studies have led to opposite conclusions [46] [51] [24].

In the light of this, we wanted to understand if there effectively is an influence of the apicals configuration to the superconducting behaviour in cuprates. Let us bring together all the pieces: we found that there is a relation of inverse proportionality between the number and distance of apical oxygens and both ΔE_{MBZB}, J_c and to $|J_2^{eff}| + J_3^{eff}$ parameters; this is due to the fact that the apicals presence tends to localize charge in the $3d_{z^2}$ orbitals thus producing an effective screening by the polarizable charge reservoir layer. On the other hand, in [54] Pavarini et al. pointed out that the optimum doping superconductive critical temperature $T_{c,max}$ scales with the next-nearest-neighbor hopping, which grows with the distance of apical oxygen from the CuO_2 plane. It has been therefore determined that there is a positive correlation between ΔE_{MBZB} and the maximum of Tc, as plotted in Fig. 4 E (bottom panel). That way, we can conclude that $T_{c,max}$, ΔE_{MBZB}, the long range hopping coupling parameters and the number and distance of apical oxygens are all related quantities, and that apicals depress $T_{c,max}$ by localizing the wave-

functions relevant to the hopping process; this finds an experimental confirmation in the usually high $T_{c,max}$ in tri-layer cuprates compounds.

Appendix A

CCO calculations

In this appendix the thoery in section 4.1 is directly applied to the CCO case. In CCO, all the planes are separated by the same distance, and because of that $J_{\perp 2} = J_{\perp 1} = J_{\perp}$. Therefore $\alpha_{\perp} = 2\alpha_{\perp 1} = 2J_{\perp}/J_{\parallel}$ and $\frac{\omega_{\parallel}\sqrt{\alpha}}{\sqrt{2}} = \frac{2\sqrt{J_{\parallel}J_{\perp}}}{\hbar}$; for the same reason, we can simplify $|\gamma_{\perp}| = \sqrt{\frac{1\cos q_z c}{2}}$. Finally, substituting the relations above in $\omega_{\mathbf{q}z}$, we can calculate:

$$\hbar\omega_{\mathbf{q}z} = 2\sqrt{J_{\parallel}J_{\perp}}\sqrt{1 \mp \sqrt{\frac{1+\cos q_z c}{2}}} = 2\sqrt{J_{\parallel}J_{\perp}}\sqrt{1 \mp \cos\frac{q_z c}{2}} \tag{A.1}$$

where $\ominus$ and $\oplus$ are simple labels to discern the two resulting modes, based on the $\mp$ sign in (4.7). We exploited the trigonometric property $\sqrt{1+\cos 2a} = \sqrt{2}\cos a$. We can therefore make explicit:

$$\begin{cases} \ominus & \hbar\omega(q_z) = 2\sqrt{2}\sqrt{J_{\parallel}J_{\perp}}\cos\frac{q_z c}{4} \\ \oplus & \hbar\omega(q_z) = 2\sqrt{2}\sqrt{J_{\parallel}J_{\perp}}\sin\frac{q_z c}{4} \end{cases} \tag{A.2}$$

From these results it is possible to calculate the modes q_z dependence in CCO; for example:

$$\begin{cases} \ominus & \hbar\omega(0,0,0) = 0 \qquad \hbar\omega(0,0,1/2) = 2\sqrt{J_{\parallel}J_{\perp}} \\ \oplus & \hbar\omega(0,0,0) = 2\sqrt{2}\sqrt{J_{\parallel}J_{\perp}} \qquad \hbar\omega(0,0,1/2) = 2\sqrt{J_{\parallel}J_{\perp}} \end{cases} \tag{A.3}$$

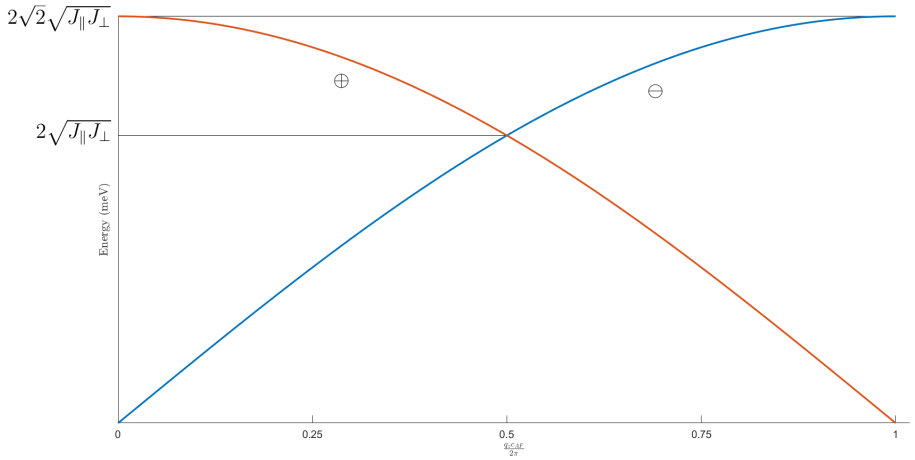

Figure A.1: *CCO magnon dispersion along L (i.e. c axis), obtained with* (A.2).

We can thus explicitly plot the magnon dispersion relation of CCO in Γ as a function of q_z and find the figures A.1. Note that we used the c_{AF} coordinate instead of the lattice coordinate c_N; this is due to the fact that, as already mentioned, the magnetic lattice has a unit cell with doubled generation vectors, and in CCO in particular, where the out-of-plane coupling is antiferromagnetic too, also the c coordinate must be extended.

Appendix B

SpinW

The aim of this appendix is to give a brief review to the tools made available by the SpinW library. This program can be downloaded for free on the PSI official site [53], along with a rich documentation. Its heart corresponds to the definition of the `sw` (spin-wave) class, which is a handle subclass that contains all the informations on the system characteristics. In particular, a `sw` object is composed by the various sub-elements required to define a spin crystal lattice.

For example, let us retrace the process necessary to simulate a magnon dispersion relation, i.e. the one used in this work. First of all, the simulation script must define a `sw` object, e.g. `obj = sw`. Then, it is possible to fill the various fields of `obj`, thus defining the problem. `obj.genlattice(...)` defines the crystal structure of the system, i.e. contains the lattice unit cell parameters (both x, y and z basis vectors' length, expressed in Å, and the angles between them) and the symmetry of the system. After that, the command `obj.addatom` permits to declare the atoms of which the unit cell is composed (it requires the relative position of the atom in the cell and its total spin). The magnetic interactions between the lattice elements can be defined after the command `obj.gencoupling`, which takes the maximum interaction distance as input. However, the single couplings must be added one by one to the possible operators in the system with the `obj.addcoupling` tool. In case of exchange interactions, the explicit form of the coupling corresponds to a scalar value: the effective ith-order exchange parameters J_i^{eff}, which must be defined one

by one. However, some different typologies of interactions can be described also by other algebraic elements (e.g. an anisotropy is characterized by the 3×3 matrix D). Finally, the command `obj.genmagstr` specifies all the spin vectors directions, according to its inputs: the `mode` with which the structure is generated (we used the `helical` one), the number of times the magnetic lattice cell is larger than the unit cell `nExt`, the central atom spin vector `S`, on which to build the structure, the vector normal to the spin plane `n` and the magnetic ordering wavevector `k`, expressed in r.l.u. (reciprocal lattice units).

Lastly, to obtain the dispersion relation, the path in the reciprocal lattice (and again in r.l.u.) on which it must be calculated has to be defined. The generic form of this input is `Qpath = {[a b c] ... [d e f] n(steps)}`, where `[a b c]` and `[d e f]` are respectively the initial and the final vectors of the path, but between them it is possible to define many sidesteps, while `n(steps)` is the number of the steps in which calculate the dispersion. At last, to obtain the dispersion plot one must generate the figure with the `sw_plotspec` tool. This script also permits to plot the intensity of the measured signal; however, this library has been conceived for INS experiments simulations, so the resulting intensity should be renormalized with RIXS and INS cross-sections.

Appendix C

J^{eff} dependence

This appendix is dedicated to a better understanding of the role that the various effective exchange parameters J^{eff}s play in the magnon dispersion relation fitting. To do that, we simulated Bi2201 dispersion relation by maintaining constant all the J^{eff} except one, on which was applied 6 small variations of 2 meV multiples around the values obtained from a $3J$ model fitting. We chose Bi2201 because, since it is monolayered, its magnon dispersion along the c axis is constant, i.e. $J_\perp = 0$ and can be excluded from the fitting. The results are shown in C.1.

We can see that both J_1^{eff} and J_2^{eff} modify the spin-wave energy around X point, but their contribution is opposite, i.e. increasing J_1^{eff} raises the energy, whereas an increment of J_2^{eff} lowers it; however, note that, if $J_2^{eff} < 0$, the increment of the modulus of both parameters enhances the value of the dispersion in X. Furthermore, it is important to note that J_2^{eff} acts on ΔE_{MBZB} (i.e. the difference between the function value in [0.25 0.25] and [0 0.5]), that is on the antiferromagnetic Brillouin zone boundary. On the other hand, J_3^{eff} doesn't modify the dispersion in X and Γ, while it changes the paths in between these two points; it also corrects heavily the magnon energy in [0.25 0.25]. Therefore, J_3^{eff} is an important tool for our goal, because we want to modify the fitting trend without virtually moving the local minima and maxima. Nonetheless, J_3^{eff} it's still not enough powerful to permit an optimal fitting because it doesn't have sufficient control on the $X \to \Gamma$ horizontal trait.

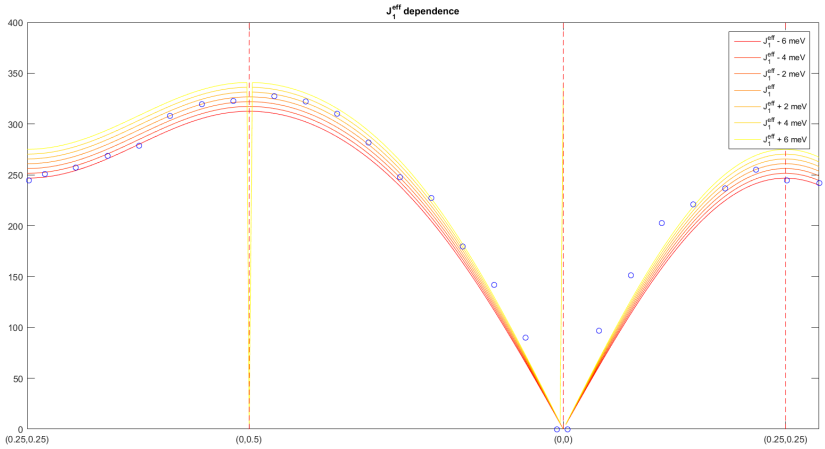

(a)

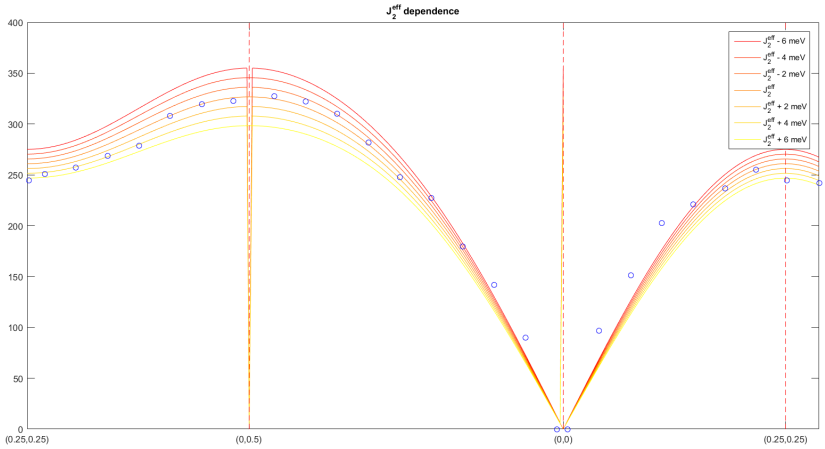

(b)

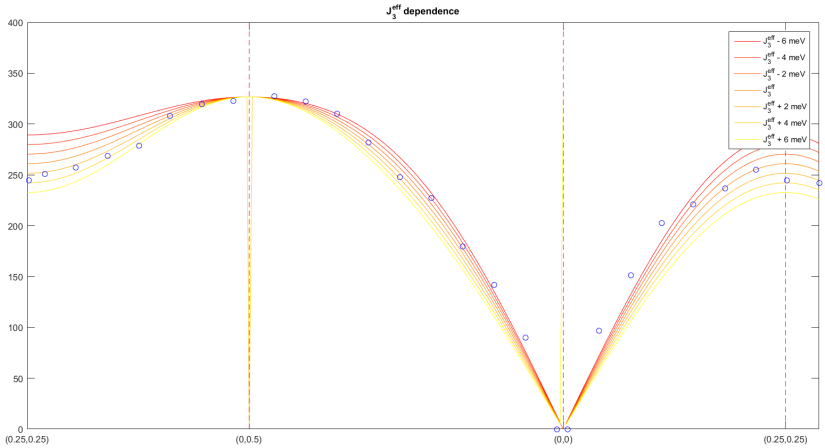

(c)

Figure C.1: *Study of the dependence of the magnons' dispersion relation on J_1^{eff} in C.1a, J_2^{eff} in C.1b and J_3^{eff} in C.1c.*

Since the simple $t-J$ model appears to be restrictive, the next model that has to be cosidered is a quartic expansion on the Hamiltonian in t/U; this generates an enormous number of interaction terms with complicated expressions, which is outside of the purpose of this thesis to show. However, it is possible to logically derivate that, since the quartic expansion added some terms that represent higher-order hopping events, the new Hamiltonian will necessarily add longer effective exchange interactions to our picture. If, as did with the $3J$ model, we don't aim to give an analytical relation between U/t and the effective parameters, we can try to perform a fitting with more effective parameters. However, the fittings with 4 J^{eff}s didn't seem to improve the results: although J_4^{eff} (viewable in 4.18) gives 8 contributions to the effective Hamiltonian, it is a low symmetry hopping and, as we are about to see, it can't adequately affect the critic areas of the dispersion on its own. It is therefore necessary to introduce a 5 J^{eff}s, but even this case is not satisfactory, and above all the J_5^{eff}, also shown in 4.18, introduces a coupling long $2\sqrt{2}a \sim 2.83a$ (where a is the square lattice side), whereas the next order exchange, J_6^{eff}, has a $3a$ length, that is quite near. It could be useful to add higher order terms; however, the fitting, even with six parameters, shows difficult convergence problems, as it is discussed in the next paragraph. Therefore, we eventually adopted a model with six J^{eff}s, referred to as *6J model*. This generates the effective couplings J_4^{eff}, J_5^{eff} and J_6^{eff} shown in 4.18.

So, we made a second dependence test: we fixed J_1^{eff}, J_2^{eff} and J_3^{eff} to their original value and we tried to add a small dependence (± 1.5 meV, ± 3 meV and ± 4.5 meV) on the next three orders effective interactions J_4^{eff}, J_5^{eff} and J_6^{eff} to see how the model reacts to them. The results of our test are in C.2. From these images we can see that J_4^{eff} works in a similar way as J_1^{eff}, but it enhances the function derivative around Γ point, therefore it can be useful to achieve a better fitting. J_5^{eff}, on the other hand, maintains fixed every local maximum and minimum, so it works similarly to J_3^{eff} and it could prove to be a very good parameter. Finally, J_6^{eff} is very odd: its effect is quite uniform and little, but it can be seen that it acts less on the [0 0.25] position, so this could be interesting too. If we would guess, we would

expect that J_6^{eff} gave a positive contribution, like J_1^{eff} and J_3^{eff}, because the three of them are all linear. On the other hand, we would suppose that J_5^{eff} would be negative, like J_2^{eff}, since it is the second diagonal interaction. More arduous to hypothesize is J_4^{eff} behaviour, but it can't be very strong, since it is not on an easy axis. Actually, none of the latter introduced parameters could be too high, since the main terms of the fitting remain J_1^{eff}, J_2^{eff} and J_3^{eff}.

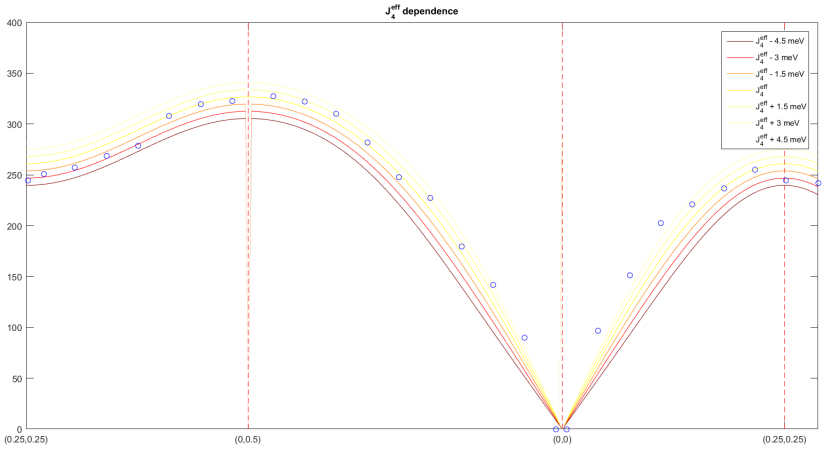

(a)

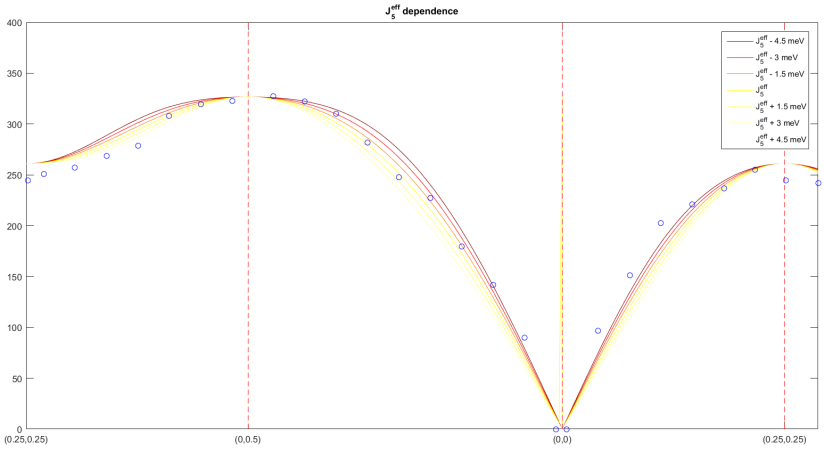

(b)

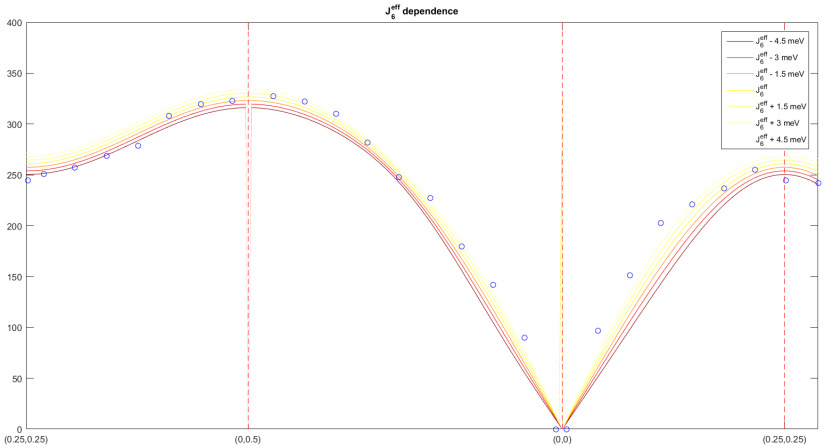

(c)

Figure C.2: *Study of the dependence of the magnons' dispersion relation on J_4^{eff} in C.2a, J_5^{eff} in C.2b and J_6^{eff} in C.2c.*

Appendix D

Convergence check

In subsection 4.4.1 of chapter 4 it has been determined that with the $6J$ model it is possible to obtain a good consistency with the measurements, but the outcoming parameters do not seem reliable. This problem could be better understand if it would be possible to map the `error` in the input J^{eff}s space, which would permit to recognize the convergence outline. However, in our cases this space has six dimensions in the best case, fact that gives problems in both the numerical calculations, that demand a tremendous amount time and computational power, and the results presentation. Therefore, we decided to simplify the calculation as much as it was possible: we programmed an algorithm that would calculate both the outcoming fitting exchanges and the corresponding `error` for all the possible combinations of two sets of J^{eff}s, one with relatively high and one with relatively low values. The results are depicted in figg. D.1, D.2 and D.3, and they are quite interesting: we can see that NBCO and Bi2201 results are quite similar, as both of them have, apart from the few divergence cases (which are characterized by an abnormally high `error`), substantially two strong converge situations, that attract the resulting parameters whatever the combination could be.

These two possible results are for BiSCO:

parameters	*low result* (meV)	*high result* (meV)
J_1^{eff}	78	268
J_2^{eff}	-32	65
J_3^{eff}	5	54
J_4^{eff}	3	10
J_5^{eff}	-0.5	0.1
J_6^{eff}	13	5

and for NBCO:

parameters	*low result*	*high result*
J_1^{eff}	85	244
J_2^{eff}	-19	67
J_3^{eff}	12	55
J_4^{eff}	9	14
J_5^{eff}	0.6	1
J_6^{eff}	0.7	5
$J_\perp^{eff}$	5	2

We see that the lower convergence point has physically acceptable numbers, and it is thus possible to accept it as best solution candidate. However, CCO shows an unique behaviour that does not uphold this choice: it has an only one convergence point, and furthermore, since there are no diverging combinations and all the imposed J^{eff}, however low, give the same result, it seems very strong.

parameters	*high result* (meV)
J_1^{eff}	225
J_2^{eff}	31
J_3^{eff}	56
J_4^{eff}	14
J_5^{eff}	-3
J_6^{eff}	4
$J_\perp^{eff}$	3

From a quick look to the resulting values, it appears that CCO misses the "right" mode. Therefore, even this analysis doesn't give us a firm result.

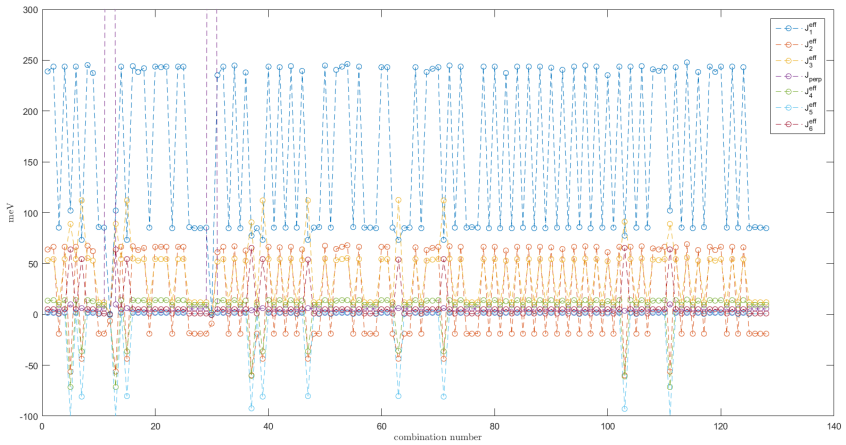

(a) *NBCO* $J^{eff}s$.

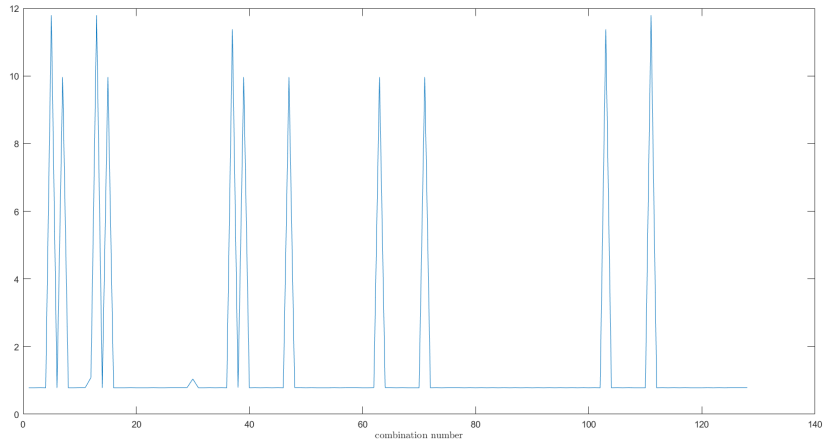

(b) *NBCO errors.*

Figure D.1: *NBCO convergence trial. The upper figure shows the outcoming parameters for each combination of inputs, while the lower the respective error.*

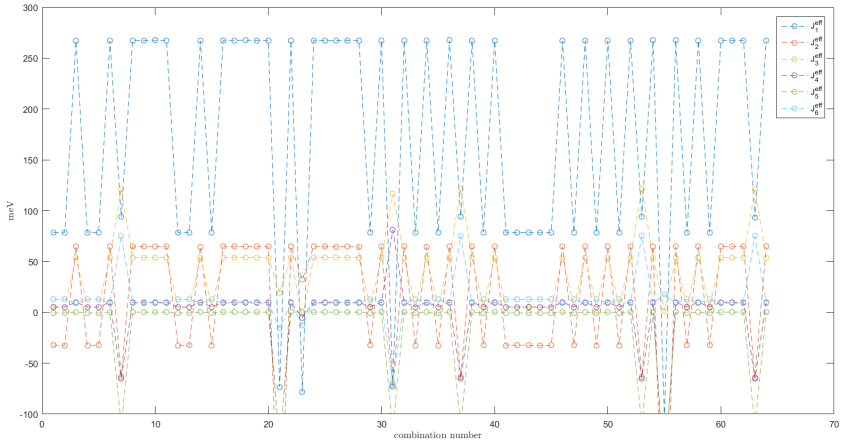

(a) *BiSCO* $J^{eff}s$.

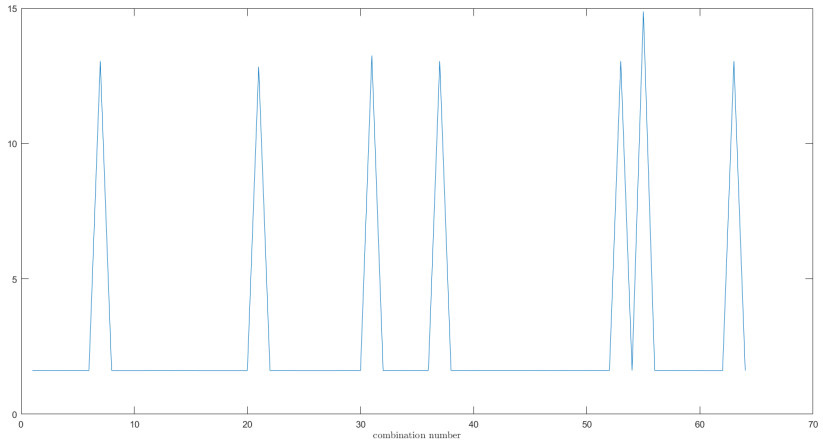

(b) *BiSCO errors.*

Figure D.2: *BiSCO convergence trial. The upper figure shows the outcoming parameters for each combination of inputs, while the lower the respective error.*

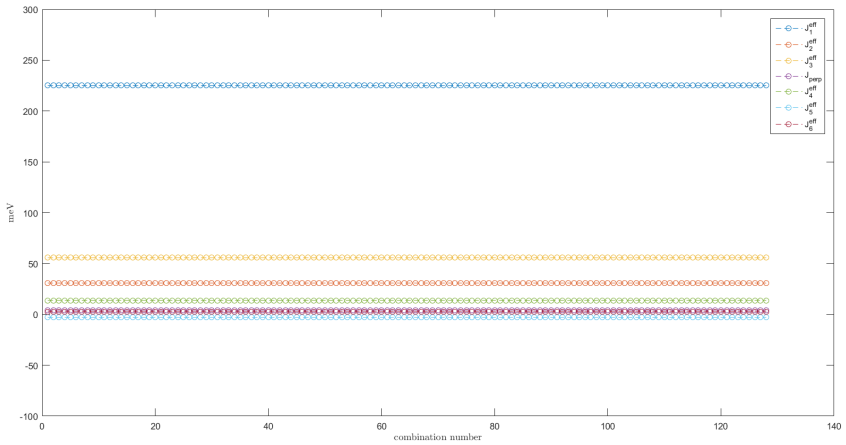

(a) *CCO* J^{eff} *s.*

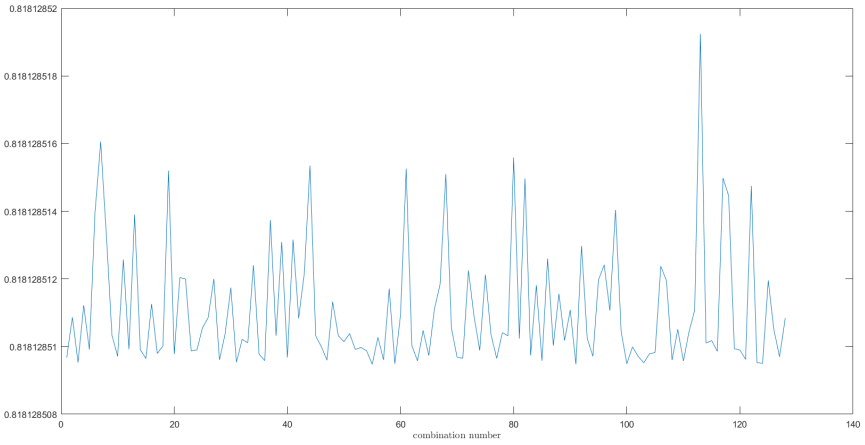

(b) *CCO errors.*

Figure D.3: *CCO convergence trial. The upper figure shows the outcoming parameters for each combination of inputs, while the lower the respective error.*

Bibliography

[1] Alexander Altland and Ben D Simons. *Condensed matter field theory*. Cambridge University Press, 2010.

[2] Luuk JP Ament et al. "Resonant inelastic x-ray scattering studies of elementary excitations". In: *Reviews of Modern Physics* 83.2 (2011), p. 705.

[3] Luuk JP Ament et al. "Theoretical demonstration of how the dispersion of magnetic excitations in cuprate compounds can be determined using resonant inelastic X-ray scattering". In: *Physical review letters* 103.11 (2009), p. 117003.

[4] Andrea Amorese. "Single photon acquisition in CCD detectors for high resolution". Master's thesis. Politecnico di Milano, 2013.

[5] Andrea Amorese et al. "Enhancing spatial resolution of soft x-ray CCD detectors by single-photon centroid determination". In: *arXiv preprint arXiv:1410.1587* (2014).

[6] PW Anderson. "Antiferromagnetism. Theory of superexchange interaction". In: *Physical Review* 79.2 (1950), p. 350.

[7] J George Bednorz and K Alex Müller. "Possible high T c superconductivity in the Ba—La—Cu—O system". In: *Ten Years of Superconductivity: 1980–1990*. Springer, 1986, pp. 267–271.

[8] Karl-Heinz Bennemann and John B Ketterson. *Superconductivity: Volume 1: Conventional and Unconventional Superconductors Volume 2: Novel Superconductors*. Springer Science & Business Media, 2008.

[9] S Blanco-Canosa et al. "Resonant x-ray scattering study of charge-density wave correlations in YBa 2 Cu 3 O 6+ x". In: *Physical Review B* 90.5 (2014), p. 054513.

[10] Felix Bloch. "Zur theorie des ferromagnetismus". In: *Zeitschrift für Physik* 61.3-4 (1930), pp. 206–219.

[11] L Braicovich et al. "The simultaneous measurement of energy and linear polarization of the scattered radiation in resonant inelastic soft x-ray scattering". In: *Review of Scientific Instruments* 85.11 (2014), p. 115104.

[12] Carmen J Calzado et al. "Four-spin cyclic exchange in spin ladder cuprates". In: *Physical Review B* 67.13 (2003), p. 132409.

[13] J Chang et al. "Direct observation of competition between superconductivity and charge density wave order in YBa2Cu3O6. 67". In: *Nature Physics* 8.12 (2012), pp. 871–876.

[14] CT Chen et al. "Experimental confirmation of the X-ray magnetic circular dichroism sum rules for iron and cobalt". In: *Physical review letters* 75.1 (1995), p. 152.

[15] SG Chiuzbăian et al. "Localized electronic excitations in nio studied with resonant inelastic X-ray scattering at the Ni M threshold: Evidence of spin flip". In: *Physical review letters* 95.19 (2005), p. 197402.

[16] R Coldea et al. "Spin waves and electronic interactions in La 2 CuO 4". In: *Physical review letters* 86.23 (2001), p. 5377.

[17] JHP Colpa. "Diagonalization of the quadratic boson hamiltonian". In: *Physica A: Statistical Mechanics and its Applications* 93.3 (1978), pp. 327–353.

[18] Bastien Dalla Piazza. "Theories of Experimentally Observed Excitation Spectra of Square Lattice Antiferromagnets". PhD thesis. École polytechnique fédérale de Lausanne, 2014.

[19] Bastien Dalla Piazza et al. "Unified one-band Hubbard model for magnetic and electronic spectra of the parent compounds of cuprate superconductors". In: *Physical Review B* 85.10 (2012), p. 100508.

[20] Andrea Damascelli, Zahid Hussain, and Zhi-Xun Shen. "Angle-resolved photoemission studies of the cuprate superconductors". In: *Reviews of modern physics* 75.2 (2003), p. 473.

[21] J-YP Delannoy et al. "Low-energy theory of the t-t'-t''-U Hubbard model at half-filling: Interaction strengths in cuprate superconductors and an effective spin-only description of La 2 CuO 4". In: *Physical Review B* 79.23 (2009), p. 235130.

[22] Greta Dellea. "Collective excitations in high temperature superconducting cuprates studied by resonant inelastic soft x-ray scattering". PhD thesis. Politecnico di Milano, 2016.

[23] ME Dinardo et al. "Gaining efficiency and resolution in soft X-ray emission spectrometers thanks to directly illuminated CCD detectors". In: *Nuclear Instruments and Methods in Physics Research Section A: Accelerators, Spectrometers, Detectors and Associated Equipment* 570.1 (2007), pp. 176–181.

[24] David Shai Ellis et al. "Correlation of the Superconducting Critical Temperature with Spin and Orbital Excitation Energies In (Ca {x} La {1-x})(Ba {1.75-x} La {0.25+ x}) Cu {3} O {y} as Measured by Resonant Inelastic X-ray Scattering". In: *arXiv preprint arXiv:1508.02021* (2015).

[25] Hendrik Johan Eskes. "Some unusual aspects of correlated systems". PhD thesis. University of Groningen, 1992.

[26] Henk Eskes and Robert Eder. "Hubbard model versus t-J model: The one-particle spectrum". In: *Physical Review B* 54.20 (1996), R14226.

[27] Øystein Fischer et al. "Scanning tunneling spectroscopy of high-temperature superconductors". In: *Reviews of Modern Physics* 79.1 (2007), p. 353.

[28] G Ghiringhelli et al. "Long-range incommensurate charge fluctuations in (Y, Nd) Ba2Cu3O6+ x". In: *Science* 337.6096 (2012), pp. 821–825.

[29] P Glatzel, M Sikora, and M Fernandez-Garcia. "Resonant X-ray spectroscopy to study K absorption pre-edges in 3d transition metal compounds". In: *The European Physical Journal Special Topics* 169.1 (2009), pp. 207–214.

[30] M Guarise et al. "High-energy magnon dispersion demonstrate extended interactions in the undoped cuprates". In: *arXiv preprint arXiv:1004.2441* (2010).

[31] Stephen M Hayden. "Neutron Scattering and the Magnetic Response of Superconductors and Related Compounds". In: *Superconductivity*. Springer, 2008, pp. 993–1029.

[32] Albert Hofmann. *The physics of synchrotron radiation*. Vol. 20. Cambridge University Press, 2004.

[33] Y Honda, Y Kuramoto, and T Watanabe. "Effects of cyclic four-spin exchange on the magnetic properties of the CuO 2 plane". In: *Physical Review B* 47.17 (1993), p. 11329.

[34] *ID32 at the European Synchrotron Radiation Facility (ESRF)*. URL: `http://www.esrf.eu/usersandscience/experiments/electstructmagn/id32`.

[35] Aharon Kapitulnik et al. "Polar Kerr effect as probe for time-reversal symmetry breaking in unconventional superconductors". In: *New Journal of Physics* 11.5 (2009), p. 055060.

[36] TA Kaplan. "Some effects of anisotropy on spiral spin-configurations with application to rare-earth metals". In: *Physical Review* 124.2 (1961), p. 329.

[37] Akio Kotani and Shik Shin. "Resonant inelastic x-ray scattering spectra for electrons in solids". In: *Reviews of Modern Physics* 73.1 (2001), p. 203.

[38] Ryogo Kubo. "The spin-wave theory of antiferromagnetics". In: *Physical Review* 87.4 (1952), p. 568.

[39] Cassiano Langini. "Advances in the detection at the new XMCD and RIXS beamline of the ESRF". Master's thesis. Politecnico di Milano, 2015.

[40] Mathieu Le Tacon et al. "Intense paramagnon excitations in a large family of high-temperature superconductors". In: *Nature Physics* 7.9 (2011), pp. 725–730.

[41] TK Lee and Shiping Feng. "Doping dependence of antiferromagnetism in La 2 Cu O 4: A numerical study based on a resonating-valence-bond state". In: *Physical Review B* 38.16 (1988), p. 11809.

[42] Ruixing Liang, DA Bonn, and WN Hardy. "Evaluation of CuO 2 plane hole doping in YBa 2 Cu 3 O 6+ x single crystals". In: *Physical Review B* 73.18 (2006), p. 180505.

[43] José Lorenzana, J Eroles, and Sandro Sorella. "Does the Heisenberg model describe the multimagnon spin dynamics in antiferromagnetic CuO layers?" In: *Physical Review Letters* 83.24 (1999), p. 5122.

[44] Jose Lorenzana and Götz Seibold. "Metallic Mean-Field Stripes, Incommensurability, and ChemicalPotential in Cuprates". In: *Physical review letters* 89.13 (2002), p. 136401.

[45] AH MacDonald, SM Girvin, and D t Yoshioka. "t U expansion for the Hubbard model". In: *Physical Review B* 37.16 (1988), p. 9753.

[46] BPP Mallett et al. "Dielectric versus magnetic pairing mechanisms in high-temperature cuprate superconductors investigated using Raman scattering". In: *Physical review letters* 111.23 (2013), p. 237001.

[47] Masahiko Matsubara et al. "Polarization dependence of resonant X-ray emission spectra in early transition metal compounds". In: *Journal of the Physical Society of Japan* 69.5 (2000), pp. 1558–1565.

[48] Matteo Minola. "Magnetic, orbital and charge fluctuations in layered cuprates studied by resonant soft X-ray scattering". PhD thesis. Politecnico di Milano, 2013.

[49] Nevill F Mott. "The basis of the electron theory of metals, with special reference to the transition metals". In: *Proceedings of the Physical Society. Section A* 62.7 (1949), p. 416.

[50] NF Mott. "Metal-insulator transition". In: *Reviews of Modern Physics* 40.4 (1968), p. 677.

[51] D Muñoz, F Illas, and I de PR Moreira. "Accurate Prediction of Large Antiferromagnetic Interactions in High-T c HgBa 2 Ca n- 1 Cu n O 2 n+ 2+ δ (n= 2, 3) Superconductor Parent Compounds". In: *Physical review letters* 84.7 (2000), p. 1579.

[52] MR Norman, D Pines, and C Kallin. "The pseudogap: friend or foe of high T c?" In: *Advances in Physics* 54.8 (2005), pp. 715–733.

[53] *Paul Scherrer Institute official website*. URL: `https://www.psi.ch/`.

[54] E Pavarini et al. "Band-structure trend in hole-doped cuprates and correlation with T c max". In: *Physical Review Letters* 87.4 (2001), p. 047003.

[55] S Petit. "Numerical simulations and magnetism". In: *École thématique de la Société Française de la Neutronique* 12 (2011), pp. 105–121.

[56] KW Plumb et al. "High-energy continuum of magnetic excitations in the two-dimensional quantum antiferromagnet Sr 2 CuO 2 Cl 2". In: *Physical Review B* 89.18 (2014), p. 180410.

[57] M Roger and JM Delrieu. "Cyclic four-spin exchange on a two-dimensional square lattice: Possible applications in high-T c superconductors". In: *Physical Review B* 39.4 (1989), p. 2299.

[58] M Moretti Sala et al. "Energy and symmetry of dd excitations in undoped layered cuprates measured by Cu L3 resonant inelastic x-ray scattering". In: *New Journal of Physics* 13.4 (2011), p. 043026.

[59] Shigemi Sasaki et al. "Design of a new type of planar undulator for generating variably polarized radiation". In: *Nuclear Instruments and Methods in Physics Research Section A: Accelerators, Spectrometers, Detectors and Associated Equipment* 331.1 (1993), pp. 763–767.

[60] Götz Seibold and Jose Lorenzana. "Doping dependence of spin excitations in the stripe phase of high-T c superconductors". In: *Physical Review B* 73.14 (2006), p. 144515.

[61] John C Slater. "Atomic shielding constants". In: *Physical Review* 36.1 (1930), p. 57.

[62] John C Slater. "Cohesion in monovalent metals". In: *Physical Review* 35.5 (1930), p. 509.

[63] *Soleil ring structure*. URL: `http://www.synchrotron-soleil.fr/`.

[64] S Toth and B Lake. "Linear spin wave theory for single-Q incommensurate magnetic structures". In: *Journal of Physics: Condensed Matter* 27.16 (2015), p. 166002.

[65] JM Tranquada et al. "Evidence for stripe correlations of spins and holes in copper oxide superconductors". In: *Nature* 375.6532 (1995), pp. 561–563.

[66] JM Tranquada et al. "Mixed valency, hole concentration, and T c in YBa 2 Cu 3 O 6+ x". In: *Physical Review B* 38.13 (1988), p. 8893.

[67] John M Tranquada. "Neutron scattering studies of antiferromagnetic correlations in cuprates". In: *Handbook of High-Temperature Superconductivity*. Springer, 2007, pp. 257–298.

[68] John M Tranquada et al. "Neutron scattering study of magnetic excitations in YBa 2 Cu 3 O 6+ x". In: *Physical Review B* 40.7 (1989), p. 4503.

[69] K Yamada et al. "Doping dependence of the spatially modulated dynamical spin correlations and the superconducting-transition temperature in La 2- x Sr x CuO 4". In: *Physical Review B* 57.10 (1998), p. 6165.

[70] Kei Yosida. *Theory of Magnetism*. Vol. 122. Springer Science & Business Media, 1996.